

Doctoral Dissertation

(Shinshu University)

**The interplay of mesoscopic structural and dynamic fluctuations and
macroscopic properties in soft materials**

March 2019

Keiichi Yanase



Interdisciplinary Graduate School of Science and Technology

Shinshu University

Contents

Chapter 1.	General introduction	1
1.1.	Polymers and gels	2
1.2.	Bilayer membranes	5
1.3.	Proteins	7
Chapter 2.	Theoretical background and experiments	15
2.1.	Small angle x-ray scattering	15
2.2.	Dielectric relaxation spectroscopy	23
2.3.	Auxiliary measurements	30
Chapter 3.	Microglobule formation and a microscopic order parameter monitoring the phase transition of aqueous poly(<i>N</i> -isopropylacrylamide) solution	32
3.1.	Introduction	33
3.2.	Experimental Methods	35
3.3.	Results and Discussion	36
3.4.	Conclusions	50
Chapter 4.	Ion fluctuations and intermembrane interactions in aqueous dispersions of dialkylchain cationic surfactant	56
4.1.	Introduction	57
4.2.	Experimental Methods	60
4.3.	Results and Discussion	64
4.4.	Conclusions	92
Chapter 5.	Intermolecular interactions and molecular dynamics in bovine serum albumin solutions	98
5.1.	Introduction	99

5.2.	Experimental Methods	101
5.3.	Results and Discussion	104
5.4.	Conclusions	116
Chapter 6.	Conclusions	121
6.1.	Summary	121
6.2.	Future Prospects	125
	Acknowledgements	139

Chapter 1. General introduction

Softmatter or soft-material is a general term representing a series of ‘soft’ substances, such as polymers, surfactants, proteins, colloids, and biological membranes [1]. These substances often exhibit a number of spatially and temporally hierarchical properties [2]. The better understanding of these hierarchical properties is considered to be a key to elucidation of the functional expression mechanisms in diverse soft-condensed and molecular complex systems. In order to clarify these underlying mechanisms, it is no doubt important to investigate not only the microscopic to mesoscopic (static) structure of the complex systems but molecular and cooperative dynamics of both solute and solvent in a combined and systematic manner, and further we need to explore more extensively the interplay between them. However, how physical properties on the microscopic to mesoscopic scales are connected to the macroscopic properties of the soft-materials have not yet been well understood.

On the one hand, the two areas, solution chemistry and colloid/soft matter physics, have essentially different concepts on how solvent molecules are treated and which temporal and spatial hierarchies are mainly focused on as a major interest. The former especially focuses on fundamental aspects of liquid systems, including structure, dynamics, and intermolecular forces, at the molecular or microscopic level [3–5]. In contrast, the latter is an wide-spread academic area in which effects of the solvent (in many cases, water) are often coarse-grained and the mesoscopic to macroscopic properties of the complex systems, such as colloidal aspects, phase behavior, slow or arrested dynamics, and so forth, are elaborately and selectively pursued [6–10].

‘Mesoscopic’ may be defined as an intermediate between microscopic and macroscopic, whose typical length scale is certainly greater than the size of atoms but considerably smaller than the size of micron-sized systems. Therefore, it may be understood as the length scale between the size of small (low-molecular-weight) molecules and that of micron-meter sized, bulklike materials [11–15]. Such macroscopic structures are not simply constructed by the microscopic atomic arrangement, but has an intermediate or mesoscopic order. The self-organization or condensation of these mesoscopic structures produces a larger macroscopic structure, leading to manifestation of the structural hierarchy. In this study, I have particularly focused on the above-mentioned interdisciplinary area when dealing with soft materials like polymers, surfactant self-assemblies, and bio-macromolecules, treating solvent molecules in an explicit manner. In order to obtain deeper insights into the interplay of mesoscopic structural and dynamic fluctuations and macroscopic properties in soft materials, I have carried out extensive scattering and spectroscopic experiments on thermo-responsive polymer, dialkylchain cationic surfactant, and globular protein, in aqueous media.

1.1. Polymers and gels

Polymers or macromolecules are defined as large molecules composed of covalently bonded small molecular units. In liquid states (solution or polymer melt), single bonds in polymers can freely rotate, polymer chains existing in the so-called random coil state [16]. Amphiphilic polymers comprising hydrophilic and hydrophobic groups can often provide potential applications as stimuli-responsive materials because they are able to adapt to external environment, such as a change in temperature and solvent composition [17–19]. In aqueous media, non-ionic polymers interact with solvent water via hydrogen bonding,

and at the same time, entropic driving forces lead to solvent-water mediated attractive interactions between hydrophobic side-chain groups, which is generally called hydrophobic interaction. Thereby, the formation of hydrogen bond between water and hydrophilic polar moieties improves their solubility, but the hydrophobic non-polar groups have a tendency to aggregate, lowering the solubility and causing phase separation in an opposite manner [20].

Chemical gels are materials that contains a large amount of solvent in the network structure formed by cross-linked polymers. This unique structure provide gel materials an intermediate unique property between liquid and solid. Gels reflect and amplify the nature of polymers. Gels can undergo the volume phase transition (VPT), where their volume changes discontinuously at a certain temperature or solvent composition [21]. This phenomenon, which is mainly driven by changes of affinity of polymers for solvents and osmotic pressure of gels, is to be universally observed in any kinds of gels [22]. The VPT of gels is also triggered by electric field [23], inorganic salt [24], and visible light [25], which are applied to cell culture substratum [26], actuator [27], and so forth. On the other hand, knowledge about fundamental principles common to polymers, such as critical phenomena [28] and diffusion kinetics [29], have been accumulated in above-mentioned applied researches. Poly(*N*-isopropylacrylamide) (pNIPAm) is a representative thermo-responsive polymer. pNIPAm-based gels were enthusiastically investigated in the pioneering study on VPT of gels [22]. pNIPAm involves both hydrophilic acrylamide groups and hydrophobic isopropyl groups in its side chain group. Because of the consequent amphiphilic nature, pNIPAm exhibits a lower critical solution temperature (LCST) of about 32°C in aqueous media [30]. Aqueous pNIPAm solution segregates into polymer-rich and water-rich phases when temperature is raised, which,

from the thermodynamic point of view, is mainly due to entropy-driven hydrophobic interaction [30]. During the phase transition, the system exhibits spinodal decomposition and the critical phenomena, in which the length scale and the magnitude of density fluctuation arising from the swollen coil polymer simultaneously diverge [31]. At spinodal temperature, pNIPAm chains undergo the coil-to-globule transition, the swollen polymer chains being collapsed into the globular state [32–36].

Theoretical studies have suggested a couple of currently prevailing concepts to explain on the coil-to-globule transition of aqueous amphiphilic polymer systems, such as the solvent-fluctuation induced transition [37], cooperative hydration/dehydration [38], and mean energetic state of aqueous solvent [39]. All these studies pointed out that the importance of the role of solvent. Dehydration behavior of the polymer chains, which may be closely related to the phase separation, was also investigated by spectroscopic techniques [40–43]. However, no specific information has been obtained.

Despite long years of studies, fundamental understanding of the microscopic features of pNIPAm chains and their changes during the coil-to-globule transition has not yet been reached. Partial globule formation even in one phase region was vaguely suggested in the cooperative hydration/dehydration picture [38]. However, this has not yet been experimentally evidenced. Recent Raman multivariate curve resolution study revealed that significant changes in the OH-band frequency range of the spectrum occur only above the phase transition temperature, where the pNIPAm chains collapse [43]. This unexpected observation appears to be inconsistent with the solvent-fluctuation induced transition mechanism [37]. I have tackled these problems by combining scattering and spectroscopic techniques and scrutinized the accurately measured experimental data in the extended scattering-vector and frequency ranges, which has allowed us to monitor the

change of the microscopic to mesoscopic (static) structure and the hydration state of the polymer chains via the cooperative dynamics of solvent water. This way, I have been able to draw a further microscopic picture of the critical fluctuation of pNIPAm in solution, which was overlooked in the previous small angle neutron scattering studies [31, 44]

1.2. Bilayer membranes

Surfactant molecules assemble into a variety of structures self-organization structures in aqueous media, such as micelles, liquid crystals, and vesicles, depending on temperature, surfactant concentration, and other external conditions [7]. They have been serve as functional materials and widely used in household, cosmetic, medical, and food industries. Calculation of Gibbs free energy explains why they form self-assembled structures and how the shape of these self-assemblies is determined [45]. The major driving-force of the surfactant self-assembly formation is hydrophobic interaction, namely a tendency for hydrophobic molecules to aggregate in aqueous media so as to compensate larger entropic loss than enthalpic gain when hydrophobic molecules or groups are dissolved into water.

The packing parameter (P) conveniently connects geometrical structure of surfactant molecules to shape of their aggregates [46]. P is given by $v/a_s l$, where v and l are volume and length of hydrophobic groups and a_s is cross sectional area of a surfactant molecule at the hydrophilic/hydrophobic interface. Production of spherical, rod, and planer self-assembly structures is indicated by $P = 1/3$, $1/2$, and 1 , respectively. If this concept is applied to surfactant/water system, an increase of P from $1/3$ to 1 generally corresponds to the production of micellar solution and cubic liquid crystalline phase ($P = 1/3$), hexagonal liquid crystalline phase ($P = 1/2$), and lamellar liquid crystalline phase ($P = 1$).

This behavior can usually be interpreted as a decrease of the relative volume of the hydrated hydrophilic head group against that of the hydrophobic tail due to a less amount of water at higher surfactant concentration.

Dialkylchain surfactants, such as phospholipids and quaternary ammonium salts, can form lamellar gels and bilayer vesicles [47]. This is because the P value becomes close to unity even at low surfactant concentration owing to the fact that the volume of the hydrocarbon in the hydrophobic part is nearly twice larger than that of usual micelle-forming mono-alkylchain surfactants [7]. Note that strictly speaking, different from lamellar liquid crystalline phase (L_α) often observed in dense surfactant/water systems, α -gel is not in a thermodynamically stable, single phase state.

It was long believed that only phospholipids can produce multi-lamellar vesicles (MLVs) until Kunitake showed in 1977 that a totally synthetic dialkyl dimethyl ammonium bromide can produce multi-lamellar vesicles (MLVs) [48]. Therefore, the vesicle formation cannot be attributed to specific structure of hydrophilic groups in phospholipid molecules, but rather to a balance between bulkiness of double-chain hydrophobic group and head group repulsion, realizing $P = 1$. A number of subsequent researches reported pseudo-spontaneous vesicle formation in ionic [49, 50] and nonionic [51] systems.

Dialkyl dimethyl ammonium (DDA) salt is widely used for household products [52, 53]. An inorganic salt like CaCl_2 is used as a viscosity modifying agent of aqueous double-chain cationic surfactant-based materials. In water, DDA salt forms a lamellar gel (α -gel), which involves partially frozen hydrocarbon chains as proved by the emergence of a sharp reflection peak at about 15.2 nm^{-1} . α -gels are usually stiff, showing no fluidity, but if a small amount of salt is added, a stiff gel is almost immediately transformed into a highly

fluidic milky dispersion. However, surprisingly, there have been virtually no report on this issue. So I have investigated aqueous dispersions of dihardened tallow dimethyl ammonium chloride (DTDAC; 2HT) in order to clarify the underlying mechanisms of this intriguing phenomena, the salt-induced phase transition and the accompanying drastic reduction of the dispersion viscosity. To shed light on the connection between these macroscopic phenomena and the underlying microscopic-to-mesoscopic nature of the systems, I have focused on the effects of CaCl_2 concentration on the interactions between the bilayer membranes formed by 2HT.

Understanding interactions between membranes is crucial to understand diverse physical, chemical and biological phenomena. According to what Derjaguin-Landau-Verwey-Overbeek (DLVO) theory predicted, fundamental interactions between membranes are governed by a balance between attractive van der Waals and repulsive electric double-layer forces [7, 54–56]. It is known that non-DLVO forces like Helfrich undulation interaction and hydration force also give notable influence [7, 56-65]. By means of simultaneous small- and wide-angle x-ray scattering, I have evaluated the extent of the bilayer undulation fluctuation disorder as a function of CaCl_2 concentration. Buchner and co-workers showed multidimensional fluctuations of the counterions in aqueous micellar solutions of sodium dodecyl sulfate [66] and alkyltrimethylammonium salts.[67, 68] To monitor counterion fluctuations at the interface of the 2HT bilayer membranes and the cooperative dynamics of solvent water, I have used dielectric relaxation spectroscopy.

1.3. Proteins

Proteins form a specific three-dimensional (3D) structure determined by a one-

dimensional amino acid sequence. Individual proteins have their own specific biological functions closely linked with their three-dimensional structure, For instance, proteins serve as a transporter of molecules, an enzyme for catalyzing metabolic reactions, building blocks of biological structure for cells and organisms, and an antibody for immune response, in aqueous environment [47]. Therefore, understanding the static structure including the protein 3D structure and protein-protein interactions in solution is undoubtedly important not only for establishing efficient crystallization conditions of protein crystals but understanding the mechanisms of protein condensation diseases like sickle cell anemia [69] and cataract [70] at the molecular level.

Protein-protein interactions are biased by solvent conditions, sharply depending on the type of co-existing salts, ionic strength, and pH. These factors may affect both the effective charges of the protein and the screening effect of long-range electrostatic repulsion between protein molecules. In previous works, protein molecules were often regarded as monodisperse charged colloidal particles, which was broadly successful [71–75].

However, when accounting for protein-protein interactions, we now need to recognize that protein-protein interactions in solution is largely affected by complexity of the 3D structure of protein molecules, e.g., irregular shape, distributed hydrophobic and hydrophilic patches, and inhomogeneous charge distributions. These features distinguish protein molecules from simple charged spherical colloidal particles. Indeed, conventional interaction potential models for colloidal dispersions like hardsphere and screened Coulomb potentials applied to experimental scattering intensities of protein solutions sometimes failed to describe their complicated scattering curves [76–78]. This seems to demonstrate that actual protein-protein interactions in solution is not isotropic.

Bovine serum albumin (BSA) is the most abundant plasma protein in bovine's blood stream, which is a counterpart of human serum albumin (HSA). BSA has a heart-like shape, whose architecture is predominately helical, consisting of three domains. A primary function of BSA is adjustment of colloid osmotic pressure (COP) of blood [79], in which a major part is undertaken by van't Hoff pressure. Thus preservation of the number density of BSA in blood stream should be important. I infer that the structure of the BSA molecule, including its shape, distributions of patches and surface charges, is optimized so as to avoid self-aggregation and aggregation with other plasma proteins and blood cells. An isoelectric point of BSA is known to be ca. 5.3, which means that BSA is strongly negatively charged at physiological pH [80].

To understand the interplay between the macroscopic aspect of the BSA specific function, preservation of van't Hoff pressure under physiological solution condition, and mesoscopic BSA-BSA interactions, I have investigated spatial correlations of BSA molecules in solution at different ionic strength and BSA concentrations. To overcome the serious problems caused by the complex molecular structure and the expected, resulting anisotropic nature of the BSA-BSA interactions, I have used a potential model free route of the static structure analysis for interpretation of the experimental structure factors.

Except effects of ionic strength and pH, solvent conditions play another important role for the protein-protein interactions because a heterogeneous field formed by the protein molecules should regulate the hydration state, which may be manifested by the slower dynamics of the hydration water molecules, and may also affect diffusion kinetics of the protein molecules. Counterion fluctuations around the protein molecules must also be considered. Therefore, I have used dielectric relaxation spectroscopy to monitor the

collective dynamics of solute and solvent molecules.

References

- [1] P.G. de Gennes, *Rev. Mod. Phys.* 64, 645-648 (1992).
- [2] T. Hashimoto, *Principles and Applications of X-ray, Light and Neutron Scattering*, Kodansha Ltd. (2017).
- [3] D. Eisenberg and W. Kauzmann, *The Structure and Properties of Water*, Clarendon Press (2005).
- [4] J.-P. Hansen and I.R. McDonald, *Theory of Simple Liquids*, Academic Press (2006)
- [5] A. Ben-Naim, *Molecular Theory of Water and Aqueous Solutions*, World Scientific Publishing Company (2009).
- [6] T. Witten and P. Pincus, *Structured Fluids: Polymers, Colloids, Surfactants*, Oxford University Press (2004).
- [7] J.N. Israelachvili, *Intermolecular and surface forces*, Academic Press (2011).
- [8] G.R. Strobl, *Condensed Matter Physics*, Springer (2011).
- [9] I.W. Hamray, *Introduction to Soft Matter*, Wiley (2013).
- [10] O. Glatter, *Scattering Methods and their Application in Colloid and Interface Science*, Elsevier (2018).
- [11] T. Hashimoto, H. Jinnai, Y. Nishikawa, and T. Koga, *Macromol. Symp.* 190, 9-22 (2002).
- [12] H. Cölfen and S. Mann, *Angew. Chem. Int. Ed.* 42, 2350-2365 (2003).
- [13] T. Hashimoto, *J. Polym. Sci. B* 42, 3027-3062 (2004).
- [14] M. Praprotnik, L.D. Site, and K. Kremer, *Annu. Rev. Phys. Chem.* 59, 545-571 (2008).

- [15] T. Hashimoto and H. Murase, *IUCrJ* 2, 59-73 (2015).
- [16] P.-G. de Gennes, *Scaling Concepts in Polymer Physics*, Cornell University Press (1979).
- [17] C. de las Heras Alarcon, S. Pennadam, and C. Alexander, *Chem. Soc. Rev.* 34, 276-285 (2005).
- [18] D. Schmaljohann, *Adv. Drug Deliv. Rev.* 58, 1655-1670 (2006).
- [19] M.A.C. Stuart, W.T.S. Huck, J. Genzer, M. Müller, C. Ober, M. Stamm, G.B. Sukhorukov, I. Szleifer, V.V. Tsukruk, M. Urban, F. Winnik, S. Zauscher, I. Luzinov, and S. Minko, *Nat. Mater.* 9, 101-103 (2010).
- [20] V. Aseyev, H. Tenhu, and F.M. Winnik, in *Self Organized Nanostructures of Amphiphilic Block Copolymers II* (Springer, Berlin, Heidelberg), 29-89 (2011).
- [21] T. Tanaka, *Phys. Rev. Lett.* 40, 820-823 (1978).
- [22] Y. Hirokawa and T. Tanaka, *J. Phys. Chem.* 81, 6379-6380 (1984).
- [23] T. Tanaka, I. Nishio, S.-T. Sun, and S. Ueno-Nishio, *Nature* 218, 467-469 (1982).
- [24] I. Ohmine and T. Tanaka, *J. Chem. Phys.* 77, 5725-5729 (1982).
- [25] A. Suzuki and T. Tanaka, *Nature* 346, 345-347 (1990).
- [26] T. Okano N. Yamada, H. Sakai, and Y. Sakurai, *J. Biomed. Mater. Res.* 27, 1243-1251 (1993).
- [27] Y. Osada, H. Okuzaki, and H. Hori, *Nature* 355, 242-244 (1992).
- [28] T. Tanaka, S. Ishiwata, and C. Ishimoto, *Phys. Rev. Lett.* 38, 771-774 (1977).
- [29] T. Tanaka and D.J. Fillmore, *J. Chem. Phys.* 70, 1214-1218 (1979).
- [30] M. Heskins and J.E. Guillet, *Macromol. Sci. Pure Appl. Chem.* 2, 1441-1455 (1968).
- [31] M. Shibayama, T. Tanaka, and C.C. Han, *J. Chem. Phys.* 97, 6829-6841 (1992).
- [32] K. Kubota, S. Fujishige, and I. Ando, *J. Phys. Chem.* 94, 5154-5158 (1990).

- [33] C. Wu and S. Zhou, *Macromolecules* 28, 8381-8387 (1995).
- [34] C. Wu and S. Zhou, *Macromolecules* 28, 5388-5390 (1995).
- [35] C. Wu and X. Wang, *Phys. Rev. Lett.* 80, 4092-4094 (1998).
- [36] X. Wang, X. Qiu, and C. Wu, *Macromolecules* 31, 2972-2976 (1998).
- [37] P.R. ten Wolde and D. Chandler, *Proc. Natl. Acad. Sci. U. S. A.* 99, 6539-6543 (2002).
- [38] Y. Okada and F. Tanaka, *Macromolecules* 38, 4465-4471 (2005).
- [39] I. Bischofberger, D. Calzolari, P. De Los Rios, I. Jelezarov, and V. Trappe, *Sci. Rep.* 4, 4377 (2014).
- [40] Y. Maeda, T. Higuchi, and I. Ikeda, *Langmuir* 16, 7503-7509 (2000).
- [41] Y. Ono and T. Shikata, *J. Am. Chem. Soc.* 128, 10030-10031 (2006).
- [42] M. Füllbrandt, E. Ermilova, A. Asadujjaman, R. Hölzel, F.F. Bier, R. von Klitzing, and A. Schönhals, *J. Phys. Chem. B* 118, 3750-3759 (2014).
- [43] K. Mochizuki and D. Ben-Amotz, *J. Phys. Chem. Lett.* 8, 1360-1364 (2017).
- [44] A. Meier-Koll, V. Pipich, P. Busch, C.M. Papadakis, and P. Müller-Buschbaum, *Langmuir* 28, 8791-8798 (2012).
- [45] C. Tanford, *The Hydrophobic Effect*, Wiley-Interscience (1973).
- [46] J.N. Israelachvili, D.J. Mitchell, and B.W. Ninham, *J. Chem. Soc., Faraday Trans. 2* 72, 1525-1568 (1976).
- [47] D. Voet, J.G. Voet, and C.W. Pratt, *Fundamentals of biochemistry*, John Wiley and Sons, Inc. (1999).
- [48] T. Kunitake and Y. Okahata, *J. Am. Chem. Soc.* 99, 3860-3861 (1977).
- [49] J.E. Brady, D.F. Evans, B. Kachar, and B.W. Ninham, *J. Am. Chem. Soc.* 106, 4279-4280 (1984).
- [50] M. Aratono, A. Mori, I. Koga, M. Shigehisa, N. Onimaru, K. Tsuchiya, T. Takiue,

- and H. Matsubara, *J. Phys. Chem. B* 112, 12304-12311 (2008).
- [51] K. Bryskhe, S. Bulut, and U. Olsson, *J. Phys. Chem. B* 109, 9265-9274 (2005).
- [52] W.M. Linfield, J.C. Sherrill, G.A. Davis, and R.M. Raschke, *J. Am. Oil Chem. Soc.* 35, 590-593 (1958).
- [53] H. Kunieda and K. Shinoda, *J. Phys. Chem.* 82, 1710-1714 (1978).
- [54] B. Derjaguin and L. Landau, *Acta Physicochim. URSS* 14, 633-662 (1941).
- [55] E.J.W. Verwey and J.T.G. Overbeek, *Theory of the stability of lyophobic colloids*, Elsevier (1948).
- [56] J.N. Israelachvili and P.M. McGuiggan, *Science* 241, 795-800 (1988).
- [57] I. Langmuir, *J. Chem. Phys.* 6, 873-896 (1938).
- [58] D.M. LeNeveu, R.P. Rand, V.A. Parsegian, and D. Gingell, *Biophys. J.* 18, 209-230 (1977).
- [59] W. Helfrich, *Z. Naturforsch.* 33, 305-315 (1978).
- [60] I. Sogami, *Phys. Lett. A* 96, 199-203 (1983).
- [61] I. Sogami and N. Ise, *J. Chem. Phys.* 81, 6320-6332 (1984).
- [62] M. Smalley, *Mol. Phys.* 71, 1251-1267 (1990).
- [63] S.T. Milner and D. Roux, *J. Phys. I* 2, 1741-1754 (1992).
- [64] D. Lukatsky and S. Safran, *Phys. Rev. E* 60, 5848-5857 (1999).
- [65] J.I. Kilpatrick, S.-H. Loh, and S.P. Jarvis, *J. Am. Chem. Soc.* 135, 2628-2634 (2013).
- [66] P. Fernandez, S. Schrödle, R. Buchner, and W. Kunz, *ChemPhysChem* 4, 1065-1072 (2003).
- [67] C. Baar, R. Buchner, and W. Kunz, *J. Phys. Chem. B* 105, 2914-2922 (2001).
- [68] F.S. Lima, H. Chaimovich, I.M. Cuccovia, and R. Buchner, *Langmuir* 29, 10037-10046 (2013).

- [69] C.T. Noguchi and A.N. Schechter, *Annu. Rev. Biophys. Biophys. Chem.* 14, 239-263 (1985).
- [70] N. Dorsaz, G.M. Thurston, A. Stradner, P. Schurtenberger, and G. Foffi, *J. Phys. Chem. B* 113, 1693-1709 (2009).
- [71] G. Pellicane, D. Costa, and C. Caccamo, *J. Phys. Condens. Matter* 16, S4923-S4936 (2004).
- [72] A. Tardieu, A. L. Verge, M. Malfois, F. Bonnete, S. Finet, M. R. Kautt, and L. Belloni, *J. Cryst. Growth.* 196, 193-203 (1999).
- [73] B. Lonetti, E. Fratini, S.H. Chen, and P. Baglioni, *Phys. Chem. Chem. Phys.* 6, 1388-1395 (2004).
- [74] Y. Liu, E. Fratini, P. Baglioni, W.R. Chen, and S.H. Chen, *Phys. Rev. Lett.* 95, 118102 (2005).
- [75] F. Zhang, M. W. A. Skoda, R. M. J. Jacobs, R. A. Martin, C. M. Martin, and F. Schreiber, *J. Phys. Chem. B* 111, 251-259 (2007).
- [76] A. Stradner, H. Sedgwick, F. Cardinaux, W.C.K. Poon, S.U. Egelhaaf, and P. Schurtenberger, *Nature.* 432, 492-495 (2004).
- [77] T. Sato, T. Komatsu, A. Nakagawa, and E. Tsuchida, *Phys. Rev. Lett.* 98, 208101 (2007).
- [78] T. Fukasawa and T. Sato, *Phys. Chem. Chem. Phys.* 13, 3187-3196 (2011).
- [79] T. Peters, *All about Albumin, Biochemistry, Genetics, and Medical Applications* Academic, New York (1996).
- [80] J.F. Foster and L.J. Kaplan, *Biochem.* 10, 630-636 (1971).

Chapter 2. Theoretical background and experiments

2.1. Small angle x-ray scattering

Small angle scattering of x-rays (SAXS) is an eminent technique to investigate microscopic structure of soft materials, such as colloidal particles, polymers, gels, biomolecules, surfactant systems, and so forth. Scattering experiments allow us to access whole size, shape, and internal structure of scattering objects and also provide information about interparticle (or intermolecular) interactions.

2.1.1. Scattering vector

Scattering experiments measure the scattering intensity as a function of the magnitude of the scattering vector, q

$$q = |\mathbf{k}_1 - \mathbf{k}_0| = \frac{4\pi}{\lambda} \sin\left(\frac{\theta}{2}\right) \quad (2.1)$$

where θ is the total scattering angle, λ the wavelength of the x-rays, and \mathbf{k} the wave vector of the incident and scattered waves. Note that we assume an elastic scattering processes, where the wave number of incident wave k_0 and scattered wave k_1 are preserved: $k_0 = k_1 = 2\pi/\lambda$. The situation is schematically shown in Figure 2.1.

According to the de Broglie relation, the wavelength is related to the momentum p via the Planck constant h : $\lambda = h/p$. The relation between the wave number and the momentum can be written as $p = \hbar k$ with $\hbar = h/2\pi$. Therefore, the scattering vector is often called the momentum transfer. Essential advantage of choice for the scattering vector q as the horizontal axis, instead of the total scattering angle or diffraction angle, when the scattered intensity is plotted lies in the fact that the q -value does not depend on the

wavelength of the incident radiation used. The scattering vector is also utilized for describing a phase difference of the scattered waves φ . According to Figure 2.1, a path-length difference l of the scattered wave from an arbitrary reference point P_1 and that from a position P_2 defined by a vector \mathbf{r} in a scattering body is described as $l = \mathbf{r} \cdot \mathbf{s}_0 - \mathbf{r} \cdot \mathbf{s}_1 = -\mathbf{r} \cdot (\mathbf{s}_1 - \mathbf{s}_0)$, where \mathbf{s}_0 and \mathbf{s}_1 are unit vectors of \mathbf{k}_0 and \mathbf{k}_1 , respectively. Note that the incident waves are coherent and the detector plane is sufficiently long compared to the size of scattering objects. The phase difference is given by the product of the path-length difference and the wave number: $\varphi = (2\pi/\lambda) \times l$. From a relation $\mathbf{k} = (2\pi/\lambda)\mathbf{s}$, we get: $\varphi = -\mathbf{q} \cdot \mathbf{r}$.

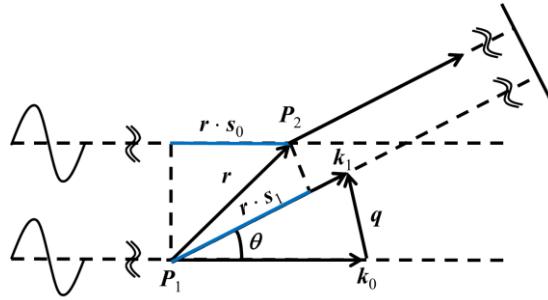


Figure 2.1. Sketch of the scattering vector and a path-length difference between the scattered wave from P_1 and P_2 at a given total scattering angle, θ .

2.1.2. Interference of the scattered waves

The total scattering field $E(\mathbf{q})$ expressed in a complex form is then calculated by summing up all scattered waves over the whole volume of the system V :

$$E(\mathbf{q}) = \int_V \rho(\mathbf{r}) e^{-i\mathbf{q} \cdot \mathbf{r}} d\mathbf{r} \quad (2.2)$$

where $\rho(\mathbf{r})$ is the electron density and $d\mathbf{r}$ is the volume element at a position \mathbf{r} . Mathematically speaking, the total scattering field is given by the Fourier transformation of the electron density distribution in the system.

The electron density distribution can be expressed by the electron density fluctuation

$\Delta\rho(\mathbf{r})$ and its mean value $\bar{\rho}$:

$$\rho(\mathbf{r}) = \bar{\rho} + \Delta\rho(\mathbf{r}) \quad (2.3)$$

The mean electron density is often well approximated as that of solvent at a dilute system.

The total scattering field is then rewritten as

$$E(\mathbf{q}) = \int_V \bar{\rho} e^{-i\mathbf{q}\cdot\mathbf{r}} d\mathbf{r} + \int_V \Delta\rho(\mathbf{r}) e^{-i\mathbf{q}\cdot\mathbf{r}} d\mathbf{r} \quad (2.4)$$

where the linearity of the Fourier transformation is used. The first term in the right-hand side contributes to the data at the zero scattering vector ($\mathbf{q} = 0$) because the Fourier transformation of a constant gives a delta function. This contribution itself has never been observed by experiments due to elimination with a beam stop or hindrance of the primary beam. Therefore, the total scattering field is represented by the Fourier transformation of the electron density fluctuation

$$E(\mathbf{q}) = \int_V \Delta\rho(\mathbf{r}) e^{-i\mathbf{q}\cdot\mathbf{r}} d\mathbf{r} \quad (2.5)$$

Practically, an accessible quantity of the scattering experiment is only the scattering intensity averaged over time and ensemble as:

$$I(q) = \langle |E(\mathbf{q})|^2 \rangle \quad (2.6)$$

Let us consider a systems consisting of N individual particles. By introducing the field $F_k(\mathbf{q})$ scattered by the particle labeled by k as:

$$F_k(\mathbf{q}) = \int_{V_k} \Delta\rho(\mathbf{r}_k) e^{-i\mathbf{q}\cdot\mathbf{r}_k} d\mathbf{r}_k \quad (2.7)$$

the scattering intensity is described as:

$$I(q) = \sum_{k=1}^N \langle |F_k(\mathbf{q})|^2 \rangle = N \langle |F(\mathbf{q})|^2 \rangle \quad (2.8)$$

where the $|F(\mathbf{q})|^2$ is the statistically averaged intensity of $|F_k(\mathbf{q})|^2$. Note that any translational or orientational symmetry, i.e., long-range order, does not exist in the system

or their effects are incorporated into $|F(\mathbf{q})|^2$. The amplitude of $F(\mathbf{q})$ is given by:

$$|F(\mathbf{q})|^2 = F(\mathbf{q}) \cdot F^*(\mathbf{q}) = \iint_V \Delta\rho(\mathbf{r}_1)\Delta\rho(\mathbf{r}_2)e^{-i\mathbf{q}\cdot(\mathbf{r}_1-\mathbf{r}_2)} d\mathbf{r}_1 d\mathbf{r}_2 \quad (2.9)$$

where V is the volume of the particle. By putting $\mathbf{r}_2 - \mathbf{r}_1 = \mathbf{r}$, we have:

$$|F(\mathbf{q})|^2 = \iint_V \Delta\rho(\mathbf{r}_1)\Delta\rho(\mathbf{r}_1 + \mathbf{r})e^{i\mathbf{q}\cdot\mathbf{r}} d\mathbf{r}_1 d\mathbf{r} \quad (2.10)$$

Note that $\mathbf{r}_2 = \mathbf{r}_1 + \mathbf{r}$ and $d\mathbf{r}_2$ corresponds to $d\mathbf{r}$. We introduce the spatial auto-correlation function $\gamma(\mathbf{r})$, which is also called the convolution square $\Delta\tilde{\rho}^2(\mathbf{r})$ in mathematics, as:

$$\gamma(\mathbf{r}) \equiv \Delta\tilde{\rho}^2(\mathbf{r}) = \int_V \Delta\rho(\mathbf{r}_1)\Delta\rho(\mathbf{r}_1 + \mathbf{r}) d\mathbf{r}_1 \quad (2.11)$$

Substitution of equation (2.11) into equation (2.10) gives:

$$|F(\mathbf{q})|^2 = \int_V \gamma(\mathbf{r})e^{i\mathbf{q}\cdot\mathbf{r}} d\mathbf{r} \quad (2.12)$$

This equation demonstrates that the intensity is given by the Fourier transformation of the spatial auto-correlation function of the density fluctuation.

An orientational averaging process gives the real space functions only depending on the distance in the radial direction r and the intensity as a function of the magnitude of the scattering vector, i.e., the intensity distribution in azimuthal angles is not found. The orientational average of the spatial auto-correlation function and the phase factor is given by

$$\gamma(r) = \langle \Delta\tilde{\rho}^2(\mathbf{r}) \rangle = \left\langle \int_V \Delta\rho(\mathbf{r}_1)\Delta\rho(\mathbf{r}_1 + \mathbf{r}) d\mathbf{r}_1 \right\rangle \quad (2.13)$$

and

$$\langle e^{i\mathbf{q}\cdot\mathbf{r}} \rangle = \frac{\sin(qr)}{qr} \quad (2.14)$$

By using equations (2.8), (2.10), (2.11), (2.12), (2.13), (2.14), the scattering intensity from the particle is given by:

$$\begin{aligned}
I(q) &= \langle |F(\mathbf{q})|^2 \rangle = \langle \int_V \Delta\tilde{\rho}^2(\mathbf{r}) e^{i\mathbf{q}\cdot\mathbf{r}} d\mathbf{r} \rangle \\
&= 4\pi \int_0^\infty \Delta\tilde{\rho}^2(r) \frac{\sin(qr)}{qr} r^2 dr \\
&= 4\pi \int_0^\infty \gamma(r) r^2 \frac{\sin(qr)}{qr} dr \\
&= 4\pi \int_0^\infty p(r) \frac{\sin(qr)}{qr} dr \quad (2.15)
\end{aligned}$$

where $p(r) = \gamma(r)r^2$ is the pair distance distribution function. Note that the variables are converted to polar coordinates. Therefore, the scattering intensity from a particle, which is often called the form factor $P(q)$ in colloidal science, is given by the Fourier transformation of the pair distance distribution function.

2.1.3. Instruments for the measurement of small- and wide-angle x-ray scattering

I performed simultaneous small- and wide-angle x-ray scattering (SWAXS) experiments on a variety of soft-matters, such as aqueous solutions of protein and thermo-responsive polymers, and aqueous dispersions of cationic surfactant, using a SAXSess camera (Anton Paar, Austria). The experimental setup used in this study is shown in Figure 2.2. A primary beam generated by a sealed tube anode x-ray generator (GE Inspection Technologies, Germany, operated at 40 kV and 50 mA) is condensed by a focusing multilayer optics, and a block collimator enables to shape the condensed primary beam into a well-defined line shape (ca. 20 mm \times 300 μ m), which provides an intense monochromatic primary beam of Cu- $K\alpha$ radiation (0.1542 nm wavelength). Liquid samples are filled into a vacuum tight quartz capillary cell (ca. 1 mm diameter) and set in a temperature controlled sample holder unit TCS120 (Anton Paar, Austria). The sample temperature was controlled with an accuracy of ± 0.1 $^\circ$ C. Use of a semi-transparent beam

stop allows us to measure the primary beam propagated through the samples at zero scattering vector. Two-dimensional scattering intensity profile recorded by an imaging-plate detector was read out by a Cyclone storage phosphor system (Perkin Elmer, USA).

The recorded two-dimensional intensity was integrated into a one-dimensional scattering curve, $I(q)$, as a function of the magnitude of the scattering vector

$$q = \frac{4\pi}{\lambda} \sin\left(\frac{\theta}{2}\right) \quad (2.16)$$

where λ is the wavelength of x-rays and θ is the total scattering angle. An accessible range of the total scattering angle of the SAXS camera is between 0.1 and 40 degrees, corresponding to the q -range of 0.07–28 nm⁻¹. All $I(q)$ data were normalized to attain a uniform primary intensity at $q = 0$ for transmission calibration. The background scattering contributions caused by the quartz capillary cell and solvent were corrected. In this procedure, both transmittance difference between solvent and solution and solute (or solvent) concentration were taken into account. The background-corrected intensity was further calibrated to an absolute intensity by referring to water intensity as a secondary standard [1], for which the reference value of the forward scattering intensity of water, 0.01633 cm⁻¹ (at 25°C), is used. Broadening (smearing) effects of the scattering curves measured by a line collimation apparatus was corrected relying on the Lake algorithm [2]. In this ‘desmearing’ procedure, an ideal scattering intensity practically equivalent to that measured by a point-collimation apparatus is iteratively calculated based on the following relationship

$$I_S(q) = \iint_{-\infty}^{+\infty} W_z(z)W_y(y)I[\sqrt{(q-y)^2 + z^2}]dydz \quad (2.17)$$

where $I_S(q)$, $W_z(z)$, and $W_y(y)$ are the smeared scattering intensity, the normalized length and width profiles of the primary beam, respectively.

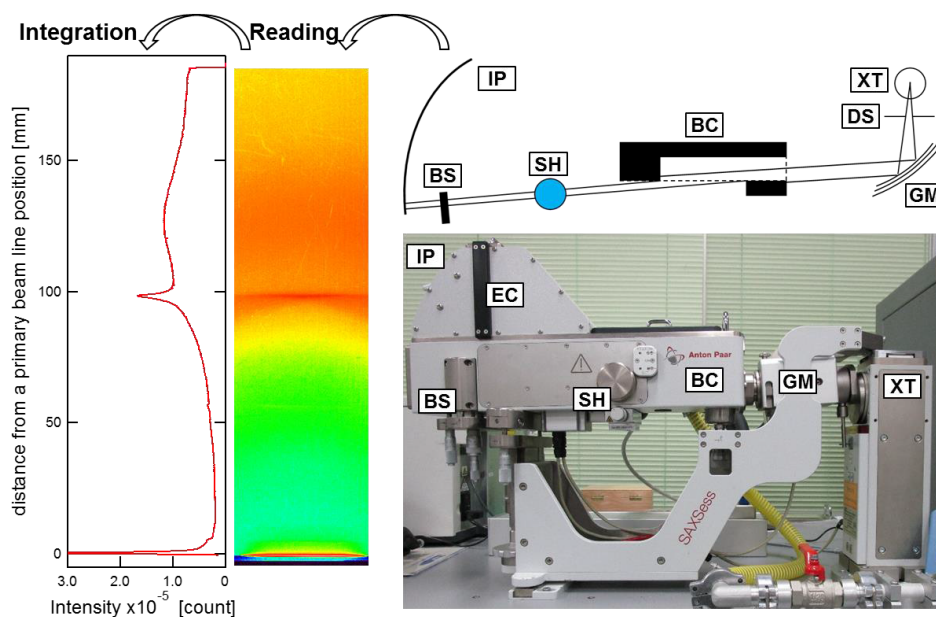


Figure 2.2. Instruments for the measurement of small- and wide-angle x-ray scattering intensities (SAXSess camera). **XT** represents x-ray tube; **DS** divergence slit; **GM** Göbel mirror; **BC** block collimator; **SH** sample holder; **BS** semi-transparent beam stop; **IP** imaging plate; **EC** evacuatable chamber. In the upper panel, schematic drawing of the system is shown. A recorded two dimensional scattering profile and a corresponding one dimensional scattering curve are also displayed on the left side.

2.1.4. Instruments for the measurement of small-angle x-ray scattering intensity (point-collimation apparatus)

The scattering intensity obtained by a point collimation system was measured by a pinhole camera, SmartLab (Rigaku, Japan). Figure 2.3 shows a picture of the SmartLab apparatus. The accelerating voltage and the electric current at the target copper were 40 kV and 30 mA, respectively, providing the Cu- $K\alpha$ radiation. The point-like primary beam having a size of ca. 50 μm is produced by passing x-rays through pinholes. A semiconductor detector is able to cover the total scattering angle from 0.25 to 3.5 degrees, which gives the accessible q -range between 0.18 and 2.5 nm^{-1} .

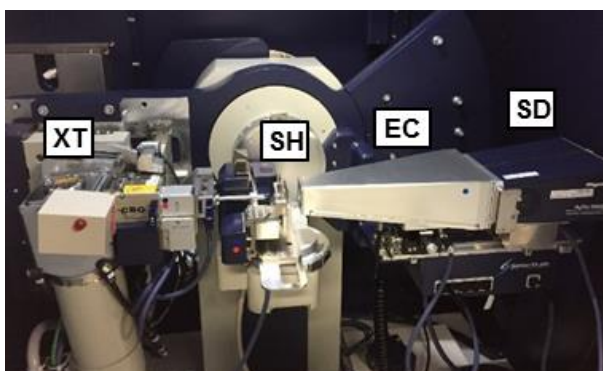


Figure 2.3. A Picture of the point collimation system, SmartLab. **XT** represents x-ray tube; **SH** sample holder; **SD** semiconductor detector, and **EC** evacuatable chamber.

2.2. Dielectric relaxation spectroscopy

The dielectric relaxation spectroscopy (DRS) monitors the dielectric response of polar liquids to an applied time-dependent electric field. Generally, the complex permittivity spectrum is given by the Fourier Laplace transformation of the time correlation function of the total dipole moment of the system. DRS allows us to access information on rotational diffusion of solute molecules, counterion fluctuations, and hydration states.

2.2.1. Time domain reflectometry

Dielectric properties of the sample from MHz to tens of GHz frequency was determined by time domain reflectometry (TDR). The experimental setup is sketched in Figure 2.4. The pulse generator and sampling head are equipped with four channel test set, HP54121A (Hewlett-Packard). A step-like pulse produced by the pulse generator, $V_i(t)$, propagates through a coaxial line and is applied to the sample placed at the end of the line. The reflected wave, $V_r(t)$, is stored and displayed at the digital oscilloscope HP54120B (Hewlett-Packard) after digitizing the data recorded by sampling head. The frequency

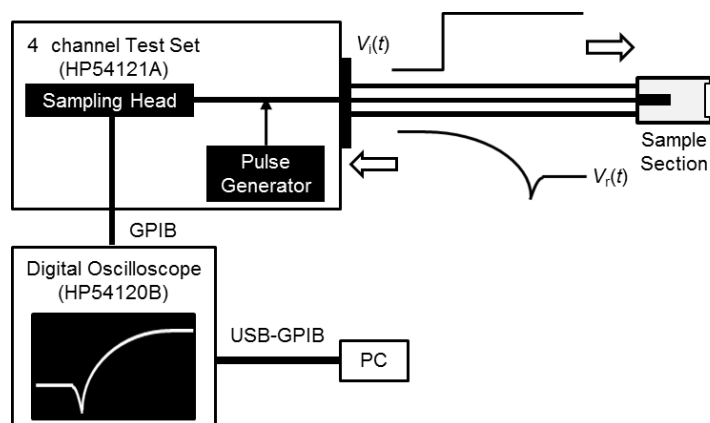


Figure 2.4. Block diagram of the time domain reflectometer. The applied and reflected signals are represented by $V_i(t)$ and $V_r(t)$, respectively.

domain spectra is obtained via the Laplace transformation of the time-dependent reflected waveforms.

The total reflection coefficient of the sample cell, $\rho(\omega)$, is defined by using the Laplace transformation of the incident, $V_i(\omega)$, and reflected, $V_r(\omega)$, waves [3]

$$\rho(\omega) = \frac{c}{gd} \frac{V_i(\omega) - V_r(\omega)}{i\omega(V_i(\omega) + V_r(\omega))} \quad (2.18)$$

where ω , g , and d is the angular frequency, the relative feeding line impedance against the impedance of the empty cell, and the electric cell length, respectively. Note that the product of gd is the cell constant. The generalized complex permittivity, $\eta(\omega)$, is obtained from the total reflection coefficient

$$\eta(\omega) = \rho(\omega) x \cot x ; x = (\omega d/c) \sqrt{\eta(\omega)} \quad (2.19)$$

It is difficult to determine the incident and reflected waves simultaneously. This problem can be avoid by referring a standard sample of known permittivity, $\eta_s(\omega)$. Typically, air can be an appropriate standard sample. The relative reflection coefficient, $\rho_r(\omega)$, is given by

$$\rho_r(\omega) = \frac{c}{gd} \frac{V_s(\omega) - V_x(\omega)}{i\omega(V_s(\omega) + V_x(\omega))} \quad (2.20)$$

where $V_s(\omega)$ and $V_x(\omega)$ are the Laplace transformation of the reflected wave of the reference standard sample and the unknown sample, respectively. The generalized complex permittivity of the sample, $\eta_x(\omega)$, is obtained by the following equation

$$\eta_x(\omega) = \frac{(\rho_r(\omega) + \eta_s(\omega)/f_s)f_x}{1 - g^2(\omega d/c)^2 \rho_1(\eta_s(\omega)/f_s)} \quad (2.21)$$

with $f_s = x_s \cot(x_s)$ and $f_x = x_x \cot(x_x)$.

The direct current (DC) conductivity of samples is evaluated from the amplitude of the reflected wave. For conducting samples, the voltage amplitude of the reflected wave at the long-time limit, $V_x(\infty)$, is reduced compared to that for the non-conducting standard

sample, $V_s(\infty)$, (see Figure 2.5.). This effect can be eliminated by introducing a parameter $h = V_x(\infty) / V_s(\infty)$ and the value of the DC conductivity, κ , is evaluated by the following relation

$$\kappa = \frac{\varepsilon_0 c}{gd} \frac{1-h}{1+h} \quad (2.22)$$

In this study, I employed the so-called time-window divided modified direct (TDMD) method reported by Sato and Buchner [6], in which I used multiple time windows having a relatively short time/div of a digitizing oscilloscope (HP54120B). For these individual waveform measurements of the reflected pulse from the standard and unknown samples, optimized different delay times were chosen. Then, these multiple planes were united into one total waveform. This procedure can increase a time resolution of the time domain measurements, simultaneously attaining the full length of time windows for the sufficient low-frequency limit of the complex permittivity.

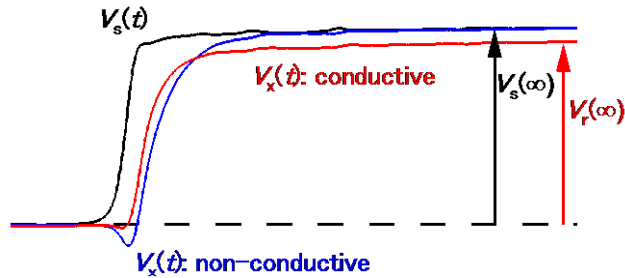


Figure 2.5. Schematic representation of the reflected waveforms from (black) standard reference and (blue) non-conductive and (red) conductive sample.

2.2.2. Vector network analysis

The vector network analyzer (VNA) is able to characterize dielectric properties of samples in a high frequency region (typically above 1 GHz) by accurately measuring the amplitude and the phase in the frequency domain. Electrical behavior of the two-port device including the device under tested is analyzed via the scattering parameter matrix,

\hat{S} ,

$$\begin{pmatrix} \hat{b}_1 \\ \hat{b}_2 \end{pmatrix} = \begin{pmatrix} \hat{S}_{11} & \hat{S}_{12} \\ \hat{S}_{21} & \hat{S}_{22} \end{pmatrix} \begin{pmatrix} \hat{a}_1 \\ \hat{a}_2 \end{pmatrix} \quad (2.23)$$

where a_j and b_j indicate incident and reflected waves at a port j , respectively. The \hat{S}_{jj} parameter corresponds to the reflection coefficient, which is required for the calculation of the complex permittivity. From a practical point of view, the scattering parameter measured by VNA, \hat{S}_{jj}^m , does not match the actual one, \hat{S}_{jj}^a . The correction of the systematic errors from directivity, \hat{e}_d , frequency response, \hat{e}_r , and source match, \hat{e}_s , was made according to the relation [7]

$$\hat{S}_{jj}^m = \hat{e}_d \frac{\hat{e}_r \hat{S}_{jj}^a}{1 - \hat{e}_s \hat{S}_{jj}^a} \quad (2.24)$$

Therefore, the calibration with open, short, and load is needed. In the case of one-port measurements characterized by an impedance step from \hat{Z}_1 to \hat{Z}_2 , the \hat{S}_{11} parameter can be related to the normalized aperture impedance, $\hat{Y} = \hat{Z}_2 / \hat{Z}_1$, via

$$\hat{S}_{11} = \frac{1 - \hat{Y}}{1 + \hat{Y}} \quad (2.25)$$

Based on a simplified coaxial aperture opening model, the complex dielectric properties, $\hat{\eta}_m$, is calculated from the normalized aperture impedance by numerically solving the following equation [7]

$$\hat{Y} = \frac{i \hat{k}_m^2}{\pi \hat{k}_c \ln(D/d)} \left[i \left(I_1 - \frac{\hat{k}_m^2 I_3}{2} + \frac{\hat{k}_m^4 I_5}{24} - \frac{\hat{k}_m^6 I_7}{720} + \dots \right) + \left(I_2 \hat{k}_m - \frac{\hat{k}_m^3 I_4}{6} + \frac{\hat{k}_m^5 I_6}{120} - \dots \right) \right] \quad (2.26)$$

where $\hat{k}_m = \omega \sqrt{\hat{k}_m \epsilon_0 \mu_0}$ is the propagation constant of the sample, $\hat{k}_c = \omega \sqrt{\hat{k}_c \epsilon_0 \mu_0}$ is the propagation constant within the dielectric material of the coaxial probe head, and d and D are the radii of the inner and outer conductor of the coaxial line, respectively. The optimized probe constants, I_n , is implemented in the Agilent 85070C software package.

Dielectric spectra in the frequency range between 0.2 and 50 GHz were determined with a VNA E8364B (Agilent) equipped with a dielectric probe kit 85070E (Agilent). The probe kit comprises two distinct probes, the high temperature cell (85070E-020) suitable for the low frequency measurements ($0.2 \leq \nu/\text{GHz} \leq 20$) and the performance cell (85070E-050) for the high frequency measurements ($1.0 \leq \nu/\text{GHz} \leq 50$). They are both mounted in a thermostated cell and temperature was controlled ± 0.03 °C. The equipment was calibrated with air, mercury, and water. The experimental setup can be seen in Figure 2.6.

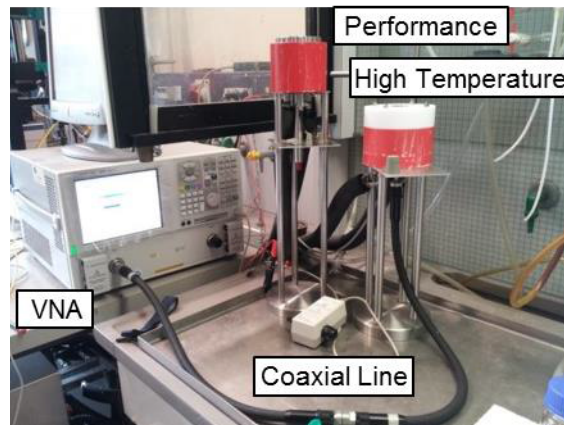


Figure 2.6. Instruments for the measurements of dielectric spectra using the vector network analyzer E8364B combined with a dielectric probe kit 85070E-020 (high temperature cell) and 85070E-050 (performance cell).

2.2.3. Waveguide interferometry

Waveguide interferometers are used to determine the permittivity in the millimeter wave frequency region. A picture of E-band interferometer installed at Regensburg University is shown in Figure 2.7. A monochromatic wave of frequency is split into measuring and reference paths. A wave passing through the sample cell and phase shifters interferes that propagating a precision attenuator. A relative signal amplitude of the interference wave is measured by the receiver. The interference curve, $A(z - z_0)$, is then determined by varying

the relative probe position, z , from the adjusted interference minimum, z_0 , in the sample path.

The attenuation coefficient, α , and wavelength, λ_m , of the sample can be obtained by fitting the interference function to the experimental data [8]

$$A(z_0 - z'_0) = A_0 + 10 \log \left\{ 1 + \exp[-2p\alpha(z_0 - z'_0)] - 2 \cos \left(\frac{2\pi}{\lambda_m} (z_0 - z'_0) \right) \cdot \exp[-2p\alpha(z_0 - z'_0)] \right\} \quad (2.27)$$

where A_0 is the relative intensity of the signal passing through the sample beam and $p = (20 \log_e \text{ dB/Np})^{-1}$ is the conversion factor. The permittivity of the sample is expressed by these quantities

$$\eta'(\nu) = \left[\left(\frac{1}{\lambda_c^{\text{vac}}} \right)^2 + \left(\frac{1}{\lambda_m} \right)^2 - \left(\frac{\alpha}{2\pi} \right)^2 \right] \left(\frac{c_0}{\nu} \right)^2 \quad (2.28)$$

$$\eta''(\nu) = \frac{\alpha}{\pi \lambda_m} \left(\frac{c_0}{\nu} \right)^2 \quad (2.29)$$

with the limiting vacuum frequency, λ_c^{vac} .

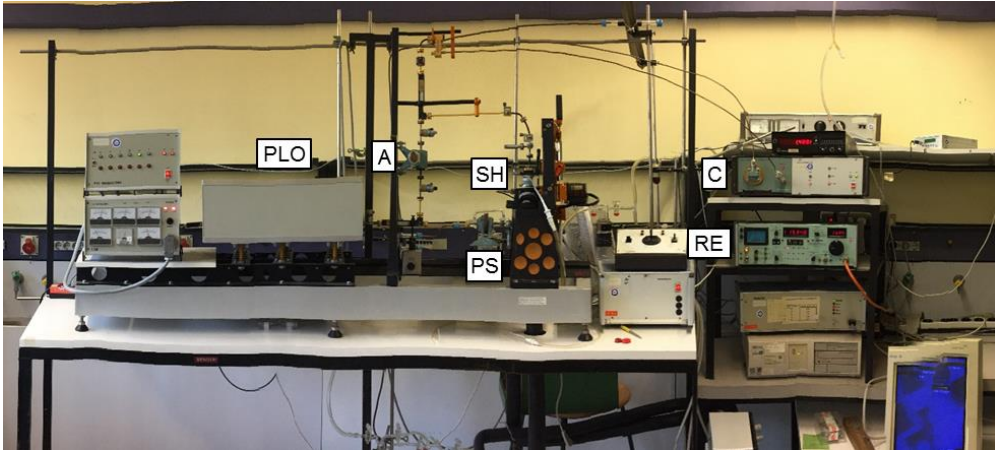


Figure 2.7. A waveguide interferometer measuring the permittivity at frequencies of the E-band. **PLO** phase locked oscillators; **A** variable precision attenuator; **PS** precision phase shifter; **SH** sample holder; **C** converter; **RE** precision receiver.

2.2.4. Data processing of dielectric spectra

A series of relaxation models based on a superposition of n -Havriliak–Negami equations, or its simpler counterparts, such as Debye, Cole-Cole, and Davidson-Cole equations, are thoroughly tested to give a quantitative and consistent description of the experimental spectra [9],

$$\varepsilon^*(\nu) = \varepsilon_\infty + \sum_{j=1}^n \frac{\Delta\varepsilon_j}{\left[1 + (i2\pi\nu\tau_j)^{\beta_j}\right]^{\alpha_j}} \quad (2.30)$$

A j th dispersion step ($j = 1, 2 \dots$ and n) is defined according to the magnitude of its relaxation time, τ_j ($\tau_j > \tau_{j+1}$), where n is the number of separable dispersion steps, ε_∞ is the infinite frequency permittivity, and α_j and β_j are the shape parameters representing asymmetric [10] and symmetric [11] broadening of the spectrum shape, respectively. The experimental complex permittivity is simultaneously fitted by using the Levenberg-Marquardt algorithm. Note that for the spectra obtained by the VNA measurement, DC conductivity arising from ionic impurity of the sample is subtracted as an adjustable parameter, while that is determined from waveform amplitude in the case of the TDR measurement.

The problem of the fitting procedure is that plausible representation is not unique due to broad shape of the spectrum. To find an appropriate model, following criteria should be used. First, the reduced error function, χ_r^2 , should be small. This function is a measure of the quality of the fit and is described as

$$\chi_r^2 = \frac{1}{2N - m - 1} \left[\sum_{k=1}^N \delta\varepsilon'(v_k)^2 + \sum_{k=1}^N \delta\varepsilon''(v_k)^2 \right] \quad (2.31)$$

where $\delta\varepsilon'$ and $\delta\varepsilon''$ are the residuals, N is the number of data set, and m is the number of

adjustable parameters. Second, the number of relaxation modes should be reasonably small. Third, the fitting model should be consistent at investigated concentration or temperature, except for specific physical reasons. Fourth, the obtained fitting parameters should be physically reasonable.

2.3. Auxiliary measurements

2.3.1. Densimetry

Density measurements were carried out using a vibrating tube densimeter, DMA4500M (Anton Paar, Austria). A U-shaped borosilicate glass tube filled with the sample is vibrated at a characteristic frequency depending on the sample density. The instrument measures the period of the vibration, τ , yielding density

$$\rho = A \left(\frac{\tau}{\tau_0} \right)^2 f_1 - B f_2 \quad (2.32)$$

where A and B are apparatus constants, τ_0 is the period of a reference oscillator, and f_1 and f_2 are factors correcting temperature, viscosity, and non-linearity effects. Before measurements, a density check of air and water was performed. Temperature is controlled within the accuracy of 0.01 °C and the precision of the density is 1×10^{-5} g/cm³.

2.3.2. Viscometry

Shear viscosities in the shear rate range of 0.01–1000 s⁻¹ were measured on an MCR92 rheometer (Anton Paar, Austria) equipped with a cone-plate measuring device.

2.3.3. Optical microscopy

Microscopy observations were performed with an inverted microscope Eclipse Ts2 (Nikon, Japan). A drop of the sample was placed onto a 1 mm thick microscope slide, and the specimen was covered by a thin cover glass to prevent solvent from evaporating. Scale bars are determined by referring length of the hemocytometer.

References

- [1] D. Orthaber, A. Bergmann, and O. Glatter, *J. Appl. Crystallogr.* 33, 218-225 (2000).
- [2] J.A. Lake, *Acta Crystallogr.* 23, 191-194 (1967).
- [3] T.K. Bose and R. Nozaki, *J. Mol. Liq.* 56, 399-417 (1993).
- [4] R. Nozaki and T.K. Bose, *IEEE Trans. Instrum. Meas.* 39, 945-951 (1990).
- [5] R. Buchner and J. Barthel, *Ber. Bunsen-Ges. Phys. Chem.* 101, 1509-1516 (1997).
- [6] T. Sato and R. Buchner, *J. Phys. Chem. A* 108, 5007-5015 (2004).
- [7] D.V. Blackham and R.D. Pollard, *IEEE Trans. Instrum. Meas.* 46, 1093-1099 (1997).
- [8] J. Barthel, K. Bachhuber, R. Buchner, H. Hetzenauer, and M. Kleebauer, *Ber. Bunsen-Ges. Phys. Chem.* 95, 853-859 (1991).
- [9] S. Havriliak and S. Negami, *Polymer* 8, 161-210 (1967).
- [10] K.S. Cole and R.H. Cole, *J. Chem. Phys.* 9, 341-351 (1941).
- [11] D.W. Davidson and R.H. Cole, *J. Chem. Phys.* 18, 1417-1417 (1950)

Chapter 3.

Microglobule formation and a microscopic order parameter monitoring the phase transition of aqueous poly(*N*-isopropylacrylamide) solution

The coil-to-globule transition of poly(*N*-isopropylacrylamide) (pNIPAm) in water is generally believed to be driven by hydrophobic interaction between the isopropyl groups of its side chains. However, it is still unclear how dehydration and critical fluctuations of the polymer chains are correlated. Here, we use small- and wide-angle x-ray scattering and dielectric relaxation spectroscopy to cover a wide range of the relevant length and time scales, enabling us to grasp an overall picture of this phase transition. We find that the hydration number of pNIPAm decreases only moderately with temperature up to about 6 K below its spinodal temperature T_S , but then drops steeply on approaching T_S . This rapid dehydration is coupled to a mean-field-like power-law divergence of the correlation length ξ , representing fluctuations of the density order parameter. Real-space decoding of an observed interference peak reveals partial-globule formation even far below T_S and demonstrates that the polymer-rich phase above T_S can be understood as a high-density assembly of the microglobules. Strikingly, condensation of the microglobules and the divergence of ξ do not run parallel. Instead, the microglobule-condensation occurs only above T_S and is completed about 6 K above T_S . The local number density of the microglobules, exhibiting a steplike increase just above T_S , should be identified as an additional microscopic order parameter governing the phase transition of pNIPAm.

3.1. Introduction

Phase transitions and critical phenomena in polymer solutions have a host of implications for the self-organization of amphiphilic molecules [1], the collapse of gel networks [2,3], and protein folding [4]. Poly(*N*-isopropylacrylamide) (pNIPAm) is among the most studied thermoresponsive polymers, undergoing a coil-to-globule transition in water at a temperature of approximately 32–34 °C [5–12]. For several decades, hydrophobic interaction has been considered to be the major cause for this collapse of the hydrophobic polymer chain in water.

More detailed mechanisms have been discussed in the literature. ten Wolde and Chandler claimed that solvent fluctuation induced dewetting is an underlying mechanism of the coil-to-globule transition of an ideal hydrophobic polymer chain [13]. Tanaka et al. proposed a cooperative-hydration picture, in which sequential hydrogen bond formation along a pNIPAm chain, triggered by cooperative interactions between nearest neighbor bound water molecules, explains its phase diagram [14,15]. Bischofberger et al. argued that it is the mean energetic state of the aqueous medium that determines hydrophobic hydration in aqueous pNIPAm [16].

Because of unfavorable x-ray scattering contrast, the static structure of pNIPAm was mostly studied by small-angle neutron scattering (SANS) in D₂O solvent. Shibayama et al. [17] showed that SANS intensities of pNIPAm in D₂O solvent recorded for $q \leq 2 \text{ nm}^{-1}$ can be described by a single Ornstein-Zernike (OZ) equation, where q is the magnitude of the scattering vector. Using SANS, Meier-Koll et al. [18] discussed values of the critical exponents describing the critical fluctuation. The high- q deviation from the OZ behavior in the SANS intensities of pNIPAm was tentatively attributed to domain

formation. Although it was pointed out that the transition temperature of pNIPAm in D₂O is 1–2 °C higher than in H₂O [19–21], possible deuterium isotope solvent effects on its critical behavior remain rather ambiguous.

Hydration effects and dynamics of pNIPAm have been extensively studied by spectroscopic techniques [22–32]. Dehydration behavior during the phase transition was investigated by dielectric relaxation spectroscopy (DRS), although the number of experimental data points are limited [24,28]. A recent Raman multivariate curve resolution (Raman-MCR) study of Mochizuki and Ben-Amotz revealed that significant changes in the OH-band frequency range of the spectrum occur only above the cloud-point temperature, where the pNIPAm chains collapse [32]. This unexpected observation appears to be inconsistent with the solvent-fluctuation induced transition mechanism.

Difficulty in reaching a general consensus regarding the counterintuitive phase behavior of aqueous pNIPAm has mostly arisen from the lack of microscopic insights into the coil and globule states. An electron paramagnetic resonance study on pNIPAm-based hydrogels demonstrated the coexistence of hydrophilic and hydrophobic environments over a wide temperature range and suggested that microphase separation takes place in coexisting swollen and collapsed regions during the collapse process [25]. However, the structural details and the role played by the swollen and collapsed domains in the phase transition still remain unclear. Furthermore, although the cooperative-hydration picture predicted partial globule formation even in the one-phase region [14,15], this has not yet been experimentally evidenced. To overcome all these issues, we study the phase transition of semidilute solutions of pNIPAm (M_w 29 kDa) by means of simultaneous small- and wide-angle x-ray scattering (SWAXS) and dielectric relaxation spectroscopy (DRS).

3.2. Experimental Methods

Poly(*N*-isopropylacrylamide) (pNIPAm) having a nominal molecular weight of 19–30 kDa was purchased from Aldrich and was used as received. pNIPAm solutions with polymer weight fraction $w = 0.13$ were prepared by dissolving the polymer in Millipore water (H₂O) and deuterium oxide (D₂O) (Wako, degree of deuteration >99.9%). Before scattering and spectroscopic measurements, the solutions were kept at 5 °C for several days for equilibration.

Small- and wide-angle x-ray scattering (SWAXS) experiments in a scattering vector range of 0.07–28 nm⁻¹ were carried out using a SAXSess camera (Anton Paar, Austria). Sample temperature was controlled with an accuracy of ±0.1 °C. The obtained solution data were corrected for background scattering from the capillary cell and the solvent. To obtain scattering intensities equivalent to those measured by means of an ideal point collimation apparatus, a model independent collimation-correction procedure relying on the Lake algorithm [33] was performed. The measured scattering intensities were converted to absolute values by normalizing to the forward intensity determined for water [34]. As the pNIPAm in the H₂O sample exhibited phase separation above 34 °C, the rotor cell setup was used to prevent precipitation.

Spectra of the complex permittivity $\epsilon^*(\nu)$ of aqueous pNIPAm solutions at identical w were determined in the frequency range between 0.2 and 89 GHz using a vector network analyzer (VNA) (Agilent, E8364B) with open-ended coaxial-line probes (Agilent, 85070E-020/-050) and A- and E-band waveguide interferometers (Regensburg) [35]. The VNA instrument was calibrated with air, mercury, and water. Uncertainty of temperature control was ±0.03 °C.

3.3. Results and Discussion

3.3.1. Static structure

Figures 3. 1(a) and 1(b) show SWAXS intensities $I(q)$ of pNIPAm in H₂O and D₂O respectively as a function of temperature T . For the full description of $I(q)$, a sum of several scattering components is necessary (see Figures 3.2 and 3.3). At low T , the lowest- q portion of $I(q)$ can be entirely described by the Ornstein-Zernike (OZ) equation,

$$I_{\text{OZ}}(q) = \frac{I_{\text{OZ}}(0)}{1 + \xi^2 q^2} \quad (3.1)$$

where ξ is the correlation length and $I_{\text{OZ}}(0)$ is the forward intensity extrapolated to zero scattering vector. The OZ-type contribution reflects the fractal nature of the swollen coil polymer network [36]. With increasing T , the forward intensity increases, whereas simultaneously the shoulder exhibits a significant low- q shift. Additionally, an excess contribution grows in at $q < 0.2 \text{ nm}^{-1}$ and becomes pronounced at $T > 32 \text{ }^\circ\text{C}$. This component can be formally described by the Guinier equation [37],

$$I_{\text{G}}(q) = I_{\text{G}}(0) \exp\left[-\frac{(R_{\text{g}}q)^2}{3}\right] \quad (3.2)$$

where $I_{\text{G}}(0)$ and R_{g} denote the asymptotic Guinier forward intensity and the radius of gyration, respectively. The emergence of this Guinier-type excess forward scattering even at $T < T_{\text{S}}$ appears to indicate that already in the one phase region pNIPAm chains are in an aggregation regime [38].

At all temperatures, two broad interference peaks in the small, respectively wide, angle regime, hereafter called low- q (L) and high- q (H) peaks, can clearly be seen. These contributions, which were outside the reach of previous SANS studies [17,18], are

modeled by Lorentzian parts of the pseudo-Voigt equations [39],

$$I_{V_x}(q) = \frac{I_{V_x}(q_x^*)}{1 + \xi_x^{*2}(q - q_x^*)^2} \quad (3.3)$$

for $x = L$ and H , where q_x^* denotes the peak position and $I_{V_x}(q_x^*)$ is the maximum intensity at $q = q_x^*$; the sharpness parameter ξ_x^* is related to the full width at half maximum (FWHM). The position of the high- q peak, $q_H^* \approx 15\text{--}16 \text{ nm}^{-1}$, remains practically unchanged on variation of T . Judging from the corresponding length scale ($< 0.5 \text{ nm}$), this contribution originates from intrachain radial distributions, i.e., the distance distributions between atoms composing the polymer chains. On the other hand, the emergence of the low- q peak, centered at approximately $3\text{--}6 \text{ nm}^{-1}$ sharply depending on T , manifests the presence of an intermediate-range order, whose length scale is far larger than that of the radial distributions but somewhat smaller than or rather similar to that of the density fluctuations of the swollen polymer network. Note that conventional water soluble random coil polymers, like dextran, often exhibit rod scattering in the similar q range but does not show such an interference peak. Therefore, the temperature dependence of this peak deserves to be scrutinized as it should be the key to a better understanding of the phase behavior of pNIPAm.

Above T_s , $I_{Oz}(0)$ abruptly reduces whereas the forward intensity approaches the Porod scattering limit [37],

$$I_P(q) = K_P q^{-4} \quad (3.4)$$

where K_P is the Porod intensity. This indicates the collapse of the swollen polymer network and the formation of a sharp interface between polymer-rich and water-rich phases. We find a higher value for K_P in D_2O than in H_2O , which is indicative of a greater surface area per unit volume in D_2O .

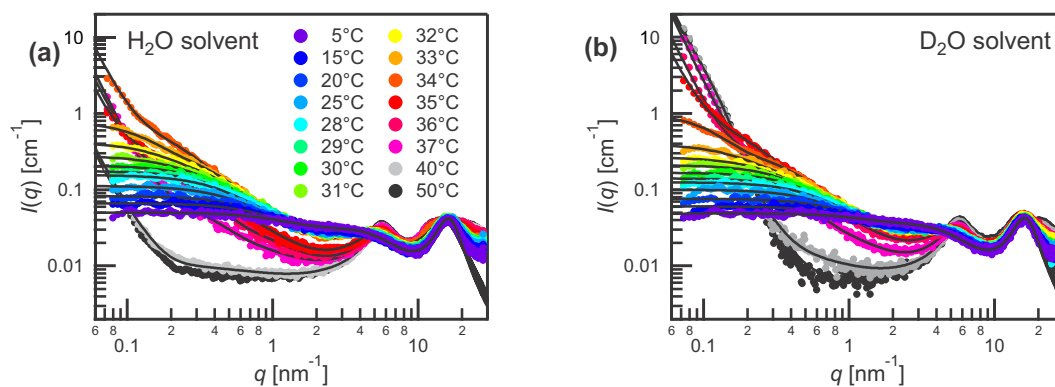


Figure 3.1. Absolute SWAXS intensities $I(q)$ of $w = 0.13$ pNIPAm weight fraction in (a) H₂O and (b) D₂O as a function of T in $5 \leq T/^\circ\text{C} \leq 50$.

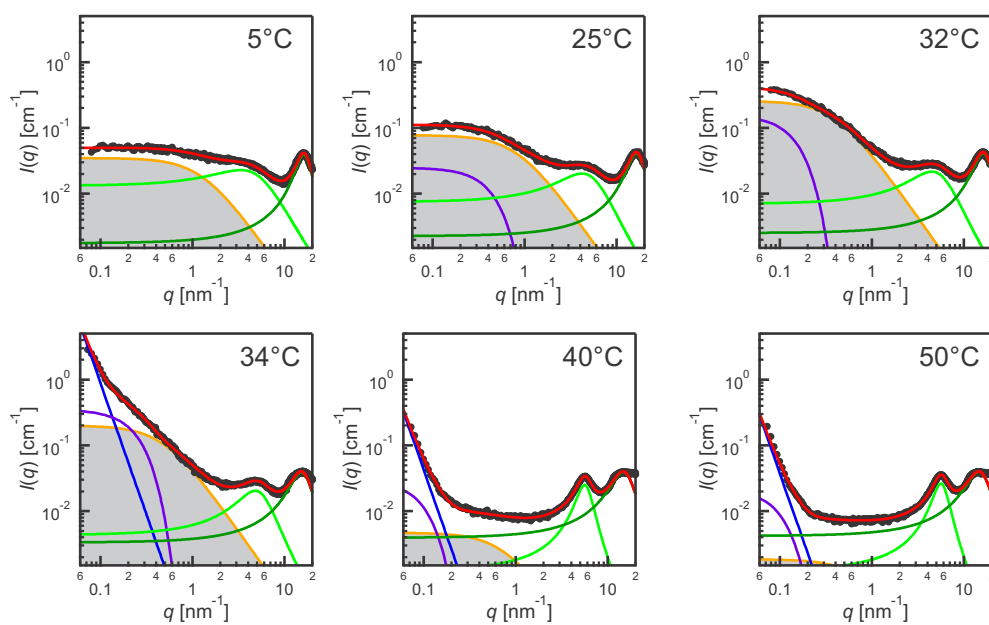


Figure 3.2. Full descriptions of $I(q)$ in H₂O at 5, 25, 32, 34, 40, and 50 °C based on superpositions of several scattering components [equations (3.1–4)].

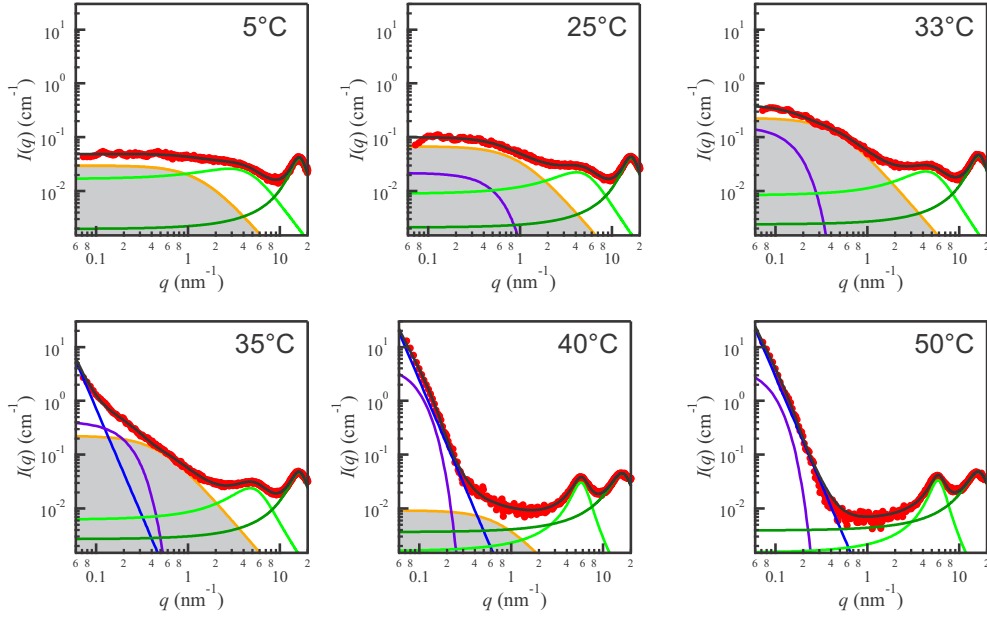


Figure 3.3. Full descriptions of $I(q)$ in D_2O at 5, 25, 33, 35, 40, and 50 °C based on superpositions of several scattering components [equations (3.1–4)].

3.3.2. Critical behavior

Figure 3.4 shows ζ and $I_{OZ}(0)$ of the OZ contribution as a function of T . For semidilute solutions, ζ should be interpreted as the mesh or blob size of the interpenetrating chains [36] whereas $I_{OZ}(0)$ is related to the magnitude of the density fluctuation, being proportional to the osmotic compressibility [40]. We observe simultaneous divergence of ζ and $I_{OZ}(0)$ at the spinodal temperature T_S . Below T_S , these quantities are described by

$$\zeta(T) = \xi_0 |(T - T_S)/T_S|^{-\nu} \quad (3.5)$$

and

$$I_{OZ}(0, T) = I_0 |(T - T_S)/T_S|^{-\gamma} \quad (3.6)$$

where ξ_0 and I_0 are the bare correlation length and forward intensity, respectively, which are treated as T -independent constants. We obtain $T_S = 34.0$ °C in H_2O while $T_S = 34.8$ °C in D_2O . This confirms that substitution of D_2O for H_2O as solvent leads to an increase of

T_S by about 1 K, consistent with the results of previous measurements of macroscopic properties [19–21]. The evaluated critical exponents are $\nu = 0.45$ and $\gamma = 0.80$ in H_2O and $\nu = 0.44$ and $\gamma = 0.80$ in D_2O . Within experimental uncertainty, the values of ν and γ are independent of the solvent conditions and systematically smaller than those predicted by mean-field theory ($\nu = 0.5$ and $\gamma = 1.0$). The present critical exponents are in excellent agreement with those reported in the previous SANS study ($\nu = 0.44$ and $\gamma = 0.81$ in D_2O) [18] despite the necessarily different choice of the fit model for the present $I(q)$ because of the extended q range.

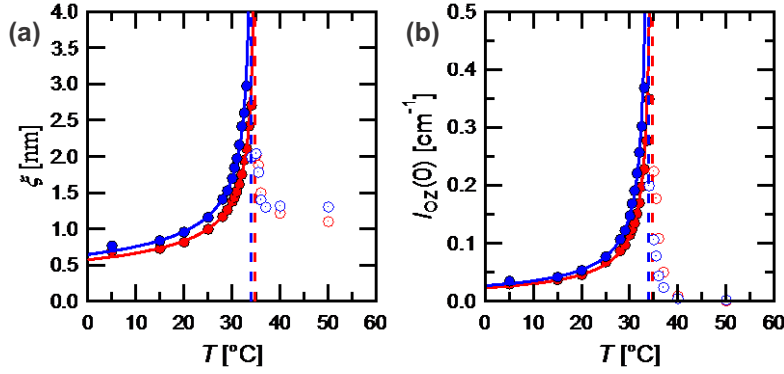


Figure 3.4. Temperature dependence of (a) the correlation length ξ and (b) the asymptotic OZ forward intensity $I_{OZ}(0)$ of semidilute pNIPAm solutions in H_2O (blue) and D_2O (red). Solid lines represent the power-law fits [equations (3.5) and (3.6)] and vertical dashed lines highlight T_S ; open circles indicate the data for temperatures above

3.3.3. Cooperative dynamics

The hydration state of the pNIPAm chains in H_2O is monitored by DRS. Figure 3.5 shows a temperature series of the complex permittivity spectra, $\varepsilon^*(\nu) = \varepsilon'(\nu) - i\varepsilon''(\nu)$, of aqueous pNIPAm, where $\varepsilon'(\nu)$ and $\varepsilon''(\nu)$ are the relative permittivity and dielectric loss, respectively. In the covered frequency range (0.2–89 GHz), the dielectric spectrum of neat water is almost perfectly described by a single Debye-type relaxation function [41].

We find that well below T_s , the addition of pNIPAm induces a marked low-frequency broadening of $\varepsilon''(\nu)$. With increasing T , the spectrum gets narrower. This effect becomes marked especially at $T > T_s - 6$ K.

We find that among the tested models, a superposition of two Debye relaxation functions,

$$\varepsilon^*(\nu) = \frac{\Delta\varepsilon_1}{1 + i2\pi\nu\tau_1} + \frac{\Delta\varepsilon_2}{1 + i2\pi\nu\tau_2} + \varepsilon_\infty \quad (3.7)$$

gives a consistent description of the experimental spectra at all investigated T . Here, the subscripts $j = 1$ and 2 designate the low- and high-frequency relaxations respectively, which are characterized by their relaxation times τ_j ($\tau_1 > \tau_2$) and amplitudes $\Delta\varepsilon_j$ (see Figure 3.6). The loss peak frequency (and thus relaxation time τ_2) of the high-frequency mode is found to be almost identical to that of pure water at all investigated T . Thus, this process is attributed to the cooperative rearrangement of the hydrogen-bond network of bulk water [41]. Its relaxation amplitude $\Delta\varepsilon_2$ reflects the concentration of water molecules behaving as bulk like water in solution. On the other hand, the additional low-frequency mode ($j = 1$) reflects the retarded (slow) dynamics of H₂O molecules in the hydration layer. Here, a contribution from dipolar pNIPAm side chains is possible but—as discussed below—apparently not significant. Segmental motions of the polymer and a possible Maxwell-Wagner-Sillars contribution of the collapsed polymer chain can also be neglected as these relaxations are in the megahertz region [29].

Below 28 °C, $\Delta\varepsilon_1$ shows a moderate decrease with T while $\Delta\varepsilon_2$ remains nearly constant. However, increasing T above 28 °C leads to a pronounced decrease of $\Delta\varepsilon_1$ and a corresponding increase of $\Delta\varepsilon_2$. Such behavior implies that on approaching T_s , water molecules are released from the pNIPAm chains.

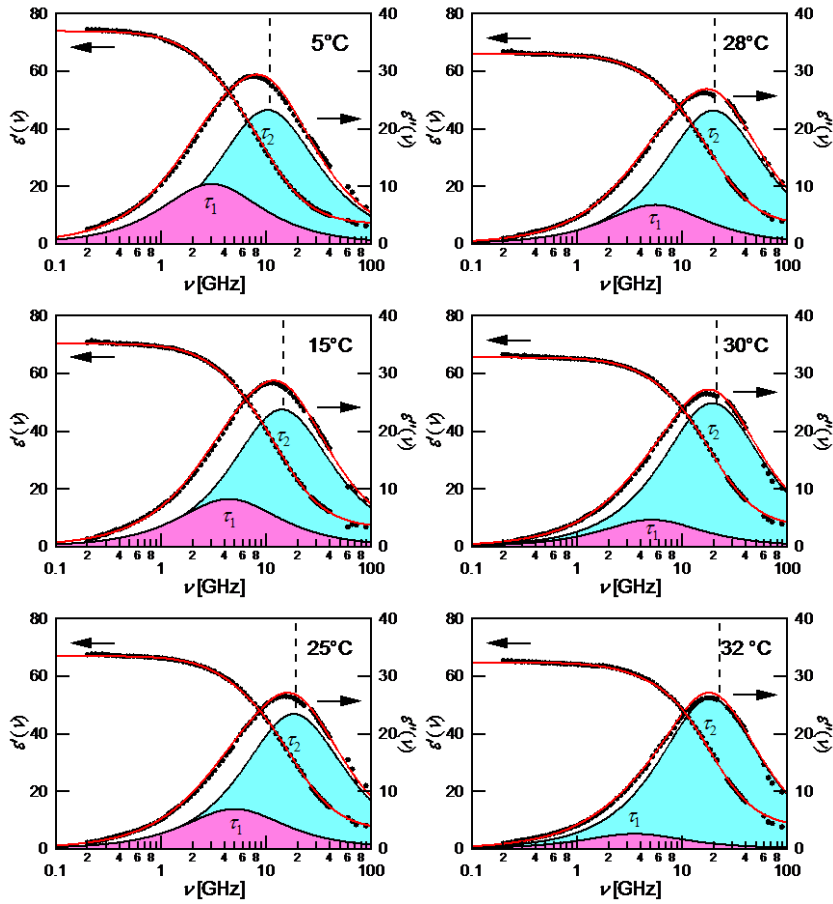


Figure 3.5. Relative permittivity $\varepsilon'(\nu)$ and dielectric loss $\varepsilon''(\nu)$ spectra of pNIPAm ($w = 0.13$) in H_2O at 5°C , 15°C , 25°C , 28°C , 30°C , and 32°C . The red lines are the sum of two Debye relaxation functions [equation (3.7)]. The shaded areas represent the contributions of the resolved modes ($j = 1$ and 2). The vertical dashed lines indicate the loss peak frequency of neat water at identical T .

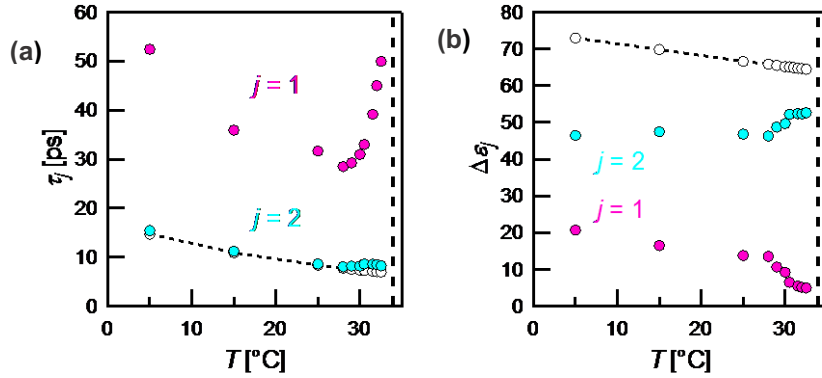


Figure 3.6. (a) Relaxation times τ_j and (b) relaxation amplitudes $\Delta\epsilon_j$ of the resolved modes (filled symbols). The empty symbols in (a) and (b) show the relaxation time and the concentration normalized amplitude of neat water, respectively. The vertical dotted lines highlight T_S .

3.3.4. Hydration/dehydration behavior

To obtain deeper insights into the hydration state of the pNIPAM chains, we evaluate effective hydration numbers per monomer unit using the generalized Cavell equation [42–44],

$$\Delta\epsilon_j = \frac{\epsilon}{\epsilon + (1 - \epsilon)A_j} \frac{N_A}{3k_B T \epsilon_0} \frac{g_j \mu_{Gj}^2}{(1 - \alpha_j f_j)^2} c_j \quad (3.8)$$

where $\Delta\epsilon_j$ is the relaxation amplitude of a j th process, ϵ is the static permittivity, A_j is the cavity-field factor, N_A is the Avogadro constant, k_B is the Boltzmann constant, T is the temperature in kelvin, and ϵ_0 is the vacuum permittivity; c_j is the molar concentration and $\mu_{G,j}$ is the gas-phase dipole moment of the species causing process j , α_j is its polarizability, and f_j is the corresponding reaction-field factor [45]. For water molecules $A_j = 1/3$ (spherical shape) is assumed.

Normalization of equation (3.8) to the expression for neat water yields the apparent concentration $c_j(c)^{\text{app}}$ at solute concentration c as

$$c_j(c)^{\text{app}} = \frac{\varepsilon(0)[2\varepsilon(c) + 1] [1 - \alpha_w f_w(c)]^2 \Delta\varepsilon_j(c)}{\varepsilon(c)[2\varepsilon(0) + 1] [1 - \alpha_w f_w(0)]^2 \Delta\varepsilon_w(0)} c_w(0) \quad (3.9)$$

Substitution of $\Delta\varepsilon_2$ for $\Delta\varepsilon_j$ in equation (3.9) yields the apparent bulk water concentration $c_w(c)^{\text{app}}$. According to the definition, $c_w(c)^{\text{app}}$ can be interpreted as the concentration of water molecules that retain dynamic properties virtually identical to those of pure water despite the presence of solute molecules (pNIPAm). The total hydration number Z_{total} is thus defined as

$$Z_{\text{total}} = \frac{c_w(c)^{\text{ana}} - c_w(c)^{\text{app}}}{c} \quad (3.10)$$

by converting the difference between $c_w(c)^{\text{app}}$ and the analytical concentration of water $c_w(c)^{\text{ana}}$ into the corresponding number of water molecules per pNIPAm repeat unit, where c is the analytical concentration of the latter.

On the other hand, the apparent concentration of slow water $c_{\text{slow}}(c)^{\text{app}}$ can be calculated by substituting $\Delta\varepsilon_1$ for $\Delta\varepsilon_j$ into equation (3.9). The corresponding number of slow water molecules per NIPAm monomer unit is obtained as

$$Z_{\text{slow}} = \frac{c_{\text{slow}}(c)^{\text{ana}}}{c} \quad (3.11)$$

As mentioned before, side-chain dipoles of pNIPAm potentially contribute to $\Delta\varepsilon_1$. However, this should result in Z_{slow} values that are significantly larger than the corresponding data for Z_{total} . According to Figure 3.7 this is not the case, so that the difference between Z_{total} and Z_{slow} can be identified as the number of water molecules that are strongly (irrotationally) bound to the solute, $Z_{\text{ib}} = Z_{\text{total}} - Z_{\text{slow}}$. The obtained hydration numbers Z_{total} , Z_{slow} , and Z_{ib} are summarized in Figure 3.7.

Up to 28 °C, Z_{total} and Z_{slow} show only a moderate decrease with T . However, above that threshold, both hydration numbers rapidly drop. In the identical T range, ζ and $I_{\text{Oz}}(0)$ show a drastic increase (Figure 3.4). This indicates that dehydration of the pNIPAm

chains does not occur monotonously upon heating but proceeds abruptly above $T_S - 6$ K, implying a strong cooperative nature of the pNIPAm dehydration/hydration. The data also demonstrate that the dehydration is strongly coupled to the critical fluctuations of pNIPAm. We therefore infer that the exclusion of hydration water from the vicinity of the pNIPAm chains and the segregation of the system into nanometer-sized polymer-rich and water-rich domains occur in a concerted manner. This is also connected with a drastic slowdown of the hydration water dynamics, i.e., a strong rise of τ_1 [Figure 3.6(a)].

The practically constant value of $Z_{ib} \approx 1.3$ probably means that these irrotationally bound water dipoles are not released from the pNIPAm chains even above T_S . A similar number of strongly bound water molecules was also found for 1,3-dimethylurea in a combined DRS and molecular dynamics study [46] and assigned to H₂O dipoles strongly interacting with the carbonyl oxygen of the solute. This may also be the case for pNIPAm with its amide group in the side chains. Note that the change of the total hydration number upon phase transition, $\Delta Z_{total} \approx 12$, is in good agreement with the result obtained by thermodynamic measurements [47].

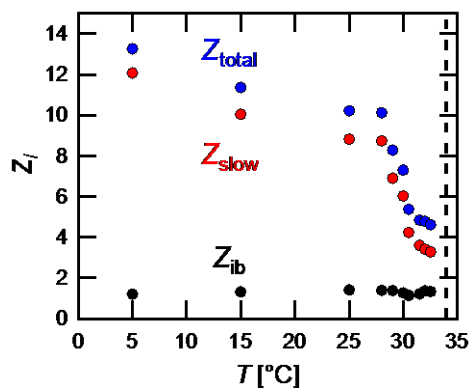


Figure 3.7. Effective hydration numbers Z_i per monomer unit of pNIPAm as a function of temperature. The total Z_{total} and slow water Z_{slow} hydration numbers are evaluated from $\Delta\varepsilon_2(T)$ and $\Delta\varepsilon_1(T)$, respectively. The difference, $Z_{ib} = Z_{total} - Z_{slow}$, gives the corresponding number of apparently “frozen” (irrotationally bound) H₂O molecules.

3.3.5. Microscopic insights into the phase transition

As shown in Figures 3.2 and 3.3, well above T_s , the measured intensities at $q < 8 \text{ nm}^{-1}$ can be approximated as $I_P(q) + I_{VL}(q)$. This means that the polymer-rich phase is virtually homogeneous on a length scale exceeding that of an intermediate-range order ($\sim 1/q_L^*$), while on a shorter length scale, the system exhibits marked density fluctuations. This unambiguously demonstrates that the low- q peak originates from intrinsic density fluctuations in the globule state of pNIPAm. From the emergence of a considerably broader but otherwise similar interference peak at temperatures far below T_s , we argue that already in the one-phase region, an equivalent exists to the positional correlations between high-density scattering objects that characterize the globule state.

A comparable low- q peak was observed for pNIPAm-based gels [48–50]. Our data firmly confirm that the emergence of this low- q peak is not a gel specific phenomenon but an intrinsic property of the pNIPAm chain. Chalal et al. claimed that the peak observed for pNIPAm-based cryogels is due to local packing arising from the hydrophobic association of isopropyl groups of two neighbor chains or from hydrogen bonds between amide groups [48]. However, this explanation cannot apply to pNIPAm solutions because for $T < 28 \text{ }^\circ\text{C}$, the values of the characteristic distance d^* , approximated as $2\pi/q_L^*$ (1.9 nm at $5 \text{ }^\circ\text{C}$ and 1.5 nm at $25 \text{ }^\circ\text{C}$), certainly exceed the corresponding correlation lengths ξ (0.77 and 1.2 nm) [Figures 3. 4(a) and 8(c)].

We are aware that the calculation of the characteristic distance from Bragg's law may be problematic for broad peaks. To overcome these issues, we calculate density autocorrelation functions (ACFs), $C(r)$, using an indirect Fourier transformation (IFT) technique [37] [Figure 3.8(a)], where $C(r)$ is given by the inverse Fourier transformation

of $I(q)$ as

$$I(q) = 4\pi \int r^2 C(r) \frac{\sin(qr)}{qr} dr \quad (3.12)$$

The resulting ACFs in the expression of $r^2C(r)$ are shown in Figure 3.8(b). (Those in D₂O solvent are provided in the Figure 3.9.) The low- q peak is mapped into oscillations in $r^2C(r)$ and the characteristic distance in real space d_r^* can be directly taken from the first peak position [Figure 3.8(c)]. For $T < T_S$, d^* monotonously decreases with T from 1.9 nm at 5 °C to 1.4 nm at 33 °C (just below T_S) while $d_r^* \approx 1.6$ nm remains nearly constant, showing a gentler slope than d^* . Above T_S , both d^* and d_r^* drop significantly and converge to 1.1 and 1.3 nm, respectively. Despite the somewhat different T dependence of d^* and d_r^* , the major point that ζ exceeds d_r^* only above approximately 28 °C is unchanged. These observations lead us to conclude that above T_S , the low- q peak arises from positional correlations between the microglobules and that similar microglobules exist already in the one-phase region ($T < T_S$), as predicted in the cooperative hydration picture [14,15].

Generally, the sharpness of an interference peak is related to the size of organized domains. Using FWHM, $\Delta\beta = 2/\zeta_L^*$, the domain size D is given by $D = 2\pi/\Delta\beta$. By extending a crystallographic method, the (relative) local number density of the microglobules may be deduced as $N_r \propto D/d_r^*$ [Figure 3.8(d)]. The values of N_r exhibit only a moderate increase for $T < T_S$, but show a steplike jump just above T_S , reaching a plateau at $T > 40$ °C. In Figures 3. 8(d) and 8(e), the characteristic T ranges of the divergence of ζ attaining $\zeta > d_r^*$ and the rapid condensation of the microglobules are highlighted in red and green colors, respectively. We stress the fact that the condensation of the microglobules does not occur in parallel with the divergence of ζ . In $T_S < T < T_S + 6K$, where the swollen polymer networks are mostly collapsed, the microglobules rapidly

condense into a high-density state as N_r exhibits a steplike increase. These findings demonstrate that the phase transition of pNIPAm in aqueous media can be viewed as a transition between a state of low density of the microglobules to a state with high microglobule density [Figure 3.8(d)]. Accordingly, we can now identify the local number density of the microglobules as an additional microscopic order parameter monitoring the phase transition [Figure 3.8(e)].

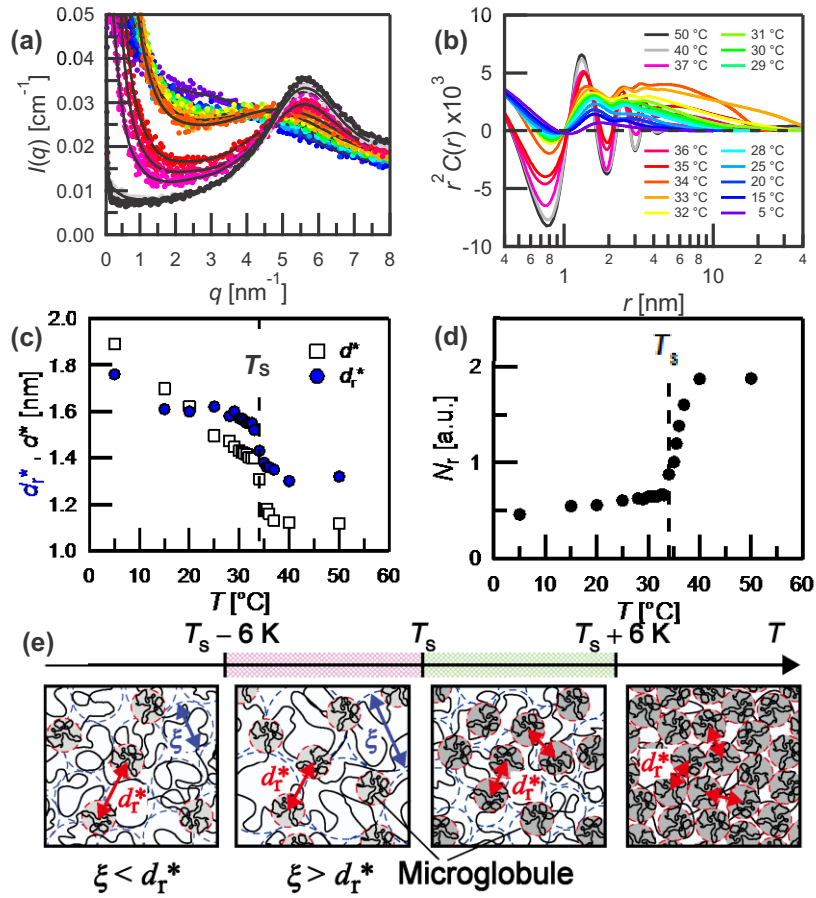


Figure 3.8. Microglobule formation as revealed by SWAXS. (a) Absolute scattering intensity $I(q)$ for scattering vectors $q \leq 8 \text{ nm}^{-1}$ and temperatures $5 \leq T/^\circ\text{C} \leq 50$ (symbols) and fits to $I(q)$ with an indirect Fourier transformation technique (lines). (b) Corresponding density autocorrelation functions $r^2C(r)$ of pNIPAm in H_2O calculated from the $I(q)$ curves shown in (a). Temperature dependence of (c) the characteristic distance obtained by applying Bragg's law ($d_r^* = 2\pi/q_L^*$, empty square) and directly read out from the first (lowest- r) peak position in $r^2C(r)$ (d_r^* , blue filled circle) and (d) the relative local number densities of the microglobules, $N_r \propto \xi_L^*/d_r^*$. (e) Schematic representation of the spatial density fluctuations of pNIPAm at different T values. Far below T_s , where $d_r^* > \xi$, longer-range positional correlations between microglobules yield a broad interference peak. In the range of $T_s - 6 \text{ K} \leq T \leq T_s$, ξ rapidly increases, leading to $\xi > d_r^*$. For $T > T_s$, the density fluctuation arising from the random coil chains rapidly disappears and the local number density of the microglobules shows a steplike increase. The condensation of the microglobules is completed at $T_s + 6 \text{ K}$ and the polymer-rich phase can be understood as a high-density assembly of the microglobules.

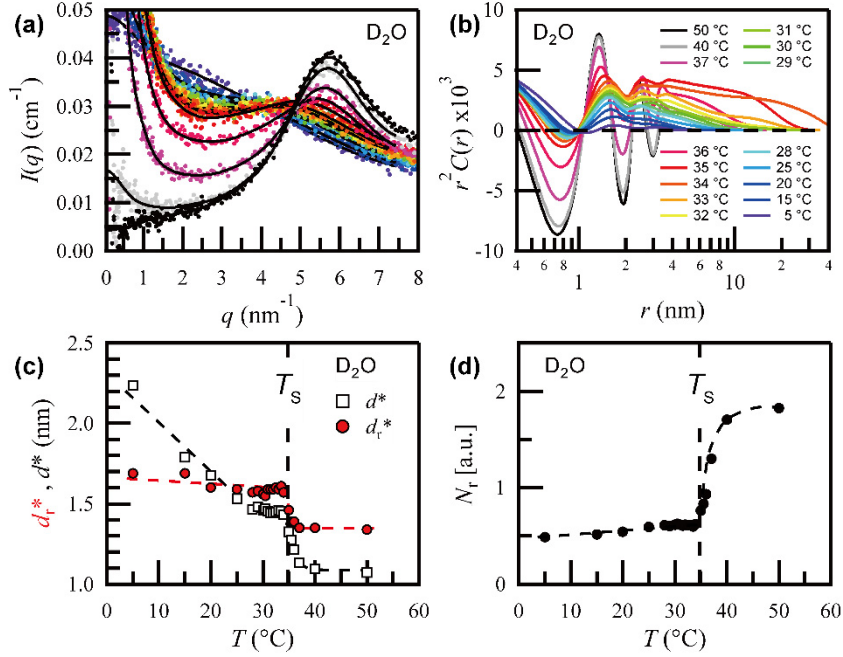


Figure 3.9. (a) Absolute scattering intensities, $I(q)$, for scattering vectors $q \leq 8 \text{ nm}^{-1}$ and temperatures $5 \leq T/^\circ\text{C} \leq 50$ (symbols) and fits to $I(q)$ with an indirect Fourier transformation technique (lines). (b) Corresponding density autocorrelation functions, $r^2C(r)$, of pNIPAM in D_2O calculated from the $I(q)$ curves shown in (a). Temperature dependence of (c) the characteristic distance obtained by applying Bragg's law ($d^* = 2\pi/q_L^*$, empty square) and directly read out from the first (lowest- r) peak position in $r^2C(r)$ (d_r^* , red filled circle) and (d) the relative local number densities of the micro-globules, $N_r \propto \xi_L^*/d_r^*$. Vertical dashed lines in (c) and (b) highlight a spinodal temperature, T_s .

3.4. Conclusions

To summarize, we have presented experimental evidence that critical fluctuations and dehydration of the pNIPAM chains are closely coupled, due to the strong cooperative nature of the dehydration/hydration of the polymer chains. we have also shown similarity and substantial difference of the critical fluctuation of pNIPAM in H_2O and D_2O , confirming about 1 K higher T_s in D_2O and almost identical critical exponents independent of the solvent conditions. The data demonstrate the onset of microglobule

formation far below T_S , where the long-range positional correlations between these microglobules ($d_r^* > \zeta$) give a broad interference peak.

Above T_S the polymer-rich phase is characterized by a high number density state of these microglobules. For $T > T_S - 6\text{K}$, ζ rapidly increases, resulting in $\zeta > d_r^*$. For $T > T_S$, the density fluctuation arising from the random coil chains rapidly disappears, whereas the local number density of the microglobules shows a steplike increase.

Importantly, we find that the condensation of the microglobules does not occur simultaneously with the divergence of ζ . Instead, the condensation sets in just above T_S and is completed at temperatures about 6 K above T_S whereas ζ already diverges when approaching T_S . Therefore, the phase transition of aqueous pNIPAm solution can be understood as a transition from a low-density to a high-density state of the microglobules. Besides the ordinary density order parameter, whose spatial fluctuations are manifested by ζ , the local number density of the microglobules can be identified as a microscopic order parameter governing the phase transition of aqueous pNIPAm solution. The change in solvent water to a weaker hydrogen bond structure above the cloud temperature, claimed by a recent Raman-MCR study [32], may be associated with the completion of the high-density microglobule assemblies.

We note that structural changes related to the volume-phase transition (VPT) of pNIPAm-based gels are often regarded as gel-specific phenomena, but this is probably not correct. As we have shown, many of these changes arise essentially from an intrinsic property of the pNIPAm chain, namely the temperature-induced change of the interchain interactions and the mixing scheme of pNIPAm in aqueous environment. We anticipate that this work has a potential impact on subsequent investigation into effects of coexisting alcohols [15,16,31] and ions on the phase transition of pNIPAm and all kinds of other

thermoreponsive polymers in aqueous media.

References

- [1] D. Chandler, *Nature* 437, 640-647 (2005).
- [2] T. Tanaka, *Phys. Rev. Lett.* 40, 820-823 (1978).
- [3] Y. Hirokawa and T. Tanaka, *J. Chem. Phys.* 81, 6379-6380 (1984).
- [4] K.A. Dill, *Biochemistry* 29, 7133-7155 (1990).
- [5] M. Heskins and J.E. Guillet, *J. Macromol. Sci., Pure Appl. Chem.* 2, 1441-1455 (1968).
- [6] V. Aseyev, H. Tenhu, and F.M. Winnik, in *Self Organized Nanostructures of Amphiphilic Block Copolymers II* (Springer, Berlin, Heidelberg), 29-89 (2011).
- [7] A. Halperin, M. Kröger, and F.M. Winnik, *Angew. Chem., Int. Ed.* 54, 15342-15367 (2015).
- [8] K. Kubota, S. Fujishige, and I. Ando, *J. Phys. Chem.* 94, 5154-5158 (1990).
- [9] C. Wu and S. Zhou, *Macromolecules* 28, 8381-8387 (1995).
- [10] C. Wu and S. Zhou, *Macromolecules* 28, 5388-5390 (1995).
- [11] C. Wu and X. Wang, *Phys. Rev. Lett.* 80, 4092-4094 (1998).
- [12] X. Wang, X. Qiu, and C. Wu, *Macromolecules* 31, 2972-2976 (1998).
- [13] P.R. ten Wolde and D. Chandler, *Proc. Natl. Acad. Sci. U. S. A.* 99, 6539-6543 (2002).
- [14] Y. Okada and F. Tanaka, *Macromolecules* 38, 4465-4471 (2005).
- [15] F. Tanaka, T. Koga, and F.M. Winnik, *Phys. Rev. Lett.* 101, 028302 (2008).
- [16] I. Bischofberger, D. Calzolari, P. De Los Rios, I. Jelezarov, and V. Trappe, *Sci. Rep.* 4, 4377 (2014).
- [17] M. Shibayama, T. Tanaka, and C.C. Han, *J. Chem. Phys.* 97, 6829-6841 (1992).
- [18] A. Meier-Koll, V. Pipich, P. Busch, C.M. Papadakis, and P. Müller-Buschbaum,

Langmuir 28, 8791-8798 (2012).

[19] X. Wang and C. Wu, *Macromolecules* 32, 4299-4301 (1999).

[20] H. Shirota, N. Kuwabara, K. Ohkawa, and K. Horie, *J. Phys. Chem. B* 103, 10400-10408 (1999).

[21] P. Kujawa and F.M. Winnik, *Macromolecules* 34, 4130-4135 (2001).

[22] T. Tokuhira, T. Amiya, A. Mamada, and T. Tanaka, *Macromolecules* 24, 2936-2943 (1991).

[23] Y. Maeda, T. Higuchi, and I. Ikeda, *Langmuir* 16, 7503-7509 (2000).

[24] Y. Ono and T. Shikata, *J. Am. Chem. Soc.* 128, 10030-10031 (2006).

[25] M.J.N. Junk, U. Jonas, and D. Hinderberger, *Small* 4, 1485-1493 (2008).

[26] Z. Ahmed, E.A. Gooding, K.V. Pimenov, L. Wang, and S.A. Asher, *J. Phys. Chem. B* 113, 4248-4256 (2009).

[27] Y. Satokawa, T. Shikata, F. Tanaka, X.-p. Qiu, and F.M. Winnik, *Macromolecules* 42, 1400-1403 (2009).

[28] M. Füllbrandt, E. Ermilova, A. Asadujjaman, R. Hölzel, F.F. Bier, R. von Klitzing, and A. Schönhal, *J. Phys. Chem. B* 118, 3750-3759 (2014).

[29] M. Yang, C. Liu, and K. Zhao, *Phys. Chem. Chem. Phys.* 19, 15433-15443 (2017).

[30] M. Yang, W. Su, and K. Zhao, *J. Polym. Sci., Part B: Polym. Phys.* 55, 1859-1864 (2017).

[31] M. Yang and K. Zhao, *J. Polym. Sci., Part B: Polym. Phys.* 55, 1227-1234 (2017).

[32] K. Mochizuki and D. Ben-Amotz, *J. Phys. Chem. Lett.* 8, 1360-1364 (2017).

[33] J.A. Lake, *Acta Crystallogr.* 23, 191-194 (1967).

[34] D. Orthaber, A. Bergmann, and O. Glatter, *J. Appl. Crystallogr.* 33, 218-225 (2000).

[35] T. Sonnleitner, D.A. Turton, S. Waselikowski, J. Hunger, A. Stoppa, M. Walther, K.

- Wynne, and R. Buchner, *J. Mol. Liq.* 192, 19-25 (2014).
- [36] P.-G. de Gennes, *Scaling Concepts in Polymer Physics*, Cornell University Press, Ithaca (1979).
- [37] O. Glatter and O. Kratky, *Small Angle X-Ray Scattering*, Academic, London (1982).
- [38] K. Nishi, T. Hiroi, K. Hashimoto, K. Fujii, Y.-S. Han, T.-H. Kim, Y. Katsumoto, and M. Shibayama, *Macromolecules* 46, 6225-6232 (2013).
- [39] G.K. Wertheim, M.A. Butler, K.W. West, and D.N.E. Buchanan, *Rev. Sci. Instrum.* 45, 1369-1371 (1974).
- [40] G.R. Strobl, *The Physics of Polymers: Concepts for Understanding Their Structures and Behavior*, Springer, Berlin, Heidelberg (2007).
- [41] T. Fukasawa, T. Sato, J. Watanabe, Y. Hama, W. Kunz, and R. Buchner, *Phys. Rev. Lett.* 95, 197802 (2005).
- [42] E.A.S. Cavell, P.C. Knight, and M.A. Sheikh, *Trans. Faraday Soc.* 67, 2225-2233 (1971).
- [43] R. Buchner, C. Hölzl, J. Stauber, and J. Barthel, *Phys. Chem. Chem. Phys.* 4, 2169-2179 (2002).
- [44] A. Eiberweiser, A. Nazet, G. Hefter, and R. Buchner, *J. Phys. Chem. B* 119, 5270-15211 (2015).
- [45] R. Buchner, S.G. Capewell, G. Hefter, and P.M. May, *J. Phys. Chem. B* 103, 1185-1192 (1999).
- [46] V. Agieienko, D. Horinek, and R. Buchner, *Phys. Chem. Chem. Phys.* 19, 219-230 (2017).
- [47] M. Shibayama, M. Morimoto, and S. Nomura, *Macromolecules* 27, 5060-5066 (1994).

- [48] M. Chalal, F. Ehrburger-Dolle, I. Morfin, F. Bley, M.-R. Aguilar de Armas, M.-L. López Donaire, J. San Roman, N. Bölgen, E. Pişkin, O. Ziane, and R. Casalegno, *Macromolecules* 43, 2009-2017 (2010).
- [49] P. Perez, F. Plieva, A. Gallardo, J. San Roman, M. R. Aguilar, I. Morfin, F. Ehrburger-Dolle, F. Bley, S. Mikhalovsky, I.Y. Galaev, and B. Mattiasson, *Biomacromolecules* 9, 66-74 (2008).
- [50] T. Kureha, T. Sato, and D. Suzuki, *Langmuir* 30, 8717-8725 (2014).

Chapter 4.

Ion fluctuations and intermembrane interactions in aqueous dispersions of dialkylchain cationic surfactant

A dialkylchain cationic surfactant forms the so-called α -gel in water showing virtually no fluidity, which is transformed into a highly fluidic dispersion upon addition of a small amount of salt. This intriguing phenomenon is utilized in household industries. However, the underlying mechanisms remain unclear. Here, we use dielectric relaxation spectroscopy (DRS) and simultaneous small- and wide-angle x-ray scattering (SWAXS) to shed light on this issue. We find that an excess amount of CaCl_2 induces an α -gel-to-multi-lamellar vesicle (MLV) transition accompanied by a marked increase of the reservoir volume fraction. This resembles an unbound lamellar-to-bound lamellar transition but cannot be explained without invoking a weak long-ranged electrostatic attraction. The DRS data provide evidence that the counterions fluctuate both vertically and laterally at the interface, whose relaxation amplitudes sharply depend on a percolating state of an aqueous phase. The strikingly small bulk-water amplitude is likely to reflect depolarizing electric fields induced by the MLV architecture, along with genuine hydration effects. The modified Caillé approach to the SAXS intensities reveals sensitive salt-concentration dependent membrane–membrane interactions. The least undulating membranes are formed at a salt concentration of ca. 10 mmol L^{-1} . Above 25 mmol L^{-1} , where small surface separation ($< 2.5 \text{ nm}$) is attained, far more undulating membranes than those predicted by the Helfrich interaction are produced. This suggests that the hydration forces, generally believed to induce strong short-range repulsion, do not

suppress the membrane undulation fluctuations.

4.1. Introduction

Understanding interactions between membranes is central to comprehending a wide range of physical, chemical and biological phenomena. It has long been believed that as classical Derjaguin–Landau–Verwey–Overbeek (DLVO) theory predicted, fundamental interactions between membranes are to a large extent determined by a balance between attractive van der Waals and repulsive electric double-layer forces [1–4]. It has been recognized that non-DLVO forces also play a significant role [3–14]. The Helfrich undulation interaction, arising from the steric hindrance of the out-of-plane fluctuations of flexible membranes, leads to a long range repulsive force [7]. For a double-chain surfactant, the bending modulus $k_C \approx k_B T$ seems to be a necessary condition for spontaneous vesicles to be equilibrium structures, where k_B is the Boltzmann constant and T is the temperature, because the induced Helfrich-type repulsion between bilayers can dominate the van der Waals attraction [15]. Water layers and hydrated ions adjacent to the interface induce a strong repulsive potential at a small separation of less than ~ 20 Å, whose decay is empirically described by an exponential function having a characteristic length of about 5 Å [3,4,6,13]. This notable short range repulsive force is called the hydration force, which efficiently prevents direct contact of the membranes embedded in water. Batista et al.[14] indicated that a clear decomposition of the interaction potential into individual contributions often becomes difficult due to the coupled structural dynamics of neighboring colloidal particles and surrounding media.

An alternative description of the fundamental forces to that of the classical DLVO theory was given by Langmuir in 1938 [5], which involved a long-range electrostatic attraction.

Although this idea was not widely accepted for a long time, it was restored by Sogami in his electrostatic interaction theory in 1983 [8]. Sogami and Ise [9] argued that order formation observed in a dispersion of highly charged macroions is unable to be explained without invoking a weak long-range electrostatic attraction mediated by the intermediate counterions. Lukatsky and Safran [12] also pointed out that counterion fluctuations induce attraction between interfaces. Using dielectric relaxation spectroscopy (DRS), Buchner and co-workers unambiguously showed that multidimensional fluctuations of the counterions occur in aqueous micellar solutions of ionic surfactants, such as sodium dodecyl sulfate (SDS) [16] and alkyltrimethylammonium salts [17,18]. These micelle-specific ion fluctuations can be detected as two well-defined relaxation modes having nanosecond timescales.

Interactions between bilayer membranes in a variety of systems have been studied by using a direct force measurement technique [3,4,13,19,20] originally developed by Israelachvili [3,4]. This technique allowed a variety of interactions between surfaces in liquids to be revealed depending on the nature of the surfaces as well as mediating liquids at sub nanometer resolution. Quantitative information about the interactions occurring in a stack of bilayer membranes is accessible by means of small angle scattering of x-rays or neutrons [15,21–28]. In the pioneering studies of Safinya and Roux [21,22], they demonstrated that interactions between negatively charged membranes composed of SDS and pentanol monitored along two dilution paths with water and brine are almost solely dominated by electrostatic and undulation forces, respectively.

Dialkyl dimethyl ammonium salts are an important class of cationic surfactants. Since the discovery of a totally synthetic bilayer membrane composed of didodecyl dimethyl ammonium bromide by Kunitake et al. [29], pseudo-spontaneous vesicle formation in

ionic [30–32] and nonionic [33] systems has been extensively discussed [19,26,28–30,32,34]. In household industries, an inorganic salt such as CaCl_2 is used as a viscosity modifier of aqueous double-chain cationic surfactant-based materials in the production of a wide range of home and personal products. Dihardened tallow dimethyl ammonium chloride (DTDAC; 2HT) forms the so-called α -gel in water, i.e., a lamellar gel having partially frozen hydrocarbon chains showing virtually no fluidity (Figure 4.1). Upon addition of a small amount of salt, a stiff α -gel is transformed into a highly fluidic milky dispersion. To clarify the underlying mechanisms of this intriguing phenomenon, we investigate the effects of CaCl_2 concentration on the interactions between the bilayer membranes formed by 2HT. We evaluate the extent of the bilayer undulation fluctuation disorder by means of simultaneous small- and wide-angle x-ray scattering (SWAXS). To monitor counterion fluctuations and the cooperative dynamics of solvent water, we use dielectric relaxation spectroscopy (DRS) [16–18,35–41].

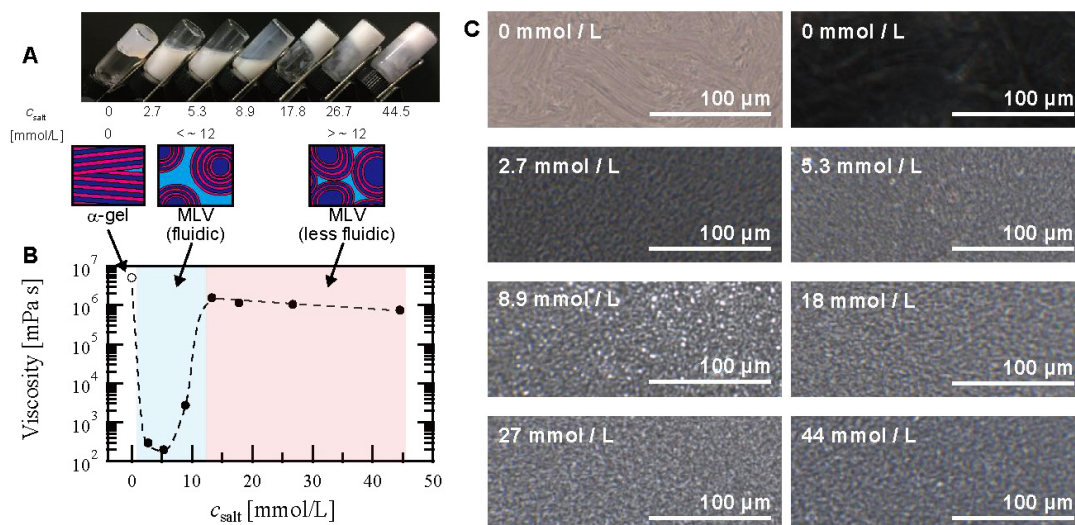


Figure 4.1. Effects of CaCl_2 concentration, c_{salt} , on the fluidity of 10 wt% 2HT dispersions: (A) a visual inspection, (B) low shear rate viscosities at a shear rate of 0.01 s^{-1} , and (C) representative images using phase-contrast microscopy (scale bar = $100 \mu\text{m}$). For the sake of clarity, a bright-field micrograph of a 2HT dispersion without CaCl_2 salt, whose observation condition is identical to that of the image at the right top corner, is also displayed. The open and filled symbols in (B) represent the data for the α -gel and MLVs, respectively. Most plausible structures are schematically depicted in the upper part of panel (B). Light blue and red areas highlight the salt concentration regions, in which the dispersions exhibit high and low fluidity, respectively.

4.2. Experimental Methods

4.2.1. Materials

Dialkyl chain cationic surfactant, dihardened tallow dimethylammonium chloride (2HT), was supplied by Research & Development Headquarters, LION Corporation, Japan, and calcium chloride (CaCl_2) was purchased from Wako Pure Chemical Industries Ltd, Japan. These materials were used as received. Gas chromatography analysis indicated

$C_{16}H_{33}C_{16}H_{33}N(CH_3)_2Cl : C_{16}H_{33}C_{18}H_{37}N(CH_3)_2Cl : C_{18}H_{37}C_{18}H_{37}N(CH_3)_2Cl = 16 : 42 : 42$, according to which the average molecular mass was evaluated to be 565 g mol^{-1} . The melted 2HT surfactant was thoroughly mixed with hot water at $60 \text{ }^\circ\text{C}$ under reduced pressure. Aqueous CaCl_2 solution was added to the 2HT/water mixtures to adjust the salt concentration and the samples were gently stirred for 30 minutes whilst being kept at $60 \text{ }^\circ\text{C}$. The formulated dispersions were equilibrated at $25 \text{ }^\circ\text{C}$ for several days. The surfactant concentration was fixed to 10 wt% and the CaCl_2 concentration, c_{salt} , was varied in the range of $0 \leq c_{\text{salt}}/\text{mmol L}^{-1} \leq 44.5$.

4.2.2. Dielectric relaxation spectroscopy (DRS)

Dielectric relaxation spectroscopy monitors the response of dipolar liquids to an applied time-dependent electric field of frequency, ν . For a solution exhibiting non-negligible dc conductivity, κ , the response is described in terms of the total complex permittivity, $\eta^*(\nu) = \varepsilon^*(\nu) - i\kappa/2\pi\nu\varepsilon_0$, where $\varepsilon^*(\nu)$ is the complex permittivity and ε_0 is the permittivity of a vacuum. An additional second term denotes an Ohmic loss contribution caused by charge transport. We determined the complex dielectric spectra, $\varepsilon^*(\nu) = \varepsilon'(\nu) - i\varepsilon''(\nu)$, of the aqueous dispersions of 2HT at $25 \text{ }^\circ\text{C}$ in $0.5 \text{ MHz} \leq \nu \leq 20 \text{ GHz}$ by measuring the total complex permittivity, $\eta^*(\nu)$, where $\varepsilon'(\nu)$ and $\varepsilon''(\nu)$ are the relative dielectric permittivity and the dielectric loss, respectively. We employed time domain reflectometry (TDR) comprising the Hewlett–Packard instruments HP54121A and HP54120B. All time-domain measurements and the transformation of the time-dependent reflected pulse waveforms to the frequency domain spectra were performed according to previously reported procedure [38]. The conductivity of the samples can be evaluated from the reflected waveform measurements in the TDR experiment.

To give a quantitative description of the experimental $\varepsilon^*(\nu)$ spectra, a series of conceivable relaxation models based on a superposition of n Havriliak–Negami equations [42]

$$\varepsilon^*(\nu) = \varepsilon_\infty + \sum_{j=1}^n \frac{\Delta\varepsilon_j}{[1 + (i2\pi\nu\tau_j)^{\beta_j}]^{\alpha_j}} \quad (4.1)$$

or its counterparts, such as Debye, Cole–Cole, and Davidson–Cole equations, were tested using a non-linear least-squares fitting procedure. A j th dispersion step ($j = 1, 2 \dots$ and n) is defined according to the magnitude of its relaxation time, τ_j ($\tau_j > \tau_{j+1}$). n is the number of dispersion steps, ε_∞ is the infinite frequency permittivity and α_j and β_j are the shape parameters representing asymmetric [43] and symmetric [44] broadening of the spectrum shape, respectively.

4.2.3. Small- and wide-angle x-ray scattering (SWAXS)

Simultaneous small- and wide-angle x-ray scattering (SWAXS) experiments were carried out using a SAXSess camera (Anton Paar, Graz, Austria) in the extended q -range between 0.06 and 27 nm^{-1} , where q is the magnitude of the scattering vector. The apparatus was equipped with an x-ray generator with a long fine focus sealed glass x-ray tube (GE Inspection Technologies, Germany), a focusing multilayer optics, and a block collimator. The system provided a line-shaped monochromatic primary beam (Cu $K\alpha$ radiation, a wavelength $\lambda = 0.154$ nm). The generator was operated at 40 kV and 50 mA. The scattering intensity was recorded using an imaging-plate detector having a pixel size of 45 $\mu\text{m} \times 45 \mu\text{m}$ and the sample to detector distance was 265 mm, corresponding to $\Delta q \approx 0.007$ nm^{-1} . The two dimensional scattered intensities were integrated into a one dimensional scattering curve. We used a vacuum-tight quartz capillary cell with a 1 mm

diameter that can be repeatedly used. The background contributions from a capillary cell and the solvent were subtracted. The absolute intensity calibration was made using water as a secondary standard [45]. A model independent collimation correction procedure (desmearing) was applied relying on the Lake algorithm [46] to obtain the scattering curves equivalent to those measured by an ideal point focus system.

To confirm the isotropic scattering patterns of the 2HT dispersion, SAXS experiments were performed using a pinhole camera, a SmartLab instrument (Rigaku, Japan). This instrument provides a point collimated primary beam of Cu K α radiation. The diameters of the first and second pinholes are 50 and 80 μm , respectively. The covered q -range is between 0.16 and 1.21 nm^{-1} .

4.2.4. Density measurements

Using a high precision densimeter, DMA4500M (Anton Paar, Austria), which is based on a conventional mechanical oscillator method, density measurements were carried out on aqueous dispersions of 2HT at 25 $^{\circ}\text{C}$ at different salt concentrations. The density data were used for calculating the molar concentration of the 2HT surfactant, $c_{2\text{HT}}$ [mol L^{-1}], as well as the analytical water concentration, $c_w(c)$ [mol L^{-1}], from the surfactant weight fraction, $w_{2\text{HT}}$.

4.2.5. Viscosity curve measurements

Shear viscosities of the 2HT dispersions at different salt concentrations were measured on an MCR92 rheometer (Anton Paar) equipped with a cone-plate measuring device in the shear rate range of 0.01–1000 s^{-1} at 25 $^{\circ}\text{C}$. Viscosity curves are shown in Figure 4.2.

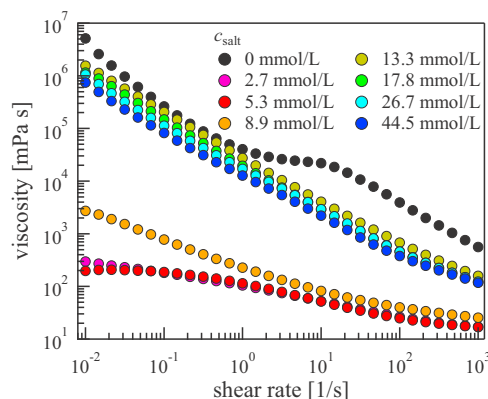


Figure 4.2. Viscosities of 2HT dispersions at different CaCl_2 concentrations at $25\text{ }^\circ\text{C}$ as a function of the share rate.

4.2.6. Optical microscopy observation

Microscopy observations were performed using an inverted microscope Eclipse Ts2 (Nikon, Japan). A drop of the 2HT dispersion was placed onto a 1 mm thick microscope slide, and the specimen was covered by a thin cover glass to avoid solvent evaporation.

4.3. Results and Discussion

4.3.1. Dielectric properties of the aqueous dispersions of 2HT

In Figure 4.3, we show the complex dielectric spectra, $\varepsilon^*(\nu)$, of the aqueous dispersions of 2HT at $25\text{ }^\circ\text{C}$ as a function of CaCl_2 concentration, c_{salt} . Upon addition of 2HT to water, broad low frequency dispersions emerge. At high salt concentrations ($c_{\text{salt}} > \sim 10\text{ mmol L}^{-1}$), these contributions become more pronounced and far exceed the solvent contribution in terms of their amplitudes. The high frequency process centered at $\sim 19\text{ GHz}$ always appears without a notable shift in the loss peak frequency of pure water. By fitting the experimental $\varepsilon^*(\nu)$ spectra to equation (4.1), we find that a superposition of four

Debye relaxation functions gives the best and most consistent description of the dielectric response of the 2HT dispersions, which is conveniently written as

$$\varepsilon^*(\nu) = \varepsilon_\infty + \frac{\Delta\varepsilon_{\text{MW}}}{1 + i2\pi\nu\tau_{\text{MW}}} + \frac{\Delta\varepsilon_1}{1 + i2\pi\nu\tau_1} + \frac{\Delta\varepsilon_2}{1 + i2\pi\nu\tau_2} + \frac{\Delta\varepsilon_3}{1 + i2\pi\nu\tau_3} \quad (4.2)$$

The results of the fitting procedure are shown in Figure 4.3B–E. The lowest-frequency process centered at about 3 MHz is assigned to the so-called Maxwell–Wagner (MW) relaxation arising from interfacial polarization effects. This emerges when the transportation of ions is blocked by the interface, which cannot be seen for aqueous solutions of ionic surfactants, such as SDS [16] or alkyl trimethyl ammonium bromide (TAB) or chloride (TAC) [17]. Apart from the MW relaxation, we observe two additional solute relaxation processes ($j = 1$ and 2) in the MHz frequency region, whose relaxation times are rather similar to those observed in a variety of ionic micellar solutions [16–18]. They can be assigned to counterion fluctuations despite the fairly different surfactant self-assembly structures. By comparing the spectrum of pure water [40], the high-frequency process ($j = 3$) is clearly attributed to the cooperative relaxation of bulk water. In Figure 4.4, the relaxation times, τ_j , and amplitudes, $\Delta\varepsilon_j$, are presented.

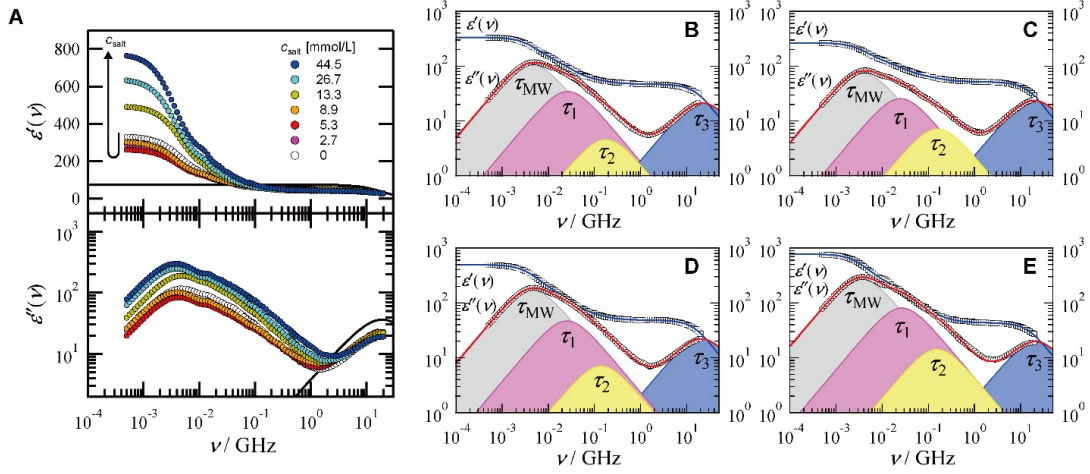


Figure 4.3. Spectra of (A) dielectric dispersion, $\varepsilon'(\nu)$, and dielectric loss, $\varepsilon''(\nu)$, of 10 wt% 2HT dispersions at 25 °C in a CaCl_2 concentration range between 0 and 44.5 mmol L^{-1} . Solid lines represent the pure water spectrum [40] for comparison. The $\varepsilon^*(\nu)$ spectra at CaCl_2 molar concentrations of (B) 0 mmol L^{-1} , (C) 5.3 mmol L^{-1} , (D) 13.3 mmol L^{-1} , and (E) 44.5 mmol L^{-1} .

4.3.2. Solute relaxation and ion fluctuations

We analyzed the salt concentration dependence of the spectra. Two solute-modes for ionic surfactant solutions are generally well described by the Grosse model for a dispersion of charged spherical colloidal particles [16–18,47]. The Grosse model predicts that the relaxation times, τ_j , and amplitudes, $\Delta\varepsilon_j$, of the ioncloud relaxation ($j = 1$) and of the surface-hopping mode of the adsorbed but still mobile counterions ($j = 2$) are defined by the following four equations [17,47],

$$\tau_1 \approx \frac{R_G^2}{D} \quad (4.3)$$

$$\Delta\varepsilon_1 = \frac{9\phi\varepsilon_m \left(\frac{2\chi\lambda_s}{\kappa}\right)^4}{16 \left[\frac{2\chi\lambda_s}{\kappa} \left(\frac{2\lambda_s}{R_G\kappa} + 1\right) + 2\right]^2} \quad (4.4)$$

$$\tau_2 = \frac{\varepsilon_0 \varepsilon_m \left(\frac{\varepsilon_p}{\varepsilon_m} + 2 \right)}{\kappa \left(\frac{2\lambda_s}{R_G \kappa} + 2 \right)} \quad (4.5)$$

$$\Delta\varepsilon_2 = \frac{9\phi \varepsilon_m \left(\frac{2\lambda_s}{R_G \kappa} - \frac{\varepsilon_p}{\varepsilon_m} \right)^2}{\left[\left(\frac{\varepsilon_p}{\varepsilon_m} + 2 \right) \left(\frac{2\lambda_s}{R_G \kappa} + 2 \right) \right]^2} \quad (4.6)$$

where D is the diffusion coefficient of free counterions, R_G is the Grosse radius describing the location of the adsorbed counterions from the center of mass of the particles, ϕ is the volume fraction of the particles, ε_p and ε_m are the static permittivities of the particle's core and the medium, respectively, χ^{-1} is the Debye length, κ is the dc conductivity of the dispersion, and λ_s is the surface conductivity. Strictly speaking, the Grosse model can be validly applied to spherical particle systems in the limit of $R_G \gg \chi^{-1}$. Nevertheless, we apply it to the present MLV systems in an extended manner. Note that, obviously, the 2HT bilayer membrane is not a homogeneous spherical particle, but its small curvature gives a better situation for applying the Grosse model to the charged bilayers than to charged spherical-like micelles. Using equations (4.3)–(4.6), R_G , λ_s , $\Delta\varepsilon_2$, and χ^{-1} can be evaluated using the experimentally determined parameters of τ_1 , $\Delta\varepsilon_1$, τ_2 , $\Delta\varepsilon_1$, and κ (Figure 4.4 and 4.6B). We fix ϕ to 0.11 and assume the values of $\varepsilon_p = 2$ and $\varepsilon_m = 78.4$, whereas D of Cl^- ($2.03 \times 10^{-9} \text{ m}^2 \text{ s}^{-1}$) is taken from the literature [48].

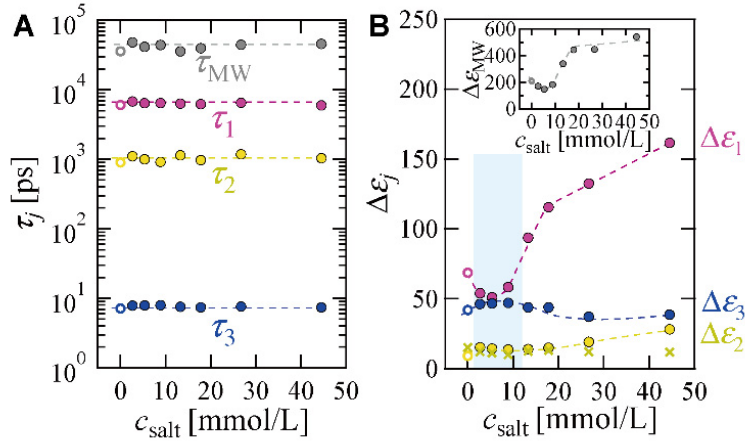


Figure 4.4. (A) Dielectric relaxation times, τ_j , and (B) amplitudes, $\Delta\epsilon_j$, of the aqueous dispersions of 2HT at 25 °C (a Maxwell–Wagner (MW) relaxation and $j = 1, 2$ and 3) as a function of added salt (CaCl_2) concentration. The open and filled symbols represent the data for the α -gel and MLVs, respectively. The blue area highlights the highly fluidic region. Cross marks indicate the predicted $\Delta\epsilon_2$ (equation (4.6)) values from λ_s determined from the experimental τ_2 values.

The R_G value can solely be determined from τ_1 (equation (4.3)), assuming that the constant diffusion coefficient $D = 2.03 \times 10^{-9} \text{ m}^2 \text{ s}^{-1}$. From $\tau_1 \approx 6.4 \text{ ns}$, $R_G \approx 3.6 \text{ nm}$ is obtained, which is virtually independent of c_{salt} . Since the salt-added 2HT dispersions show the formation of sub-micron to micron-sized spherical-like particles, it is obvious that $R_G \approx 3.6 \text{ nm}$ cannot be correlated with the radii of the MLVs. Instead, the value is nicely coupled to the thickness of the 2HT bilayer, δ (ca. 4.8–5 nm) (see Figure 4.12B and C). Indeed, $R_G \approx 3.6 \text{ nm}$ is comparable to the distance of $\delta/2 + 4r(\text{H}_2\text{O}) + r(\text{Cl}^-) \approx 3.3 \text{ nm}$ estimated by accounting for the hydration layers of the interface and chloride ion, where $r(\text{H}_2\text{O})$ and $r(\text{Cl}^-)$ are the radii of a water molecule and chloride ion, respectively. Therefore, the value of R_G can be practically interpreted as the location of the center of the condensed counterions relative to the center of the 2HT membrane around which the counterions fluctuate.

As for ionic spherical-like micelles, such as SDS [16] and C_8TAB , C_{12}TAB , C_{16}TAB

and C₁₂TAC [17] micelles, the amplitude of the surface-hopping (the lateral mode), $\Delta\epsilon_2$, is always dominant over that of the ion-cloud fluctuation (the vertical mode), $\Delta\epsilon_1$. However, we find that in the 2HT dispersions, the amplitudes of the lateral and vertical modes are inverted ($\Delta\epsilon_1 > \Delta\epsilon_2$). Furthermore, $\Delta\epsilon_1$ shows approximately one order of magnitude greater values than that observed for ionic micellar solutions [16,17]. These phenomena can be understood based on simple simulation using equations (4.4) and (4.6). Although the Grosse model does not explicitly involve ion concentration or ionic strength, the effect is implicitly expressed in the Debye length, χ^{-1} , and the relative surface conductivity against the bulk conductivity, λ_S/κ . The simulated $\Delta\epsilon_1$ and $\Delta\epsilon_2$ as a function of λ_S/κ are shown in Figure 4.5, in which the Debye length χ^{-1} is fixed as 2, 2.5, and 3 nm for simplicity although in a strict sense, χ^{-1} and κ are not independent. At higher c_{salt} , the shorter χ^{-1} leads to greater values of $\Delta\epsilon_1$. $\Delta\epsilon_1$ shows an upturn increase with λ_S/κ , while $\Delta\epsilon_2$ exhibits a relatively moderate upward-convex increase. Thereby, a high λ_S/κ value, i.e., a high surface conductivity λ_S relative to the bulk conductivity κ , results not only in greater relaxation amplitudes of the ion fluctuations, but also in the inversion of $\Delta\epsilon_1$ and $\Delta\epsilon_2$, yielding a greater value of $\Delta\epsilon_1$ than $\Delta\epsilon_2$.

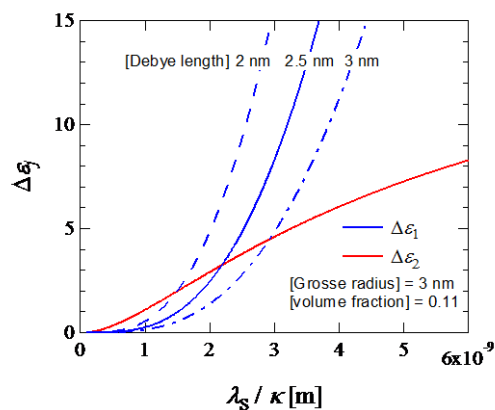


Figure 4.5. Simulated relaxation amplitudes of the ion-cloud fluctuation, $\Delta\epsilon_1$ (equation (4.4)), and the surface-hopping mode, $\Delta\epsilon_2$ (equation (4.6)), as a function of the relative surface conductivity against the bulk conductivity, λ_s/κ . The Grosse radius and the volume fraction are fixed to 3 nm and 0.11, respectively. The simulated $\Delta\epsilon_1$ with the Debye length of 2 nm, 2.5 nm, and 3 nm are represented by the blue dashed, solid, and dash-dot lines, respectively.

It is known that membranes and vesicle architectures serve as an insulator of electric conduction. The conductivity in the vesicle dispersions can be approximated to be in inverse proportion to the diameter of the MLVs [26,49]. Indeed, the measured conductivities of the 2HT dispersions are one order of magnitude smaller than those of the C₁₂TAC solutions with no added salt [17]. Furthermore, ions dissolved in an inner aqueous phase of the vesicles may not practically contribute to the conductivity of the dispersion.

Importantly, we observe that the amplitude of the diffused ion cloud ($\Delta\epsilon_1$) exhibits an eccentric behavior, a minimum at $c_{\text{salt}} \approx 5 \text{ mmol L}^{-1}$ and a most abrupt increase in the range of $10 < c_{\text{salt}}/\text{mmol L}^{-1} < 20$. In Figure 4.6D, we present the evaluated λ_s/κ from τ_2 applying equation (4.5) using the measured κ and the readily determined R_G . In Figure 4.4B, the predicted $\Delta\epsilon_2$ values from λ_s determined from the experimental τ_2 values are shown. Despite a successive increase of the ion concentration, λ_s/κ shows a minimum at

$c_{\text{salt}} \approx 10 \text{ mmol L}^{-1}$. This causes the characteristic behavior of $\Delta\varepsilon_1$ shown in Figure 4.4B. As shown in Figure 4.1, the viscosity of the 2HT dispersions drastically decreases upon addition of a small amount of salt ($c_{\text{salt}} < 3 \text{ mmol L}^{-1}$), but with a further increase of the salt concentration ($c_{\text{salt}} > 10 \text{ mmol L}^{-1}$), it rapidly increases. Therefore, the minimum of λ_S/κ and the resulting marked change of $\Delta\varepsilon_1$ in the range of $10 < c_{\text{salt}}/\text{mmol L}^{-1} < 20$ can be attributed to the α -gel-to-vesicle transition accompanied by a drastic increase of the reservoir volume fraction due to expelled solvent water. A sharp minimum of λ_S/κ mainly reflects a macroscopically permeable state of an aqueous phase.

As shown in Figure 4.6C, the χ^{-1} values resulting from the DRS analysis based on the Grosse model show a similar decreasing trend to those obtained by conventional calculations. Although the discrepancy between them is far less than one order of magnitude, this may be caused by non-ideal application conditions of the Grosse theory to the MLVs or α -gel. A simple assumption for the degree of counterion dissociation ≈ 0.1 for the conventional calculation may also be an error source.

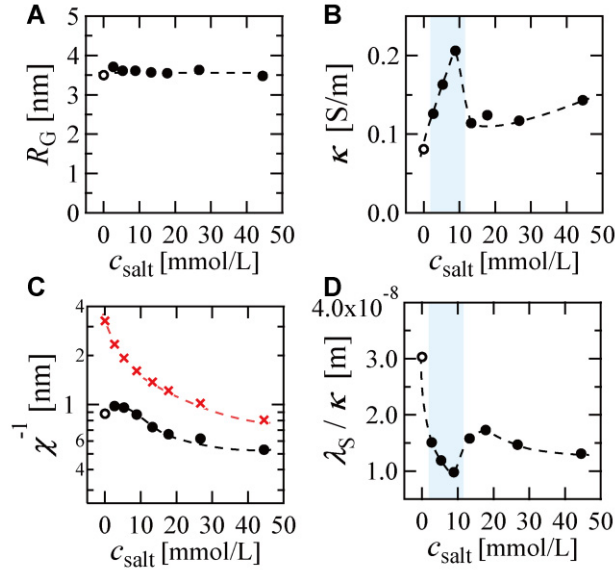


Figure 4.6. (A) The Grosse radius, R_G , (B) the bulk conductivity, κ , (C) the Debye length, χ^{-1} , and (D) the relative surface conductivity against the bulk conductivity, λ_S/κ , as a function of added salt (CaCl_2) concentration. The open and filled symbols represent the data for the α -gel and MLVs, respectively. The blue area highlights the highly fluidic region. Cross symbols in (C) represent the Debye length calculated in a conventional manner from $\chi^{-1} = [\epsilon_m \epsilon_0 k_B T / (2N_A e^2 I)]^{-1/2}$.

4.3.3. Hydration effects of 2HT

The dielectric spectrum of pure water in the microwave region is governed by a single Debye relaxation attributed to the collective reorientation of water molecules, which is associated with the cooperative rearrangement of the hydrogen-bond network of water [40]. In the 2HT dispersions, the amplitude of bulk water, $\Delta\epsilon_3$, is strikingly smaller than those predicted by a mixture model and the analytical (actual) water concentration, it is reduced to about 65% or less than that of pure water at $w_{2\text{HT}} = 0.1$. This seems to be in part due to the manifestation of the strong water binding capability of 2HT and may imply that an enormous number of water molecules are strongly bound by the surfactants and ions in a cooperative manner. However, such a marked reduction of the bulk water

amplitude is not observed for the nonionic and ionic micellar solutions,[16,18,36,41] but the situation is rather similar to those observed for aqueous dispersions of zwitterionic phospholipids in a pioneering work of Pottel et al. [35] Here, we attempt to quantify the hydration effects. Relying on the generalized Cavell equation [39,50], the relaxation amplitude of the j th relaxation process, $\Delta\varepsilon_j$, is connected to the concentration of the relaxation species, c_j , by

$$\Delta\varepsilon_i = \frac{\varepsilon}{3(\varepsilon + (1 - \varepsilon)A_i)} \frac{N_A}{k_B T \varepsilon_0} \frac{g_i \mu_{Gi}^2}{(1 - \alpha_i f_i)^2} c_i \quad (4.7)$$

where ε is the static permittivity, A_j is the shape parameter, N_A is Avogadro's number, k_B is the Boltzmann constant, ε_0 is the vacuum permittivity, μ_{Gj} is the gas-phase dipole moment, g_j is the dipole–dipole correlation factor, α_j is the polarizability and f_j is the field factor. By normalizing equation (4.7) to that of pure water (solute concentration $c = 0$), the apparent water concentration, $c_w(c)^{\text{app}}$, at solute molar concentration c is written as

$$c_w^{\text{app}}(c) = c_w(c) \frac{g_w(c)}{g_w(0)} = \frac{\varepsilon(0)(2\varepsilon(c) + 1)}{\varepsilon(c)(2\varepsilon(0) + 1)} \frac{(1 - \alpha_w f_w(c))^2}{(1 - \alpha_w f_w(0))^2} \frac{\Delta\varepsilon_w(c)}{\Delta\varepsilon_w(0)} c_w(0) \quad (4.8)$$

where $\Delta\varepsilon_w(0) = 72.5$ and $\Delta\varepsilon_w(c) = \Delta\varepsilon_3(c)$. Assuming a spherical water molecule ($A_j = 1/3$) having a radius $r = 0.1425$ nm and a polarizability $\alpha_w = 1.607 \times 10^{-40}$ C m² V⁻¹, the apparent concentration of bulk water, $c_w(c)^{\text{app}}$, can be calculated (Figure 4.7A). Generally, $c_w(c)^{\text{app}}$ is understood as the concentration of water molecules that are not affected by the presence of solute molecules and/or ions, and thus they still retain their dynamic properties identical to those of bulk-water. We further define the effective hydration number of a 2HT molecule, Z_{hyd} , involving counterion hydration effects as

$$Z_{\text{hyd}} = [c_w(c) - c_w^{\text{app}}(c)]/c \quad (4.9)$$

where c is the molar concentration of the surfactant ($=c_{2\text{HT}}$). From equation (4.9), Z_{hyd} gives the number of water molecules that cannot contribute to the bulk-water relaxation

process ($j = 3$) due to hydration effects.

In ionic surfactant solutions, a slow water mode often appears as a several-times-slower relaxation process compared to that of bulk-like water [16,18,36]. This is normally assigned to the water molecules exhibiting reduced but not rotationally immobilized dynamics. Importantly, we are not able to resolve any slow water relaxation in the 2HT dispersions in the entire c_{salt} range. Therefore, the evaluated Z_{hyd} based on equation (4.9) is to be interpreted as Z_{ib} , where Z_{ib} is the number of ‘irrotationally bound’ water molecules per surfactant. $c_{\text{w}}(c) - c_{\text{w}}(c)^{\text{app}}$ reaches 12 mol L^{-1} at $w_{2\text{HT}} = 0.1$ ($c_{2\text{HT}} \approx 0.17 \text{ mol L}^{-1}$) under low salt conditions, corresponding to $Z_{\text{ib}} \approx 70$. Furthermore, $Z_{\text{ib}} > 100$ is obtained under high salt conditions, where $c_{\text{salt}} > 25 \text{ mmol L}^{-1}$. There are more than a couple of factors that may conceivably explain the high Z_{ib} values; the 2HT bilayer membranes are covered with an extended hydrophobic surface, cations potentially have a higher impact on the rotational mobility of water molecules than anions do (the hydration number of Ca^{2+} was estimated to be ca. 10 at room temperature by means of extensive measurements of the colligative properties of aqueous calcium salts [51], whereas $Z_{\text{ib}} = 0$ was evaluated for Cl^- by DRS [37]), and water molecules can be cooperatively bound by an anion and a cation, resulting in a frozen state in their rotational dynamics.

However, we obtain $Z_{\text{ib}} \approx 80$ at $c_{\text{salt}} = 18 \text{ mmol L}^{-1}$, which already exceeds the number of water molecules existing in a 3.4 nm-thick water layer between the surfaces. Strong compressions of water layers and/or an extremely long-range influence extended over more than several water layers from the surface that freezes the rotational mobilities of all water molecules has been suggested [52].

Equation (4.8) yields the relative Kirkwood’s dipole–dipole correlation factor in solution

against that in pure water, $g_w(c)/g_w(0)$, as expressed in its second term, which is a measure of the perturbation of the water dipole moments' parallel alignment (Figure 4.7B). The observed drastic reduction of the bulk water amplitude corresponds to a decrease of the Kirkwood's dipole–dipole correlation factor, decreasing to less than 70% of that in pure water. This finding is corroborated by the observation of Pottel et al. in their pioneering work on aqueous dispersions of zwitterionic phospholipids [35]. The drastic effects on the bulk water relaxation amplitude, $\Delta\epsilon_3$, manifested in the $g_w(c)/g_w(0)$ values are likely to reflect depolarizing electric fields induced by the MLV architectures, as recently predicted by Steinhauser and co-workers [53], which should be distinctly different from those in ionic micellar solutions and dispersions of homogeneous dielectric spheres. The simultaneous appearance of the maxima in c_w^{app} and $g_w(c)$ as well as the minimum in λ_S/κ in the high-fluidity region of $c_{\text{salt}} < 10 \text{ mmol L}^{-1}$ should be closely linked with a permeable state of an outer aqueous phase.

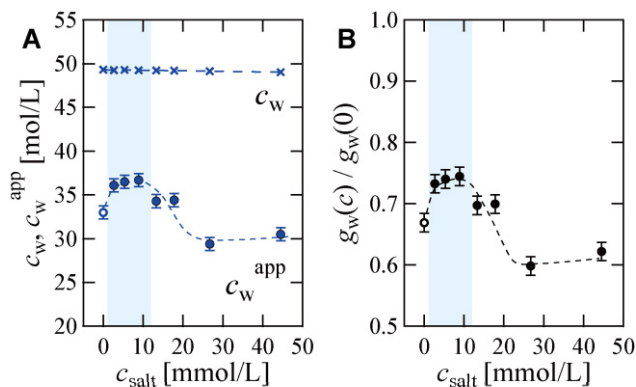


Figure 4.7. Effects of added CaCl₂ on the hydration of 2HT. (A) The apparent bulk water concentration, c_w^{app} , calculated from the bulk water relaxation amplitude and analytical water (molar) concentration, c_w , and (B) the Kirkwood's dipole–dipole correlation factor of water, $g_w(c)$, in the 2HT dispersions normalized by that in pure water, $g_w(0)$, as a function of CaCl₂ concentration, c_{salt} . The blue area highlights the region where the dispersion is highly fluidic.

4.3.4. Static structures of 2HT dispersions

It is established that liquid-like systems, e.g., α -gels, lamellar lyotropic liquid crystals [54], and MLVs [55,56], exhibit isotropic scattering patterns under static conditions. In Figure 4.8, we compare the scattering patterns obtained by a point and a line collimated apparatus, which confirm the isotropic scattering patterns of the 2HT dispersions and that the collimation corrected $I(q)$ measured by the line-collimation apparatus coincides well with that measured by the point collimated apparatus.

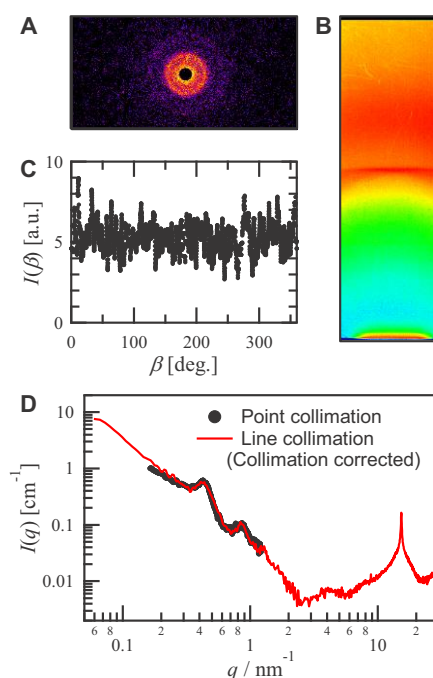


Figure 4.8. Two-dimensional scattering patterns of the 2HT dispersion at CaCl_2 concentration of 2.7 mmol/L as obtained by (A) a point collimation SmartLab apparatus and (B) a line collimation SAXSess mc² apparatus. One-dimensional scattering intensities as a function of (C) the magnitude of the azimuthal angle, β , and (D) the scattering vector, q , respectively. The azimuthal profile, $I(\beta)$, is obtained by integrating the point collimated $I(q)$ in the q -range between 0.36 and 0.48 nm⁻¹, corresponding to the scattering angles of 0.51° and 0.67°. For $I(q)$ data measured by the line collimation apparatus, a desmearing procedure is made. The background contribution and transmission calibration are corrected.

In Figure 4.9A, we show $I(q)$ for the 2HT dispersions on an absolute scale as a function of c_{salt} . The q^{-2} behavior as indicated by a dotted line is the so-called fractal scattering from the planar object, whose fractal dimension is two. The high- q oscillation seen in range of $2\text{--}6\text{ nm}^{-1}$ comes from the form factor of the planar object, mainly reflecting the thickness and internal electron-density distributions within the bilayers. The emergence of up to three reflections in the positional ratio of $1 : 2 : 3$ in the small angle regime reflects the long-range order of the membrane–membrane correlations. As shown in Figure 4.1, the microscope images of the 2HT dispersions confirm the formation of submicron to micron-sized spherical-like particles in the salt-added dispersions, whereas no particle-like objects are found in the sample with no added salt (α -gel). We also performed microscope observations on the 20-fold diluted dispersions and we were able to observe that spherical-like particles are still present (Figure 4.9).

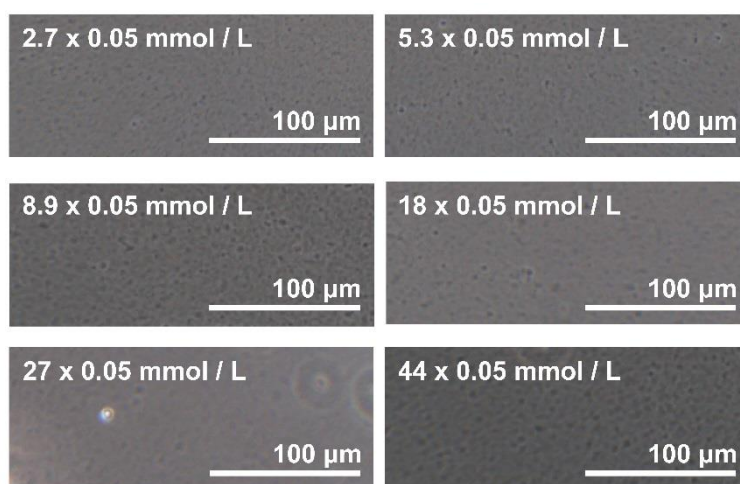


Figure 4.9. Phase-contrast micrographs of diluted 2HT dispersions (scale bar = $100\ \mu\text{m}$). These dispersions were prepared by diluting the mother dispersions of 2HT at different CaCl_2 salt concentrations by 20 times with Millipore water.

These data confirm the formation of a multi lamellar vesicle (MLV) structure, which can be classified as a lamellar gel (L_β) phase. In Figure 4.10B, the SAXS intensities in the

expression of $q^2I(q)$ are shown for a better visibility of the interference scattering. Importantly, even without imposing any structure factor model, it is already clear that at $c_{\text{salt}} \approx 10\text{--}20 \text{ mmol L}^{-1}$, the sharpness of the primary peak attains its maximum and the decay of the higher-order reflections becomes slowest.

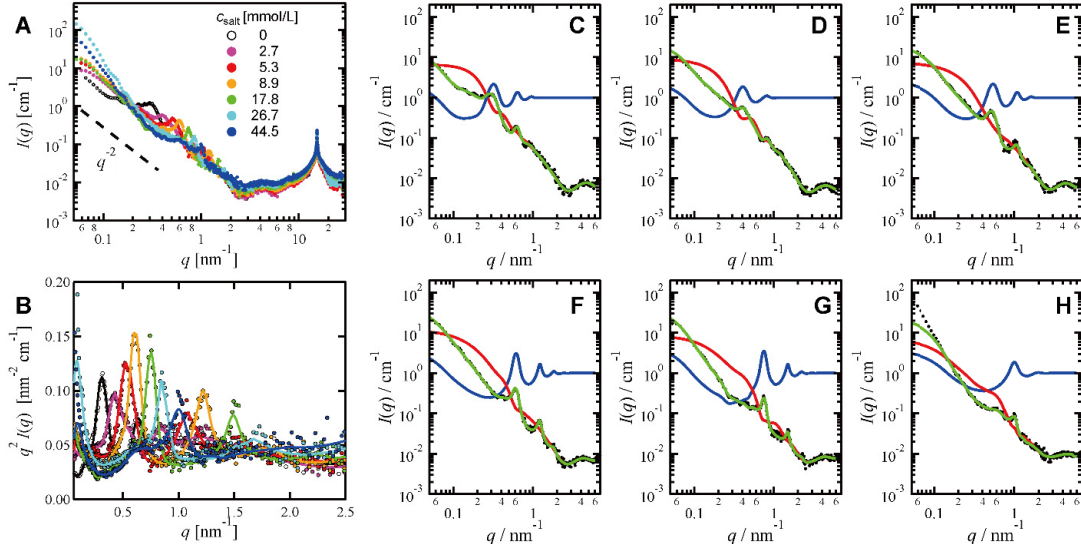


Figure 4.10. (A) Collimation-corrected SWAXS intensity, $I(q)$, of the aqueous dispersions of 0.174 mol L^{-1} 2HT at $25 \text{ }^\circ\text{C}$ on an absolute scale as a function of added CaCl_2 concentration from 0 to 44.5 mmol L^{-1} , and (B) a plot of $q^2I(q)$ in $0.06 \leq q/\text{nm}^{-1} \leq 2.5$, emphasizing the intermembrane interference contributions. GIFT analyses of $I(q)$ at CaCl_2 concentrations of (C) 0 mmol L^{-1} , (D) 2.7 mmol L^{-1} , (E) 5.3 mmol L^{-1} , (F) 8.9 mmol L^{-1} , (G) 17.8 mmol L^{-1} , and (H) 44.5 mmol L^{-1} . The green curve represents the GIFT fit to the experimental $I(q)$. The deduced form factor, $P(q)$, and structure factor, $S(q)$, are shown in red and blue curves, respectively.

To obtain further insights into the interactions between the bilayer membranes, we analyzed the SAXS data by applying the generalized indirect Fourier transformation (GIFT) technique [27,57] to the small-angle regime ($0.07 \leq q/\text{nm}^{-1} \leq 6$) of the experimental $I(q)$. Similarly to the case of globular particle systems, the scattering intensity $I(q)$ from a multilamellar stack of the bilayer membranes can be written as $I(q) \propto P(q)S(q)$, where $P(q)$ is the form factor and $S(q)$ is the structure factor [27]. The

structure factor $S(q)$ in the modified Caillé model [24,25,27] is given by

$$S(q) = N + \left\{ 2 \sum_{m=1}^{N-1} (N-m) \cos(mdq) \exp \left[- \left(\frac{d}{2\pi} \right)^2 q^2 \eta \gamma \right] \right. \\ \left. \times (\pi m)^{- \left(\frac{d}{2\pi} \right)^2 q^2 \eta} \right\} \quad (4.10)$$

where d is the interlayer spacing, N is the mean number of correlated bilayers, which scatter x-rays in a coherent manner, and γ ($= 0.5772$) is Euler's constant. The Caillé parameter, η , is interpreted as a measure for the undulation fluctuation disorder, which is given as a function of the bending modulus K of the bilayers and the compression modulus B [24,25,27,58]

$$\eta = \frac{q_1^2 k_B T}{8\pi \sqrt{KB}} \quad (4.11)$$

where $q_1 = 2\pi/d$ is the scattering vector corresponding to the primary peak position in $S(q)$. $k_C = Kd$ is the bending modulus of a single membrane. In our present approach, it is only possible to evaluate the product of these two moduli, KB or $k_C B$, from the SAXS data.

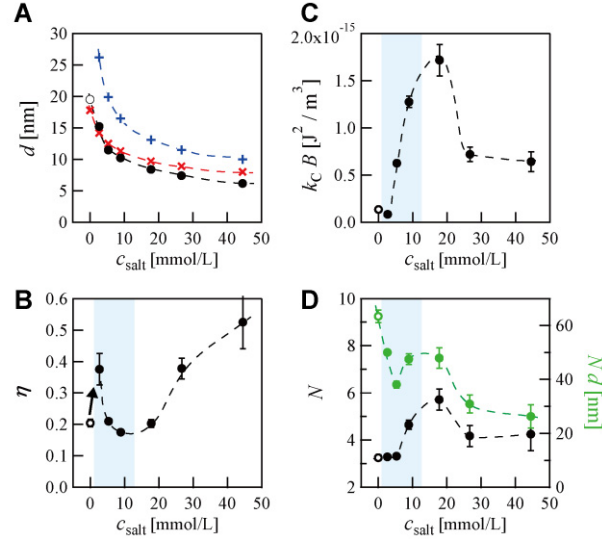


Figure 4.11. Structure factor parameters for the 2HT dispersions at $c_{2\text{HT}} = 0.174 \text{ mol L}^{-1}$. (A) Interlayer spacing, d , (B) Caillé parameter, η , (C) the product of the bending modulus of a single membrane and the compression modulus, $k_C B$, and (D) the number of correlated bilayers, N , and the extent of the long-range correlation, Nd , as a function of CaCl_2 concentration, c_{salt} . The predicted d -values from the Sogami–Ise potential, d_{SI} (red cross marks), and the modified DLVO potential, $d_{\text{mod-DLVO}}$ (blue positive signs), are also plotted in (A). An arrow in (B) highlights a marked increase of η induced by addition of a small amount of excess salt and the resulting α -gel-to-MLV transition. The blue area highlights the salt concentration region where the dispersion exhibits high fluidity.

Using the thickness scattering function $P_t(q)$, $P(q)$ is written as $P(q) = (2\pi A/q^2)P_t(q)$ [27,59], where $P_t(q)$ is given by the cosine transformation of the thickness distance distribution function, $p_t(r)$, as

$$P_t(q) = 2 \int_0^{\infty} p_t(r) \cos(qr) dr \quad (4.12)$$

The thickness of the bilayer, d , is estimated to be about 4.8–5.0 nm from the distance at which $p_t(r)$ goes to zero. The electron density profile, $\Delta\rho(r)$, is calculated by deconvoluting $p_t(r)$ (Figure 4.12B and C). The maximum distance read out from $\Delta\rho(r)$ (2.4–2.5 nm) is comparable to the length of a 2HT molecule (ca. 2.5 nm) [60]. The

negative values of $\Delta\rho(r)$ at $r < 1.5$ nm can clearly be attributed to the lower electron density of the hydrocarbon chains compared to that of solvent water. $\Delta\rho(r)$ appears to become nearly zero or only slightly positive at an intermediate distance of $r = 1.5\text{--}1.8$ nm and again shows negative values at larger r . We infer that this behavior reflects the average locations of the charged ammonium (N^+) group and terminal methyl groups of 2HT, respectively.

As already seen in the $q^2I(q)$ plot (Figure 4.10B), the shape of the structure factor $S(q)$ is strongly salt concentration dependent. Interlayer spacing, d , directly linked with the first-peak position, q_1 , in $S(q)$ as $d \approx 2\pi/q_1$, decreases with an increase of c_{salt} . As shown in Figure 4.10B and 4.12A, the α -gel-to MLV transition induced by adding a small amount of CaCl_2 causes a broader and weaker primary peak to appear in $S(q)$, but an increase of c_{salt} leads to a sharper and stronger peak. The sharpest primary peak and the slowest decay of higher-order reflections are observed at c_{salt} in the range of $10\text{--}20$ mmol L^{-1} , resulting in the minimum value of the Caillé parameter η , indicating the formation of the least undulating membranes. With a further increase of c_{salt} , the interference peaks get rapidly broader and weaker again. The number of correlated membranes, N , shows a maximum at $c_{\text{salt}} \approx 20$ mmol L^{-1} , leading to a local maximum of Nd .

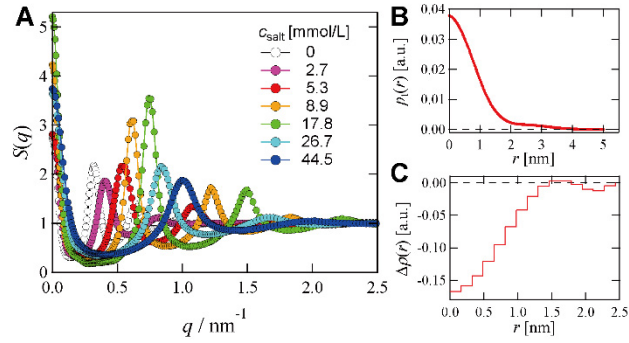


Figure 4.12. (A) Static structure factor, $S(q)$, of the 2HT membranes in the aqueous dispersion at $c_{2\text{HT}} = 0.174 \text{ mol L}^{-1}$ as a function of CaCl_2 concentration in the range of $0 \leq c_{\text{salt}}/\text{mmol L}^{-1} \leq 44.5$ deduced from the SAXS intensity, $I(q)$, shown in Figure 4.10C–G using the modified Caillé model. The thickness pair-distance distribution function, $p_t(r)$, and the electron density profile of the 2HT membranes are also displayed in (B) and (C), respectively.

4.3.5. Interaction potential calculations

The drastic reduction of the dispersion viscosity upon addition of salt indicates that the α -gel-to-MLV transition in the 2HT system is accompanied by a marked increase of the reservoir volume fraction due to expelled (excess) solvent water. In view of the c_{salt} -dependent behavior of the dispersion viscosity (Figure 4.1B) and the interlayer spacing d (Figure 4.11A), the present α -gel-to-MLV transition looks as if it is an unbound lamellar-to-bound lamellar transition although it is still uncertain if the α -gel can be classified as an unbound lamellar phase in a strict sense. The size of the innermost aqueous phase in a MLV may also largely change depending on c_{salt} . To model the interactions between the 2HT membranes, we calculate the interaction free energy for two flat surfaces per unit area using three different potential models based on Derjaguin-Landau-Verwey-Overbeek (DLVO) theory [1,2,4], the Sogami-Ise theory [8–10], and an extended DLVO theory [61].

The total potential, V_{DLVO} , between the surfaces can be described as the sum of two

contributions, the van der Waals attraction, V_A , and the electric double-layer repulsion, V_R as $V_{DLVO} = V_A + V_R$, where

$$V_A = -\frac{A}{12\pi} \left\{ \frac{1}{h^2} + \frac{1}{(h+2\delta)^2} - \frac{2}{(h+\delta)^2} \right\} \quad (4.13)$$

and

$$V_R = 64nk_B T \chi^{-1} \left[\tanh\left(\frac{e\psi_0}{4k_B T}\right) \right]^2 \exp(-\chi h) \quad (4.14)$$

A , h , δ , n , e , and ψ_0 respectively denote the Hamaker constant, surface separation, the bilayer thickness, number density of ions, charge of an electron, and surface potential obtained from the equation, $\sigma_0 = (8N_A I \epsilon_0 \epsilon_m k_B T)^{1/2} \sinh[e\psi_0/2k_B T]$, where σ_0 is the surface charge density and I is the ionic strength. The van der Waals potential between two flat surfaces, V_A , has a distance dependence of $V_A \sim h^{-2}$ as indicated by equation (4.13), thereby being inherently short-ranged and causing strong adhesion at a contact distance. The strength and the screening of the electrostatic double-layer potential are mainly determined by the surface charge density and the salinity of the intervening water, respectively. Higher salt concentration results in the faster decay of the potential. Monolayer compression isotherms of dialkyl dimethyl ammonium salt surfactants indicated the headgroup area of ca. 60 \AA^2 , whereas ca. 40 \AA^2 is obtained if all hydrocarbon chains are assumed to be crystalline and packed into a hexagonal lattice having a repeat distance of 4.2 \AA .

We also tested Sogami-Ise potential, V_{SI} , which assumes a weak long-range electrostatic attraction mediated by the intermediate counterions [8–10],

$$V_{SI} = \frac{\sigma_0^2}{\epsilon_m \epsilon_0} \frac{\exp(-\chi h)}{\chi} (3 - \chi h) \quad (4.15)$$

The depth of the potential minimum becomes shallower at higher salt concentration, where the surface separation is smaller.

Recently, Hishida and coworkers suggested the modified electric double layer interaction potential, V_{DL} , given by

$$V_{DL} = \frac{2\pi\varepsilon_m\varepsilon_0(k_B T)^2}{e^2} \left(\frac{1}{h} - \frac{1}{h_{\max}} \right) + \frac{2I - \rho_0}{Z} k_B T N_A (h - h_{\max}) \quad (4.16)$$

in which additional osmotic pressure arising from an ion concentration difference between inner and outer aqueous phases separated by vesicle architecture is taken into account [52]. The modified DLVO potential, $V_{\text{mod-DLVO}}$, is thus given by a sum of the van der Waals and the modified electric double layer potentials as $V_{\text{mod-DLVO}} = V_A + V_{DL}$. They claimed that this model can explain co-ion-valence effects on the lamellar repeat distance between anionic bilayers.

The interaction free energies, V_{DLVO} , V_{SI} , and $V_{\text{mod-DLVO}}$, are shown in Figure 4.13 and all parameters used in this calculation are listed in Tables 4.1, 4.2, and 4.3. The DLVO potential, V_{DLVO} , accounting for the attractive van der Waals and repulsive electric double-layer forces, is shown in Figure 4.13A. Milner and Roux discussed the transition between bound and unbound states of surfactant bilayers, which is controlled by the strength of attractive van der Waals interactions [11]. They demonstrated that when the attractive van der Waals interaction is strong enough (or the Hamaker constant, A , is large enough), the potential may have a minimum at a finite surface separation. A bound lamellar phase cannot be infinitely diluted, as it expels excess solvent when exceeding a certain maximal dilution. In contrast, in the unbound regime, d is simply governed by the surfactant concentration. With increasing A , a discontinuous phase transition from an unbound lamellar phase to a bound lamellar phase coexisting with excess solvent occurs. However, a distinct secondary minimum cannot be seen in the calculated DLVO potentials for the 2HT MLV bilayers at all investigated c_{salt} values, which is a typical feature of an unbound lamellar phase [11]. Therefore, the DLVO potential cannot explain the observed c_{salt} -

dependence of the d values for the 2HT dispersions.

Next, we recall the Sogami–Ise potential, V_{SI} , [8–10] which assumes a weak long-range electrostatic attraction mediated by intermediate counterions in addition to an intermediate range repulsion (Figure 4.13B). The predicted interlayer spacing from the Sogami–Ise potential, $d_{\text{SI}} = h_{\text{SI}} + d$, where h_{SI} is the surface separations corresponding to the minimum in V_{SI} and $d \approx 4.8$ nm is the thickness of the 2HT bilayer, eventually coincides with the experimentally obtained d values (Figure 4.11A). We note that as shown in Figure 4.13B, the depth of the potential minimum in V_{SI} becomes shallower at a higher salt concentration, which predicts a more disordered state of the membrane’s spatial distributions at a higher salt concentration. The observed destabilization of the longer-ranged ordering of the membranes, as manifested by a decrease of Nd , at a higher salt concentration is in fair agreement with the predictions of the Sogami–Ise model and can be at least qualitatively explained by Figure 4.13B. This finding may indicate that a weak long range attraction mediated by counterions is operative in the present systems although the issue is open to debate [62].

The modified DLVO potential, $V_{\text{mod-DLVO}}$, is defined by a sum of the van der Waals and the modified electric double layer potentials. According to this model, the potential minimum becomes markedly deeper at a higher-salt concentration, which would result in a highly ordered stacking state of the membranes at a higher salt concentration. However, we observe the smallest N and Nd values with unexpectedly large values of η at high salt concentrations, typically $c_{\text{salt}} > 25$ mM, which is an indication of the destabilization of the long-range order of the membranes at high c_{salt} . The predicted d values from the position of the potential minimum in $V_{\text{mod-DLVO}}$ systematically overestimate the observed d values, as shown in Figure 4.10A.

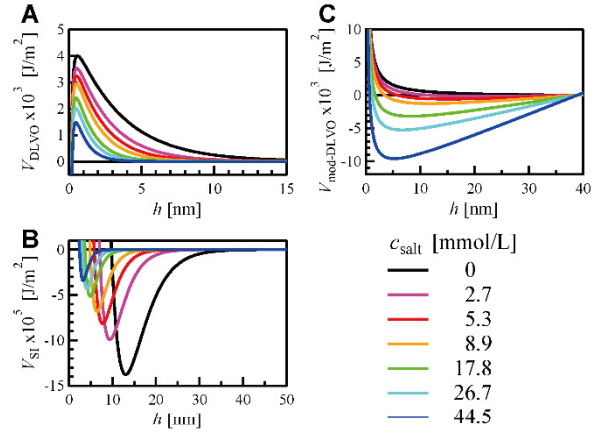


Figure 4.13. Interaction free energy for two charged flat surfaces per unit area in an aqueous electrolyte solution calculated based on (A) the Derjaguin-Landau-Verwey-Overbeek (DLVO) model, V_{DLVO} , (B) the Sogami-Ise model, V_{SI} , and (C) the modified DLVO model, $V_{\text{mod-DLVO}}$, as a function of surface separation of h .

Table 4.1. Parameters used for calculating DLVO interaction free energy, V_{DLVO} , for two charged flat surfaces shown in Figure 4.13A.

Parameter	Value
Boltzmann constant k_{B} [J / K]	1.38×10^{-23}
permittivity of vacuum ϵ_0 [C / V m]	8.85×10^{-12}
Avogadro number N_{A} [mol ⁻¹]	6.02×10^{23}
charge of an electron e [C]	1.60×10^{-19}
(relative) permittivity of solvent ϵ_{m}	78.36
Temperature T [K]	298.15
Hamaker constant A [J]	5×10^{-21}
surface charge density σ^* [C / m ²]	4.0×10^{-2}
layer thickness δ [nm]	4.8
degree of counterion dissociation	0.1

Table. 4.2. Parameters used for calculating effective potential of Sogami-Ise, V_{SI} , for two charged flat surfaces shown in Figure 4.13B.

Parameter	Value
Boltzmann constant k_B [J / K]	1.38×10^{-23}
permittivity of vacuum ϵ_0 [C / V m]	8.85×10^{-12}
Avogadro number N_A [mol ⁻¹]	6.02×10^{23}
charge of an electron e [C]	1.60×10^{-19}
(relative) permittivity of solvent ϵ_m	78.36
Temperature T [K]	298.15
surface charge density σ_0 [C / m ²]	4.0×10^{-2}

Table. 4.3. Parameters used for calculating modified DLVO interaction free energy, $V_{mod-DLVO}$, shown in Figure 4.13C.

Parameter	Value
Boltzmann constant k_B [J / K]	1.38×10^{-23}
permittivity of vacuum ϵ_0 [C / V m]	8.85×10^{-12}
Avogadro number N_A [mol ⁻¹]	6.02×10^{23}
charge of an electron e [C]	1.60×10^{-19}
(relative) permittivity of solvent ϵ_m	78.36
Temperature T [K]	298.15
Hamaker constant A [J]	5×10^{-21}
maximum surface separation h_{max} [nm]	38.8
concentration of the counter ion originally stuck to 2HT ρ_0 [mol/cm ³]	1.74×10^{-5}
valence of the ionic species Z	2
layer thickness δ [nm]	4.8
degree of counterion dissociation	0.1

4.3.6. Interactions between the 2HT membranes

To further quantify the interplay between the experimentally obtained Caillé parameter, η , and the interlayer spacing, d , we consider the electric double-layer repulsion and

Helfrich undulation interaction. The Helfrich undulation interaction is among the non-DLVO forces arising from the steric hindrance of the out-of-plane fluctuations of flexible membranes [7]. This leads to a long range repulsive force. According to Roux and Safinya [21,22], the compression modulus for the undulation interaction, B_{und} , can be calculated from the free energy per unit volume as

$$B_{\text{und}} = d \frac{9\pi^2(k_{\text{B}}T)^2}{64k_{\text{C}}} \frac{1}{(d - \delta)^4} \quad (4.17)$$

For systems in which interactions between the membranes are solely governed by the Helfrich undulation interaction, the Caillé parameter, η_{und} , is simply given by

$$\eta_{\text{und}} = \frac{4}{3} \left(1 - \frac{\delta}{d}\right)^2 \quad (4.18)$$

On the other hand, under the assumption that the compressibility of the system is dominated by electrostatic interaction, the compression modulus, B_{elc} , may be estimated as [20,22,28]

$$B_{\text{und}} = \frac{\pi^2 k_{\text{B}} T d}{2L(d - \delta)^3} \left(1 - 3 \frac{\Sigma}{\alpha L(d - \delta)} + 6 \frac{\Sigma^2}{\alpha^2 L^2 (d - \delta)^2} + \dots\right) \quad (4.19)$$

where Σ is the surface area of the surfactant molecule, α is the dissociation ratio of counterions, and L is defined as $L = \pi e^2 / (\epsilon_{\text{m}} k_{\text{B}} T)$, $l_{\text{B}} = e^2 / (\epsilon_{\text{m}} k_{\text{B}} T)$ being called the Bjerrum length and about 0.72 nm in water. Combining equations (4.11) and (4.19), the Caillé parameter for such electrically stabilized systems, η_{elc} , at low salt concentration is given by

$$\eta_{\text{und}} = \left(\frac{k_{\text{B}} T L}{2k_{\text{C}} d}\right)^{\frac{1}{2}} \left(1 - \frac{\delta}{d}\right)^{3/2} \left(1 - 3 \frac{\Sigma}{\alpha L(d - \delta)} + 6 \frac{\Sigma^2}{\alpha^2 L^2 (d - \delta)^2} + \dots\right)^{-1/2} \quad (4.20)$$

When using equation (4.19) and (4.20), the bending modulus of a single membrane, k_{C} , has to be treated as an unknown parameter. Soubiran et al. [26] claimed that membranes of cationic systems are far more rigid compared to the lamellar phase consisting of SDS,

in which $k_C \sim k_B T$ and consequently the undulation forces are thought to be dominant for the interactions between lamellae. If this is the case, the thermal fluctuations may not largely contribute to the stability of the membranes in a cationic lamellar phase, but they are expected to be stabilized almost exclusively by the electrostatic double layer repulsions, especially at low c_{salt} values. According to Mitchell and Ninham [63], when interactions between the membranes are exclusively dominated by electrostatic interactions, the bending rigidity for low salt concentrations, k_C^{LS} , can be approximated as

$$k_C^{\text{LS}} = \frac{\varepsilon_m}{\pi\chi} \left(\frac{k_B T}{e} \right)^2 \quad (4.21)$$

This gives, for instance, $k_C^{\text{LS}} = 1.04k_B T$ at $c_{\text{salt}} = 2.7 \text{ mmol L}^{-1}$, where $\chi^{-1} = 2.3 \text{ nm}$.

In Figure 4.14, we present the experimentally determined η as a function of d , in which the theoretically predicted η_{und} and η_{elc} are also shown. η_{elc} is calculated for $k_C = k_B T, 5k_B T, 10k_B T$, and k_C^{LS} . The α -gel shows $\eta (\approx 0.2)$, which is rather close to the prediction from the electric double-layer repulsion and $k_C \sim k_B T$. We observe that when the salt-induced transition from α -gel to MLV occurs, η is markedly increased. The η value (≈ 0.35) at $c_{\text{salt}} \approx 3 \text{ mmol L}^{-1}$, which is considerably greater than η_{elc} with $k_C = k_B T$ but is certainly smaller than η_{und} , cannot be explained in terms of the purely repulsive models. As pointed out in reference 11, attractive forces efficiently reduce the compression modulus B . Thus, the presence of attraction may potentially result in an increase of η . Therefore, the results indicate the operation of some attractive forces in the salt-added system. An additional attractive interaction due to ion–ion correlation effects [4,12,14], i.e., correlations between laterally mobile ions on the surface and those between ions in the diffuse double layers, is predicted. Indeed, fluctuations of both laterally mobile ions and the vertically diffusing ion cloud in the diffuse double-layers are detected by DRS. The

multidimensional fluctuations of the counterions and their correlations appear to induce extra attractive interactions that may cancel the double layer repulsion. Note that substitution of $k_C = 5k_B T$ or $10k_B T$ gives far smaller η_{elc} values, which are no longer comparable with the experimental η (Figure 4.14). As we have already shown, the least undulating membranes are formed at $c_{\text{salt}} \approx 10 \text{ mmol L}^{-1}$. A further increase of salt concentration to $> 25 \text{ mmol L}^{-1}$ leads to $h < \sim 3 \text{ nm}$, where the double-layer theory may not hold at such small separations, and highly disordered and far more undulating membranes than those predicted by the Helfrich interaction are produced. We suggest that the strongly undulating membrane formation at small separations should be partly related to the dynamical properties of the hydrated counterions.

The minimum in the Sogami–Ise potential appears as a consequence of the long-ranged weak attractive forces and the minimum becomes shallower at a higher salt concentration, as shown in Figure 4.13B [8]. Suppose that different from this prediction, if the attractive potential becomes deeper at a high salt concentration, the ordered structure should be more stabilized by the electrostatic attraction with a higher salt concentration. However, this is not the case for the present 2HT systems. Hachisu et al. [64] studied coexisting ordered and disordered structures in monodisperse polystyrene latexes. They showed that at a very low ion concentration, a stable iridescent (ordered) phase is formed, whose interparticle distance far exceeds the range of the van der Waals attraction. However, with increasing salt concentration, the ordered structure becomes unstable and the disordered phase appears as a whitish supernatant. Despite the large difference of the systems, our findings that the long-range ordering of the 2HT membranes most efficiently stabilized at a relatively low salt concentration ($c_{\text{salt}} \approx 10 \text{ mmol L}^{-1}$) and is rapidly destabilized at a higher salt concentration of $c_{\text{salt}} > \sim 25 \text{ mmol L}^{-1}$ are practically in line with the

observation of Hachisu et al [64].

When the surface separation reduces to less than 2–3 nm, hydration forces, known as an extremely strong short-range repulsion induced by the presence of tightly bound water molecules to ions or surfaces [3,4,6,13], are thought to be operative. Considering the size of the hydration shell of the ions, which is typically less than but rather close to 1 nm, the water layer between two membranes is mostly occupied by bound water molecules at surface separations of about 1–2 nm observed at $c_{\text{salt}} > \sim 25 \text{ mmol L}^{-1}$. However, in view of the sharp increase of η with decreasing d , hydration forces do not suppress the undulation fluctuation of the membranes. If the hydrating water layers are so strongly bound, how can they generate highly undulating membranes, instead of making them solid-like? This is likely to come either from the mobility of the bound ions themselves as detected by DRS or the exchange of hydration water molecules between the ions/surfaces.

We will further investigate these issues using different coions and counterions more strongly and weakly bound to water molecules. The results will be reported elsewhere.

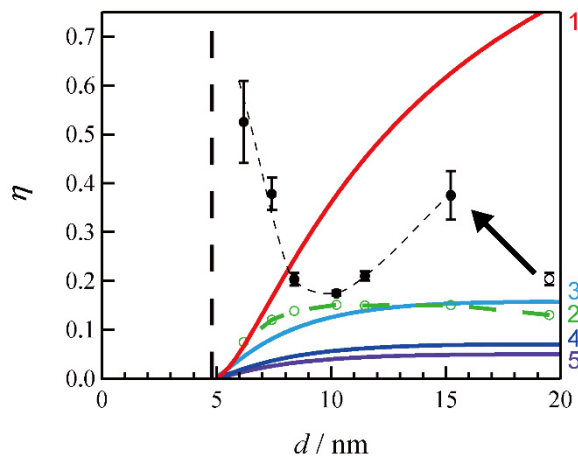


Figure 4.14. The Caillé parameter, η , plotted as a function of the interlayer spacing, d . The filled circles and the empty circle represent the experimental η values for the MLVs and the α -gel, respectively. A dashed curve is drawn as an eye guide. The theoretically predicted η values for the electric double-layer repulsion, η_{elc} , and the Helfrich undulation interaction, η_{und} (line 1), are also shown for comparison. η_{elc} is calculated for $k_{\text{C}} = k_{\text{B}}T$ (line 3), $5k_{\text{B}}T$ (line 4), $10k_{\text{B}}T$ (line 5), and k_{C}^{LS} (line 2) using equation (4.20). The vertical dashed line indicates the bilayer thickness, δ . An arrow highlights a jump of η accompanying the salt-induced α -gel-to-MLV transition.

4.4. Conclusions

The observed salt-induced α -gel-to-MLV transition in a dispersion of dialkylchain cationic surfactant (2HT), accompanied by a marked increase of the reservoir volume due to expelled solvent water, leads to a drastic decrease of the dispersion viscosity. This transition can be viewed as a pseudo unbound lamellar-to-bound lamellar transition, which appears to be driven by a counterion-mediated weak long-range attraction between the membranes although its generality and origin still need to be clarified. The DRS results demonstrate that the counterions fluctuate both vertically and laterally at the interface. The interference scattering observed in the small-angle regime was quantified

by the modified Caillé model [24,25,27,58]. An experimental η value for the α -gel (≈ 0.2) was found to be rather close to a predicted value from the electric double-layer repulsion. When the α -gel-to-MLV transition occurs, η is markedly increased. The η value at a low salt concentration cannot be explained without invoking weak long-range attractive forces. We infer that the dynamic properties of hydrated counterions may induce extra attractive forces between the membranes [4,12,14], which can lead to a reduction of B and the consequent increase of η . λ_S/κ sharply depends on whether an aqueous phase is in a permeable or an impermeable state. This clearly correlates with a drastic decrease of the dispersion viscosity with c_{salt} and its subsequent increase with a further increase of c_{salt} . The minimum of λ_S/κ appears at $c_{\text{salt}} \approx 10 \text{ mmol L}^{-1}$. Furthermore, the pronounced minimum of η_{und} the maximum of N at $c_{\text{salt}} \approx 10\text{--}20 \text{ mmol L}^{-1}$ demonstrate that the undulation fluctuation disorder of the MLV membranes is most efficiently suppressed and the long-range ordering of the membranes is most stabilized under this salinity condition. At $c_{\text{salt}} > 25 \text{ mmol L}^{-1}$, where the small surface separation of less than 2.5 nm is attained, highly disordered membranes are produced with no melting transition, which are far more undulating than that the Helfrich interaction model predicts. The actual interactions between the cationic membranes seem to be more complex than what is predicted by the existing continuum models. Our data suggest that the hydration forces, known as a very strong short-range repulsion caused by the presence of tightly bound water molecules to ions or surfaces [3,4,6,13], do not suppress the undulation fluctuation of the membranes under the present salinity conditions. The significant reduction of the bulk water relaxation amplitude cannot be entirely attributed to the irrotationally bound water molecules to ions and/or the interface, but it seems to come from depolarizing electric fields induced by the MLV architectures, as suggested for phospholipid MLV dispersions

[35]. This should be kept in mind when hydration effects in the MLV dispersions are discussed.

References

- [1] B. Derjaguin and L. Landau, *Acta Physicochim. URSS* 14, 633-662 (1941).
- [2] E. J. W. Verwey and J. T. G. Overbeek, *Theory of the stability of lyophobic colloids*, Elsevier (1948).
- [3] J.N. Israelachvili and P.M. McGuiggan, *Science* 241, 795-800 (1988).
- [4] J.N. Israelachvili, *Intermolecular and surface forces*, Academic Press (2011).
- [5] I. Langmuir, *J. Chem. Phys.* 6, 873-896 (1938).
- [6] D.M. LeNeveu, R.P. Rand, V. A. Parsegian, and D. Gingell, *Biophys. J.* 18, 209-230 (1977).
- [7] W. Helfrich, *Z. Naturforsch.* 33, 305-315 (1978).
- [8] I. Sogami, *Phys. Lett. A* 96, 199-203 (1983).
- [9] I. Sogami and N. Ise, *J. Chem. Phys.* 81, 6320-6332 (1984).
- [10] M. Smalley, *Mol. Phys.* 71, 1251-1267 (1990).
- [11] S.T. Milner and D. Roux, *J. Phys. I* 2, 1741-1754 (1992).
- [12] D. Lukatsky and S. Safran, *Phys. Rev. E* 60, 5848-5857 (1999).
- [13] J.I. Kilpatrick, S.-H. Loh, and S.P. Jarvis, *J. Am. Chem. Soc.* 135, 2628-2634 (2013).
- [14] C.A.S. Batista, R.G. Larson, and N.A. Kotov, *Science* 350, 1242477 (2015).
- [15] B.A. Coldren, H. Warriner, R. van Zanten, J.A. Zasadzinski, and E.B. Sirota, *Langmuir* 22, 2465-2473 (2006).
- [16] P. Fernandez, S. Schrödle, R. Buchner, and W. Kunz, *ChemPhysChem* 4, 1065-1072

(2003).

[17] C. Baar, R. Buchner, and W. Kunz, *J. Phys. Chem. B* 105, 2914-2922 (2001).

[18] F.S. Lima, H. Chaimovich, I.M. Cuccovia, and R. Buchner, *Langmuir* 29, 10037-10046 (2013).

[19] J. Marra, *J. Phys. Chem.* 90, 2145-2150 (1986).

[20] P. Richetti, P. Kékicheff, J. Parker, and B. Ninham, *Nature* 346, 252-254 (1990).

[21] C. Safinya, D. Roux, G. Smith, S. Sinha, P. Dimon, N. Clark, and A. Bellocq, *Phys. Rev. Lett.* 57, 2718-2721 (1986).

[22] D. Roux and C. Safinya, *J. Phys.* 49, 307-318 (1988).

[23] F. Nallet, R. Laversanne, and D. Roux, *J. Phys. II* 3, 487-502 (1993).

[24] R. Zhang, R.M. Suter, and J.F. Nagle, *Phys. Rev. E* 50, 5047-5060 (1994).

[25] G. Pabst, M. Rappolt, H. Amenitsch, and P. Laggner, *Phys. Rev. E* 62, 4000-4009 (2000).

[26] L. Soubiran, E. Staples, I. Tucker, J. Penfold, and A. Creeth, *Langmuir* 17, 7988-7994 (2001).

[27] T. Frühwirth, G. Fritz, N. Freiberger, and O. Glatter, *J. Appl. Crystallogr.* 37, 703-710 (2004).

[28] I. Tucker, J. Penfold, R.K. Thomas, I. Grillo, J.G. Barker, and D.F.R. Mildner, *Langmuir* 24, 6509-6520 (2008).

[29] T. Kunitake and Y. Okahata, *J. Am. Chem. Soc.* 99, 3860-3861 (1977).

[30] J.E. Brady, D.F. Evans, B. Kachar, and B.W. Ninham, *J. Am. Chem. Soc.* 106, 4279-4280 (1984).

[31] H.T. Jung, B. Coldren, J.A. Zasadzinski, D.J. Iampietro, and E.W. Kaler, *Proc. Natl. Acad. Sci. U. S. A.* 98, 1353-1357 (2001).

- [32] M. Aratono, A. Mori, I. Koga, M. Shigehisa, N. Onimaru, K. Tsuchiya, T. Takiue, and H. Matsubara, *J. Phys. Chem. B* 112, 12304-12311 (2008).
- [33] K. Bryskhe, S. Bulut, and U. Olsson, *J. Phys. Chem. B* 109, 9265-9274 (2005).
- [34] H. Kunieda and K. Shinoda, *J. Phys. Chem.* 82, 1710-1714 (1978).
- [35] R. Pottel, K.-D. Göpel, R. Henze, U. Kaatze, and V. Uhlendorf, *Biophys. Chem.* 19, 233-244 (1984).
- [36] C. Baar, R. Buchner, and W. Kunz, *J. Phys. Chem. B* 105, 2906-2913 (2001).
- [37] T. Chen, G. Hefter, and R. Buchner, *J. Phys. Chem. A* 107, 4025-4031 (2003).
- [38] T. Sato and R. Buchner, *J. Phys. Chem. A* 108, 5007-5015 (2004).
- [39] R. Buchner, in *Dielectric Spectroscopy of Solutions*, ed. J. Samios, and V. A. Durov, Springer, Netherlands, Dordrecht, 265-288 (2004).
- [40] T. Fukasawa, T. Sato, J. Watanabe, Y. Hama, W. Kunz, and R. Buchner, *Phys. Rev. Lett.* 95, 197802 (2005).
- [41] T. Sato, T. Akahane, K. Amano, R. Hyodo, K. Yanase, and T. Ogura, *J. Phys. Chem. B* 120, 5444-5454 (2016).
- [42] S. Havriliak and S. Negami, *Polymer* 8, 161-210 (1967).
- [43] D. Davidson and R. Cole, *J. Chem. Phys.* 18, 1417-1417 (1950).
- [44] K.S. Cole and R.H. Cole, *J. Chem. Phys.* 9, 341-351 (1941).
- [45] D. Orthaber, A. Bergmann, and O. Glatter, *J. Appl. Crystallogr.* 33, 218-225 (2000).
- [46] J. Lake, *Acta Crystallogr.* 23, 191-194 (1967).
- [47] C. Grosse, *J. Phys. Chem.* 92, 3905-3910 (1988).
- [48] *CRC Handbook of Chemistry and Physics*, ed. D. R. Lide and CRC Press, Boca Raton, New York, London, Tokyo, 76th edn (1995).
- [49] L. Soubiran, C. Coulon, P. Sierro, and D. Roux, *Europhys. Lett.* 31, 243-248 (1995).

- [50] E. Cavell, P. Knight, and M. Sheikh, *Trans. Faraday Soc.* 67, 2225-2233 (1971).
- [51] A.A. Zavitsas, *J. Phys. Chem. B* 109, 20636-20640 (2005).
- [52] M. Hishida and K. Tanaka, *Phys. Rev. Lett.* 106, 158102 (2011).
- [53] M. Schmollngruber, D. Braun, D. Oser, and O. Steinhauser, *Phys. Chem. Chem. Phys.* 18, 3606-3617 (2016).
- [54] A.S. Poulos, M. Nania, P. Lapham, R.M. Miller, A.J. Smith, H. Tantawy, J. Caragay, J. Gummel, O. Ces, E.S.J. Robles, and J.T. Cabral, *Langmuir* 32, 5852-5861 (2016).
- [55] A. Bóta, Z. Varga, and G. Goerigk, *J. Phys. Chem. B* 111, 1911-1915 (2007).
- [56] A. Bóta, Z. Varga, and G. Goerigk, *J. Appl. Crystallogr.* 40, s259-s263 (2007).
- [57] J.B.-Popela and O. Glatter, *J. Appl. Crystallogr.* 30, 431-442 (1997).
- [58] A. Caillé, *C. R. Acad. Sci. Ser. B* 274, 891-893 (1972).
- [59] O. Glatter, *J. Appl. Crystallogr.* 13, 577-584 (1980).
- [60] N. Senda, *Idemitsu Tech. Rep.* 49, 106-111 (2006).
- [61] M. Hishida, Y. Nomura, R. Akiyama, Y. Yamamura, and K. Saito, *Phys. Rev. E* 96, 040601 (2017).
- [62] F. Geng, R. Ma, A. Nakamura, K. Akatsuka, Y. Ebina, Y. Yamauchi, N. Miyamoto, Y. Tateyama, and T. Sasaki, *Nat. Commun.* 4, 1632 (2013).
- [63] D.J. Mitchell and B.W. Ninham, *Langmuir*, 5, 1121-1123 (1989).
- [64] S. Hachisu, Y. Kobayashi, and A. Kose, *J. Colloid Interface Sci.* 42, 342-348 (1973).

Chapter 5.

Intermolecular interactions and molecular dynamics in bovine serum albumin solutions

We used small angle x-ray scattering (SAXS) and dielectric relaxation spectroscopy (DRS) to clarify static structure and molecular dynamics of bovine serum albumin (BSA) in solution. SAXS allowed us to access spatial correlations of the protein molecules in concentrated solutions at different ionic strength. Using a well-established Fourier inversion technique, called SQ-IFT, we deduced the effective pair correlation functions, $g(r)^{\text{eff}}$, from the effective (or experimental) structure factors, $S(q)^{\text{eff}}$, without assuming any potential models for protein-protein interactions. In terms of $S(q)^{\text{eff}}$ and $g(r)^{\text{eff}}$, the mean nearest-neighbor distance, d^* , the osmotic compressibility, κ_{osm} , and the coordination number, N_C , were evaluated.

The complex dielectric spectra of aqueous BSA solutions measured in the frequency range from 1 MHz to 10 GHz were able to be decomposed into three relaxation processes having different physical origins. The highest frequency process, whose relaxation time was ca. 8 ps, was assigned to cooperative rearrangement of H-bond network of bulk water. We evaluated the effective hydration number of a BSA molecule, Z_{hyd} , using the bulk water relaxation amplitude. This approach yielded ca. 1200 hydrated water molecules per a BSA molecule, corresponding to ca. 0.3 g hydrated water per 1 g protein. The lowest frequency process having a relaxation time of ca. 50 ns was assigned to rotational diffusion of the BSA molecule. We confirmed that an effective molar volume of BSA calculated with Stokes-Einstein-Debye equation was identical to that predicted from its

molecular weight and specific density. According to the Kirkwood relationship, the dipole-dipole orientational correlation factor decreased with an increase of protein concentration, which indicated the operation of BSA-BSA interaction and favored antiparallel dipolar correlation between the protein molecules.

5.1. Introduction

Interactions between protein macromolecules in solution are of central importance in a number of areas, ranging from aggregation or segregation related to protein condensation diseases to protein crystallography. Small angle scattering of x-rays (SAXS) and neutrons (SANS) are highly efficient techniques to investigate protein-protein interactions in solution, and have been used for a number of globular proteins [1–9]. For example, Stradner et al. [1] discussed equilibrium cluster formation in concentrated lysozyme solution in view of the appearance of low- q (scattering vector) sub-peak position in their SANS structure factor. Conventional potential models, such as a hard sphere, a screened Coulomb [5–6], and a more complicated Derjaguin-Landau-Verwey-Overbeek (DLVO) potential model [2–4] have been applied to experimental scattering intensities of proteins in solution. However, in some cases, these potential models cannot fully explain rich behavior of proteins [7–9]. We infer that due to the complexity of structural features of proteins, e.g., irregular shape, distributed hydrophobic and hydrophilic patches, and inhomogeneous charge distributions, actual protein-protein interactions in solution may not fulfill an isotropic interaction assumed in these well-known potential models. Accordingly, we investigated spatial correlations of protein in solution at different ionic strength varying concentration between 4.99 mg mL^{-1} and 263.6 mg mL^{-1} by means of SAXS. Using an extended version of a well-established indirect Fourier transformation

(IFT) technique, the so-called SQ-IFT, the SAXS data was analyzed without assuming any potential models. Then, we tried to give an explanation of the structural quantities obtained with SQ-IFT.

Dynamical properties of protein solution are also of critical importance for understanding protein specific functions. Dielectric relaxation spectroscopy (DRS) observes collective dynamics of solute and solvent molecules. In the frequency range between 1 MHz and 10 GHz, two strong relaxation bands are observed for globular protein solutions, which are generally assigned to the collective reorientation of bulk water and rotational diffusion of the protein molecules. In addition, an intermediate frequency process between these two is also resolved. However, its assignment to tightly bound hydration water molecules is not yet very clear [10].

In this study, we investigated spatial correlations and molecular dynamics of bovine serum albumin (BSA) in solution. BSA is the most abundant plasma protein in bovine's blood stream. BSA is a counterpart of human serum albumin (HSA), exhibiting 75.8 % identity. BSA architecture is predominately helical, consisting of three domains that create heart-like shape. A primary function of BSA is transportation of hydrophobic molecules, which is achieved by its nonspecific ligand binding capability [11]. BSA also serves as an adjuster of colloid osmotic pressure (COP) of blood [11]. HSA showing isoelectric point (pI) of 4.7 carries a net negative charge of about 18 electronic charges at physiological pH [12]. BSA is also strongly negatively charged at physiological pH because its isoelectric point is ca. 5.3 [13], which is rather close to that of HSA.

5.2. Experimental Methods

5.2.1. Materials

For SAXS experiments, bovine serum albumin (BSA) was purchased from Sigma-Aldrich (product No. A7030). Two sets of several BSA samples in Millipore water and in 0.15 M phosphate buffered saline (PBS) solution (pH = 7.4, GIBCO®, Invitrogen) were prepared. Protein concentration, c , was calculated from weight fraction of BSA in solution and its partial specific volume ($v = 0.733$ and 0.741 cm³/g for BSA in aqueous solution and in PBS solution, respectively, which were determined by densitometry. For DRS experiments, the powdered BSA purchased from Wako Pure Chemical Industries (product No. STM1969) was used as received. The solid BSA was dissolved in Millipore water.

5.2.2. Small angle x-ray scattering (SAXS)

SAXS experiments on solutions of BSA were performed using a SAXSess camera (Anton-Paar, Graz, Austria). A sealed tube anode x-ray generator (GE Inspection Technologies, Germany) was operated at 40 kV and 50 mA. A focusing multilayer optics and a block collimator provide an intense monochromatic primary beam (Cu K α radiation, $\lambda = 0.1542$ nm) with a well-defined line shape (20 mm \times 300 μ m). A semi-transparent beam stop enabled a measurement of an attenuated primary beam at zero scattering vector. The samples were filled into a vacuum tight quartz capillary cell (ca. 1 mm ϕ) and set in a temperature controlled sample holder unit (TCS120, Anton Paar). Two-dimensional (2D) scattering intensity distribution recorded by an imaging-plate (IP) detector was read out by a Cyclone storage phosphor system (Perkin Elmer, USA). The 2D data was

integrated into a 1D scattering intensity, $I(q)$, as a function of the magnitude of the scattering vector

$$q = \frac{4\pi}{\lambda} \sin(\theta/2) \quad (5.1)$$

where θ is the total scattering angle.

All $I(q)$ data were normalized so as to have a uniform primary intensity at $q = 0$ for transmission calibration. The back ground scattering contributions from capillary and solvent were corrected. The absolute intensity calibration was made by referring to water intensity as a secondary standard [14].

5.2.3. Data Analysis

Small angle scattering of x-rays (SAXS) and neutrons (SANS) is a very efficient technique to study interparticle interactions in solution. The scattering intensity, $I(q)$, for a concentrated colloidal dispersion is given by the product of the form factor, $P(q)$, and the static structure factor, $S(q)$, as [15–17]

$$I(q) = nP(q)S(q) \quad (5.2)$$

where n is the particle number density.

$P(q)$ is a reciprocal-space function associated with the pair distance distribution function, $p(r)$, describing particle structure. These two functions are connected with each other *via* Fourier transformation [15,18,19] as

$$P(q) = 4\pi \int_0^{\infty} p(r) \frac{\sin qr}{qr} dr \quad (5.3)$$

On the other hand, the static structure factor, $S(q)$, is also given by Fourier transformation of the total correlation function, $h(r) = g(r) - 1$, as [20]

$$S(q) - 1 = 4\pi n \int_0^{\infty} [g(r) - 1] r^2 \frac{\sin qr}{qr} dr \quad (5.4)$$

where $g(r)$ is the pair correlation function describing spatial distribution of colloidal particles.

If we measure a scattering intensity at very low protein concentration, where intermolecular interactions can be neglected ($S(q) \approx 1$), the scattering curve exclusively represents intramolecular structure of the protein. In such a case, equation (5.2) is rewritten as

$$I(q) = nP(q)^{\text{exp}} \quad (5.5)$$

where $P(q)^{\text{exp}}$ is the experimental form factor.

Once we get $P(q)^{\text{exp}}$, the effective structure factor, $S(q)^{\text{eff}}$, can be deduced by dividing the concentration normalized intensity, $I(q)/c$, by $P(q)^{\text{exp}}$ as [21]

$$S(q)^{\text{eff}} = I(q)/cP(q)^{\text{exp}} \quad (5.6)$$

Using the relation given in equation (5.6), we transcribed $S(q)^{\text{eff}}$ into the effective pair correlation function, $g(r)^{\text{eff}}$, relying on indirect Fourier transformation (IFT) technique [15,18]. We call such an interaction potential model-free analytical technique of static structure factor SQ-IFT [21].

5.2.4. Dielectric relaxation spectroscopy (DRS)

To obtain specific information about states of the proteins and water in aqueous BSA solutions from a viewpoint of molecular dynamics, we determined complex dielectric spectra, $\varepsilon^*(\nu) = \varepsilon'(\nu) - i\varepsilon''(\nu)$, of aqueous BSA solutions at 25 °C in the frequency range from 1 MHz to 10 GHz using time domain reflectometry (TDR) [22].

5.3. Results and Discussion

5.3.1. Spatial correlations of BSA

Using SAXS, we investigated spatial correlations of BSA at protein concentrations of $4.00 < c / \text{mg mL}^{-1} < 264$ in water and in 150 mM PBS solution. These solvent conditions were chosen to minimize ionic strength and to achieve ionic strength and pH close to physiological conditions, respectively. Figure 5.1(a) and (b) show the concentration normalized scattering intensities of BSA, $I(q)/c$, in water and in 150 mM PBS solution at 25 °C on absolute scale. It is often the case that the maximum q value of SAXS and SANS experiments is limited to 3–5 nm^{-1} . In this study, we have extended the maximum q -range to ca. 28 nm^{-1} , covering a wide-angle regime. With increasing BSA concentration, we observed a decrease of forward intensity and appearance of a protein-protein positional correlation peak, which are manifestation of static structure factor, $S(q)$. Such behavior is more pronounced in water. To scrutinize these significant features, the effective structure factor, $S(q)^{\text{eff}}$, was extracted by dividing $I(q) / c$ by the experimental form factor, $P(q)^{\text{exp}}$, determined at lowest c in PBS solution.

$P(q)^{\text{exp}}$ determined in PBS solution was also used for aqueous BSA to obtain $S(q)^{\text{eff}}$ because in aqueous solution, intermolecular interference effects were not be perfectly eliminated even at $c = 4.99 \text{ mg mL}^{-1}$ due to only weakly screened long-range electrostatic repulsion. We found that conventional interaction potential models, such as hard sphere interaction or screened Coulomb interaction, did not fully describe the shape of $S(q)^{\text{eff}}$ (see Figure 5.1(c) and (d)). Even in PBS solution, $S(q) \approx 1$ at $c = 4.99 \text{ mg mL}^{-1}$ would not be exact. Consequently, $S(q)^{\text{eff}}$ in the forward direction $q < q^*$ may slightly be overestimated, where q^* is the protein-protein positional correlation peak position, related

to the mean nearest-neighbor distance between the proteins, d^* , as $d^* \approx 2\pi / q^*$.

We transcribed $S(q)^{\text{eff}}$ into a real space function, i.e., the effective pair correlation function, $g(r)^{\text{eff}}$, without imposing any potential models using SQ-IFT technique [21], which is based on the well-established IFT technique [18]. In this approach, we approximated $g(r)^{\text{eff}}$ using superposition of N B-spline functions, $\phi_\nu(r)$ ($\nu = 1, 2, \dots, N$) as

$$n[g(r) - 1]r^2 = \sum_{\nu=1}^N c_\nu \phi_\nu(r) \quad (5.7)$$

Then, $S(q)^{\text{eff}}$ was fitted with the Fourier transformation of the superposed B-spline functions given in equation (5.7)

$$S(q) - 1 = 4\pi n \int_0^\infty [g(r) - 1]r^2 \frac{\sin qr}{qr} dr = \sum_{\nu=1}^N c_\nu \psi_\nu(q) \quad (5.8)$$

where $\psi_\nu(q)$ is Fourier transformation of $\phi_\nu(r)$. In Figure 5.1, we show application of SQ-IFT to SAXS data for BSA in PBS solution and in water. The consequent $g(r)^{\text{eff}}$ functions for BSA at different ionic strength are shown in Figures 5.1 (e) and (f) as a function of c . We note that $g(r)^{\text{eff}}$ converges to unity for $r \rightarrow \infty$, which indicates that the number density at a high r region corresponds to the averaged number density, although the averaged number density depends on the solute concentration.

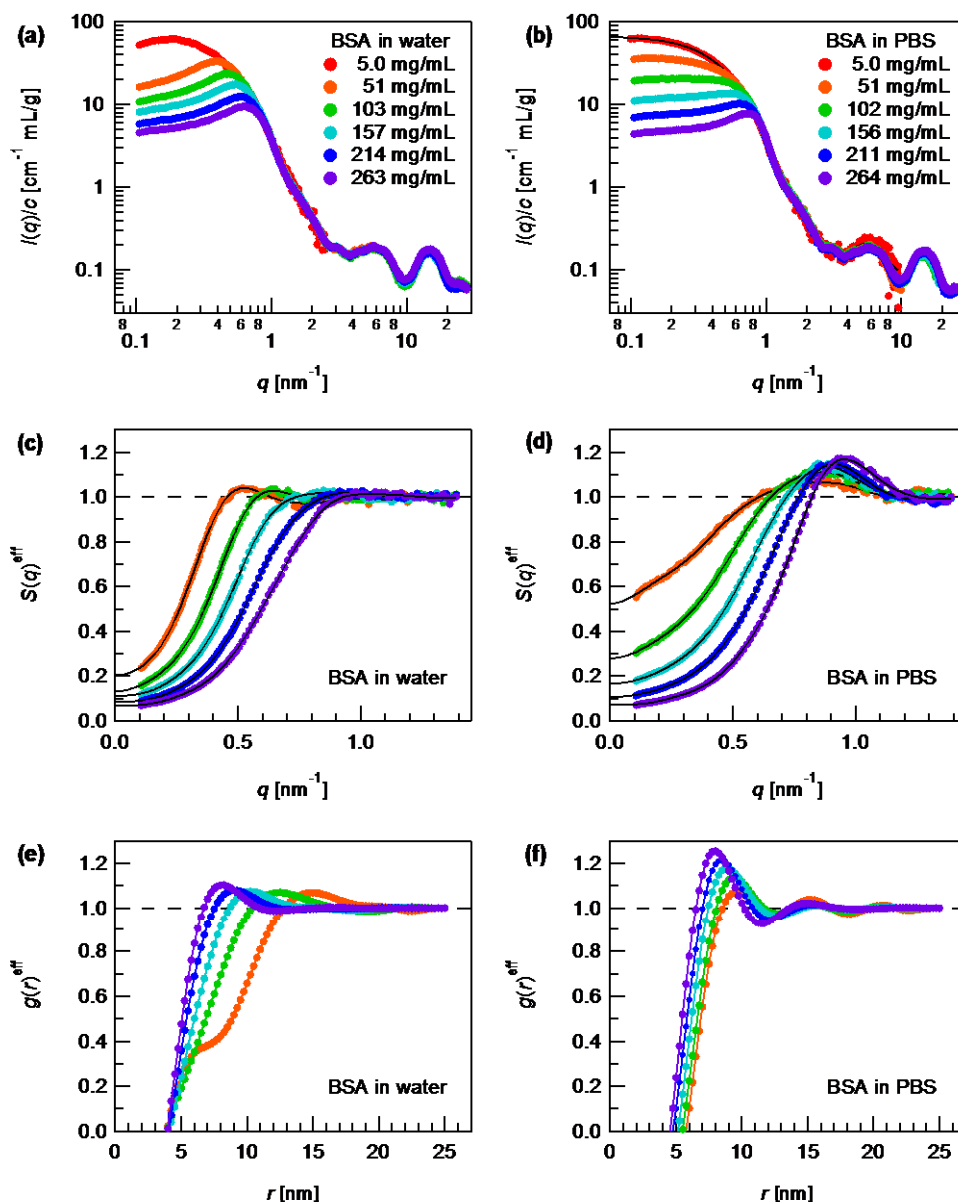


Figure 5.1. Effects of concentration and ionic strength on the spatial distributions of BSA in solution as obtained by SAXS. The concentration normalized SAXS intensities, $I(q)/c$, the experimental structure factors, $S(q)^{\text{eff}}$, and the effective (potential model-free) pair correlation functions, $g(r)^{\text{eff}}$, of BSA at 25°C (a, c, e) in water and (b, d, f) those in 150 mM PBS solution at pH = 7.4. $g(r)^{\text{eff}}$ was calculated from $S(q)^{\text{eff}}$ with an extended IFT technique (SQ-IFT) *via* the potential model-free route.

As shown in Figure 5.2, in terms of $S(q)^{\text{eff}}$ and $g(r)^{\text{eff}}$, a set of three structural parameters characterizing the BSA-BSA correlations in solution were calculated. The mean nearest-

neighbor distance between BSAs, d^* , was read out from the first peak position in $g(r)^{\text{eff}}$, which is systematically greater than those approximated as $d^* \approx 2\pi / q^*$ by referring to the peak position in $S(q)^{\text{eff}}$, and is expected to be more accurate. The extrapolated structure factors to zero scattering vector, $S(q \rightarrow 0)^{\text{eff}}$ are proportional to the osmotic compressibility of the system, κ_{osm} [23], and thus can be used as a measure of the net repulsive interaction between the proteins, where the ‘net repulsive interaction’ involves the excluded volume effect, the electrostatic repulsion, and a short-range attraction, which a number of globular proteins have been shown to exhibit.

In PBS, d^* slightly decreases with c , showing a linear-like behavior, and reaches a nearly identical value with a maximum diameter of BSA ($D_{\text{max}} \approx 8$ nm) at highest c . This indicates that the BSA-BSA interactions in PBS become short-ranged because the salt screens the electrostatic repulsion. In contrast, aqueous BSA exhibited far greater d^* and significantly smaller $S(q \rightarrow 0)^{\text{eff}}$ especially at low c , which demonstrates the stronger electrostatic repulsion between the BSA molecules than that in PBS solution. This is apparently due to a weaker screening effect of the electrostatic interactions at low ionic strength. Moreover, in aqueous solution, d^* decreased with c , holding a relation, $d^* \propto c^{-1/3}$. We point out that these are typical behavior of charged colloidal systems at low ionic strength because repulsively interacting charged colloidal particles in dispersion maximize their average interparticle distance. At highest c (≈ 250 mg mL⁻¹), both d^* and $S(q \rightarrow 0)^{\text{eff}}$ for aqueous BSA eventually converged to those in PBS solution.

Further, we extracted the coordination number, N_C , from $g(r)^{\text{eff}}$, which can be defined by an integration of $g(r)^{\text{eff}}$ as

$$N_C = 4\pi n \int_0^{r_{\text{min}}} g(r)^{\text{eff}} r^2 dr \quad (5.9)$$

where r_{min} is the distance corresponding to the first local minimum in $g(r)^{\text{eff}}$. We plot N_C

as a function of c (filled circles in Figure 5.2(c) and (d)). In PBS, N_C monotonously increases with c , approaching the value of close packing ($N_C \approx 12$) at highest c . In contrast, in aqueous solution, N_C is almost independent of c , and the value is close to the coordination number corresponding to close packing.

The markedly different c -dependence of N_C in water and in PBS solution is a manifestation of BSA-BSA spatial correlations influenced by different solvent conditions. In PBS solution, N_C is a rather straightforward increasing function of c which starts from nearly zero at $c = 0$. The linear-like increase of N_C with c , together with the nearly constant d^* values close to the maximum diameter of BSA, demonstrate that the number of (the center of mass of) BSA molecules involved in almost invariable space (about $4/3 \pi r_{\min}^3 \sim 7 \times 10^3 \text{ nm}^3$) is counted at all c to determine N_C . Therefore, we judge that the observed c -dependent behavior of N_C and d^* reflect increasing packing density in space having constant volume, as illustrated in Figure 5.2(e). By contrast, N_C is almost independent of c in aqueous solution, in which we observed operation of only weakly screened long-range electrostatic repulsion between BSAs, manifested in the relation, $d^* \propto c^{-1/3}$, and significantly smaller $S(q \rightarrow 0)^{\text{eff}}$ than that in PBS. Judging from these findings, there is no clear structural change of the spatial distributions of BSAs, but shrinkage of the lattice involving a nearly constant number of BSA molecules occurs. That is to say, N_C exhibits a nearly constant value corresponding to a random close pack at all c , as illustrated in Figure 5.2(f).

The definition based on equation (5.9) provides us with the reasonable and realistic values of N_C with respect to the number of central BSA's nearest neighbors. However, we note that there are a couple of different definitions for evaluating N_C in terms of the integration of $g(r)$ (Figure 5.2(c) and (d)), e.g., the integration up to the first peak position

(r_{\max}) of $g(r)$ (open square) and the integration up to twice longer distance than the first peak position ($2 \times r_{\max}$) of $g(r)$ (open triangle). N_C deduced by using the definition “integration up to the first peak position of $g(r)$ ” is roughly proportional to that calculated from equation (5.9), but the values in themselves appear to be too small to be interpreted as the number of the nearest neighbors. The definition, “integration up to twice longer distance than the first peak position of $g(r)$ (open triangle)”, resulted in unrealistically great values of N_C .

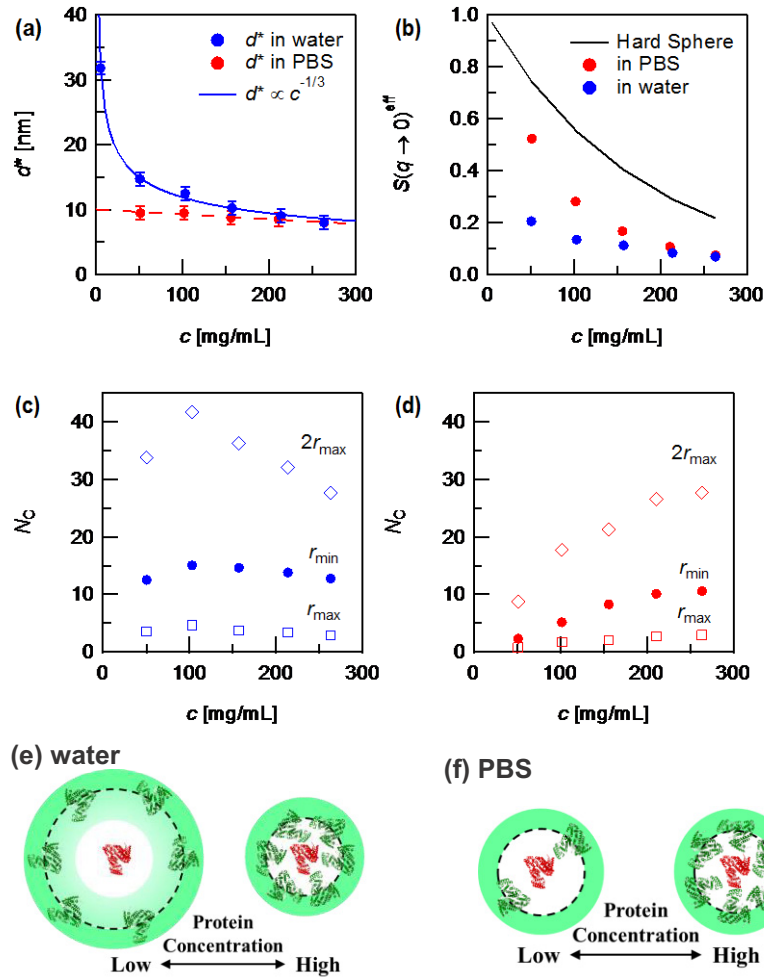


Figure 5.2. Effects of concentration and ionic strength on the protein-protein interactions in BSA solutions. (a) The mean nearest neighbor distance between the proteins, d^* , evaluated from the primary peak position in $g(r)^{\text{eff}}$, (b) the extrapolated structure factors to zero scattering vector, $S(q \rightarrow 0)^{\text{eff}}$, and the coordination number, N_c , (c) in water and (d) in PBS plotted as a function of BSA concentration, c . Schematic pictures of possible structural correlations between BSAs (e) in water and (f) in PBS are also shown. The green and light green areas represent the averaged and lower number density, respectively.

5.3.2. Collective dynamics of aqueous BSA

Figure 5.3 shows the complex dielectric spectra of aqueous BSA in $10.0 \leq c / \text{mg mL}^{-1} \leq 50.53$ at $25 \text{ }^\circ\text{C}$ in the frequency range of $0.001 \leq \nu / \text{GHz} \leq 10$. For a quantitative

description of the experimental $\varepsilon^*(\nu)$ spectra, we tested various conceivable relaxation models based on a superposition of n Havriliak-Negami (HN) equations, or its variants, using a non-linear least-squares fitting procedure. We found that a superposition of two Debye ($j = 1$ and $j = 2$) and one Cole-Cole ($j = 3$) relaxation functions,

$$\varepsilon^*(\nu) = \varepsilon_\infty + \frac{\Delta\varepsilon_1}{1 + i2\pi\nu\tau_1} + \frac{\Delta\varepsilon_2}{1 + i2\pi\nu\tau_2} + \frac{\Delta\varepsilon_3}{1 + (i2\pi\nu\tau_3)^{\beta_3}} \quad (5.10)$$

gave the best description to the spectra, where the j th dispersion step is defined by its relaxation time, τ_j ($\tau_j > \tau_{j+1}$) and amplitude, $\Delta\varepsilon_j$. ε_∞ is the infinite frequency permittivity, and β_j is the shape parameter representing symmetric broadening of the spectrum, respectively. τ_j and $\Delta\varepsilon_j$ of aqueous BSA solutions ($j = 1-3$) are shown in Figure 5.4. These relaxation processes $j = 3, 2,$ and 1 will be dealt with in 5.3.3, 5.3.5, and 5.3.4, respectively.

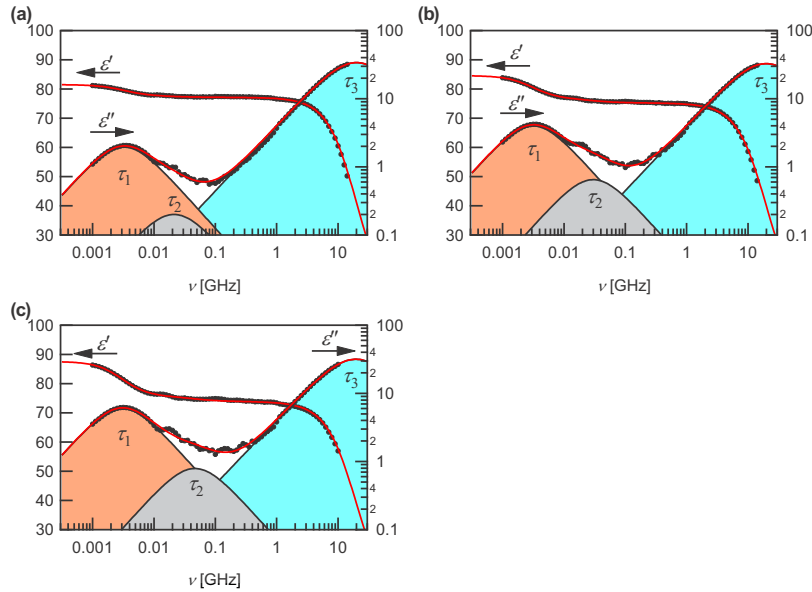


Figure 5.3. The dielectric dispersion, $\varepsilon'(\nu)$, and absorption, $\varepsilon''(\nu)$, spectra of aqueous BSA solutions at 25 °C at different concentrations of (a) $c = 10.0 \text{ mg mL}^{-1}$, (b) $c = 30.1 \text{ mg mL}^{-1}$, and (c) $c = 50.53 \text{ mg mL}^{-1}$. The solid curves are calculated from equation (5.10) based on the nonlinear least-squares fitting procedure.

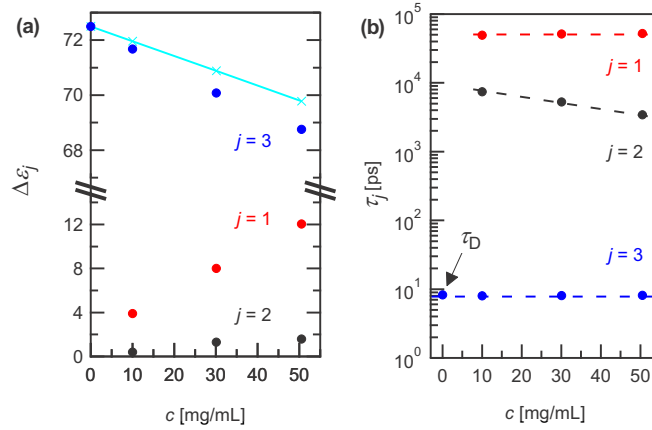


Figure 5.4. (a) Dielectric relaxation amplitudes, $\Delta\epsilon_j$, and (b) relaxation times, τ_j , of aqueous BSA solutions at 25 °C for the BSA rotational diffusion ($j = 1$), the ‘unclear’ intermediate ($j = 2$), and the bulk water ($j = 3$) processes as a function of protein concentration, c . Christcross symbols (\times) shown together with $\Delta\epsilon_3$ in the panel (a) represent the ideal bulk water amplitude predicted from the analytical water concentration under assumption that all water molecules in solution contribute to the bulk water process ($j = 3$). The data of pure water ($c = 0$) is referred from a reference [24].

5.3.3. Hydration of the BSA molecules

The relaxation time of the highest frequency process, τ_3 , is nearly identical with the Debye relaxation time of bulk water, $\tau_D = 8.3$ ps [24–28], and almost independent of the protein concentration, c . Therefore, the process is clearly attributed to the cooperative H-bond rearrangement dynamics of bulk-like water [24].

Using the experimentally obtained bulk water amplitude, $\Delta\epsilon_3$, we evaluated the effective hydration number of a BSA molecule, Z_{hyd} . The generalized Cavell equation [29]

$$\Delta\epsilon_i = \frac{\epsilon}{3(\epsilon + (1 - \epsilon)A_i)} \frac{N_A}{k_B T \epsilon_0} \frac{g_i \mu_{Gi}^2}{(1 - \alpha_i f_i)^2} c_i \quad (5.11)$$

connects the relaxation amplitude of the i th dispersion step, $\Delta\epsilon_i$, to the concentration of the relaxation species, c_i , where μ_{Gi} is a gas-phase dipole moment, α_i a polarizability, A_i

the shape parameter of the reaction field, ε the static permittivity, g_i the dipole-dipole correlation factor, k_B the Boltzmann constant, N_A the Avogadro's number, ε_0 the vacuum permittivity, f_i the field factor defined as [29]

$$f_i = \frac{1}{4\pi\varepsilon_0 r^3} \frac{2\varepsilon - 2}{2\varepsilon + 1} \quad (5.12)$$

Equation (5.11) normalized to pure water yields the apparent water concentration, $c_w^{\text{app}}(c)$, at protein molar concentration c as

$$c_w^{\text{app}}(c) = c_w(c) \frac{g_w(c)}{g_w(0)} = \frac{\varepsilon(0)(2\varepsilon(c) + 1) (1 - \alpha_w f_w(c))^2 \Delta\varepsilon_w(c)}{\varepsilon(c)(2\varepsilon(0) + 1) (1 - \alpha_w f_w(0))^2 \Delta\varepsilon_w(0)} c_w(0) \quad (5.13)$$

where $\Delta\varepsilon_w(0) = 72.5$ and $\Delta\varepsilon_w(c) = \Delta\varepsilon_3(c)$. Assuming a spherical water molecule ($A_i = 1 / 3$) having a radius $r = 0.1425$ nm, a gas-phase dipole moment $\mu_{Gi} = 1.85$ D, and a polarizability $\alpha_i = 1.607 \times 10^{-40}$ C m² / V, the apparent water concentration of bulk water, $c_w^{\text{app}}(c)$, i.e., the molar concentration of water molecules that can still contribute to the bulk water relaxation process in solution, can be evaluated. Then we define Z_{hyd} by converting the difference between the apparent water concentration, $c_w^{\text{app}}(c)$, and the analytical water concentration, $c_w(c)$, to the corresponding number of water molecules per BSA molecule (Figure 5.4(c))

$$Z_{\text{hyd}} = [c_w(c) - c_w^{\text{app}}(c)] / c \quad (5.14)$$

The mass of hydrated water molecule per unit mass (1 g) of protein, M_{hyd} , can be also calculated as $M_{\text{hyd}} = [Z_{\text{hyd}} \times M_w] / M$, where M_w and M are molecular mass of water and BSA, respectively. According to the definition of Z_{hyd} given by equation (5.14), one can interpret Z_{hyd} as the number of water molecules that cannot contribute to the bulk water relaxation process due to solvation effects.

As a result, we obtained 1.2×10^3 hydrated water molecules per BSA molecule, which correspond to ca. 0.3 g of water per unit mass (1 g) of BSA (Figure 5.5). The value is

broadly consistent with those obtained by thermodynamic measurements for globular proteins ($0.2 < M_{\text{hyd}} / [\text{g} / 1 \text{ g protein}] < 0.4$) [30].

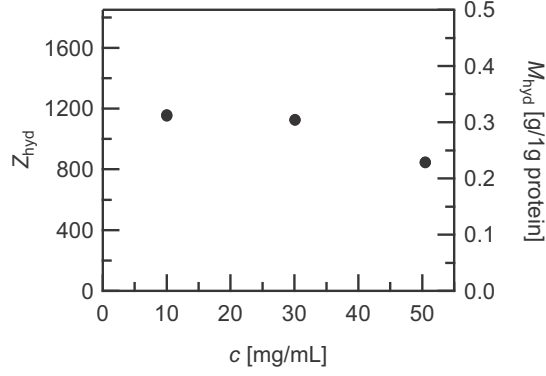


Figure 5.5. The effective hydration number of a BSA molecule, Z_{hyd} , as a function of c . Reference to the right axes gives the effective mass of hydrated water molecules per one gram protein, M_{hyd} . These quantities are calculated from the concentration dependence of the bulk water relaxation amplitude, $\Delta\varepsilon_3$, based on the generalized Cavell equation. Z_{hyd} explains the number of water molecules that cannot contribute to the bulk water process due to the solvation effect.

5.3.4. Rotational diffusion of BSA molecules

If dipoles relax by rotational diffusion, as is expected for BSA, the microscopic relaxation time [31], τ_1' , is determined by the solution viscosity, η , and follows the modified Stokes-Einstein-Debye (SED) equation [32,33]

$$\tau_1' = \frac{2\varepsilon + \varepsilon_{\infty,1}}{3\varepsilon} \tau_1 = \frac{3V_{\text{eff}}\eta}{k_{\text{B}}T} \quad (5.15)$$

where $\varepsilon_{\infty,1}$ is the high-frequency limit of the $j = 1$ process. Since the identical relaxation time, $\tau_1 \approx 51$ ns, provides virtually identical effective molar volume of BSA, $V^{\text{eff}} \approx 4.6 \times 10^4 \text{ cm}^3 \text{ mol}^{-1}$ compared to $4.93 \times 10^4 \text{ cm}^3 \text{ mol}^{-1}$ calculated from the partial specific volume ($\nu = 0.7425 \text{ cm}^3 \text{ g}^{-1}$) and the molecular weight ($M = 66.4 \text{ kDa}$), this process is assigned to the rotational diffusion of the BSA.

On the other hand, the relaxation amplitude of the lowest frequency process showed an upward convex curve with increasing protein concentration. If we interpret such behavior based on Onsager-Onsley model, the effective dipole moment, μ^{eff} , of the BSA is a decreasing function with c due to a decrease of the Kirkwood's dipole-dipole orientational correlation factor, g . This result indicates the operation of the BSA-BSA interaction and favored antiparallel dipolar correlations between protein molecules.

5.3.5. An assignment of the intermediate frequency process

In previous DRS studies, the intermediate frequency process of protein solution centered at ca. 500 MHz was assigned to kinetics of hydrated water. These studies suggested that such tightly bound water molecules should interact with the protein surface and exhibit a nanosecond relaxation time [34–37]. In this study, the relaxation time of the intermediate frequency process is evaluated to ca. 5 ns, which is nearly identical with that of tightly bound water according to the previous classification. However, this assignment may imply approximately thousand times slower reorientation of hydrated water molecules than that of bulk water. Recent NMR studies and molecular dynamics simulations [38–40] may call for a different interpretation of this relaxation process. These studies concluded that the rotational relaxation of water in the vicinity of a globular protein was less than 10 times slower than that of the bulk water. Therefore, the intermediate frequency process may not be directly linked with very slow motions of strongly bound water molecules, but rather may arise from some coupled protein–water motions. We also point out that the relaxation time (~ 5 ns) is nearly identical with those of counter ion fluctuations observed in a dispersion of charged colloidal particles having similar size to globular proteins [41,42]. We will try to renovate the assignment of the intermediate

process by precisely controlling ionic concentration.

5.4. Conclusions

In this study, we have revealed the spatial correlations and corrective dynamics of BSA using SAXS and DRS. First, we investigated spatial correlations of BSA in solution using an interaction potential model-free analysis of experimental static structure factor, $S(q)^{\text{eff}}$ (SQ-IFT). Such approach is advantageous especially when $S(q)^{\text{eff}}$ of proteins is fairly different from those predicted for the conventional interaction models, as observed for BSA. $g(r)^{\text{eff}}$ was calculated from $S(q)^{\text{eff}}$, which allowed us to access three independent structural quantities, the mean nearest-neighbor distance between the BSA molecules, the osmotic compressibility of the system, and the coordination number of BSA. From the viewpoint of these structural features, especially the coordination number, N_C , we were able to understand how the spatial correlations of BSA depended on solvent ionic strength. In PBS solution, screened electrostatic repulsion, manifested in the nearly constant d^* values, led to the linear-like increase of N_C with c , which was interpreted as an increase of packing density with increasing c . In aqueous solution, N_C exhibits a nearly constant value around that of a random close pack. This was due to the operation of an only weakly screened long-range electrostatic repulsive interaction, which was reflected in the relation, $d^* \propto c^{-1/3}$, and significantly smaller $S(q \rightarrow 0)^{\text{eff}}$ than that in PBS. These findings demonstrated that there was no clear structural change of the spatial distributions of BSAs, but shrinkage of the lattice involving a nearly constant number of BSA molecules occurred.

In DRS study, we evaluated hydration number of a BSA molecule using the bulk water relaxation amplitude. The result was broadly consistent with those obtained by

thermodynamic measurements [30], yielding ca. 0.3 g hydrated water per unit mass (1 g) of BSA at $c \rightarrow 0$. The lowest frequency process showing a relaxation time of ca. 50 ns was assigned to rotational diffusion of BSA. The concentration dependence of the relaxation amplitude given rise to by the BSA rotational diffusion indicated operation of BSA-BSA interaction even at low $c < 50 \text{ mg mL}^{-1}$ and favored antiparallel dipolar correlations between the BSA molecules. The relaxation amplitude of the intermediate frequency process rapidly grew with an increase of c . The relaxation time of this process was close to that of ‘tightly bound water’ according to the interpretation given in previous DRS studies [34–37]. However, the solid assignment still remains to be given. In future works, we will examine effects of counter ion fluctuations around protein molecules.

References

- [1] A. Stradner, H. Sedgwick, F. Cardinaux, W.C.K. Poon, S.U. Egelhaaf, and P. Schurtenberger, *Nature*. 432, 492-495 (2004).
- [2] G. Pellicane, D. Costa, and C. Caccamo, *J. Phys. Condens. Matter* 16, S4923-S4936 (2004).
- [3] A. Tardieu, A.L. Verge, M. Malfois, F. Bonnete, S. Finet, M.R. Kautt, and L. Belloni, *J. Cryst. Growth*. 196, 193-203 (1999).
- [4] B. Lonetti, E. Fratini, S. H. Chen, and P. Baglioni, *Phys. Chem. Chem. Phys.* 6, 1388-1395 (2004).
- [5] Y. Liu, E. Fratini, P. Baglioni, W. Chen, and S. Chen, *Phys. Rev. Lett.* 95, 118102 (2005).
- [6] F. Zhang, M.W.A. Skoda, R.M.J. Jacobs, R.A. Martin, C.M. Martin, and F. Schreiber, *J. Phys. Chem. B* 111, 251-259 (2007).

- [7] M.L. Broide, T.M. Tominc, and M.D. Saxowsky, *Phys. Rev. E* 53, 6325-6335 (1996).
- [8] R. Piazza, *Curr. Opin. Colloid Interface Sci.* 8, 515-522 (2004).
- [9] A. Striolo, D. Bratko, J.Z. Wu, N. Elvassore, H.W. Blanch, and J.M. Prausnitz, *J. Chem. Phys.* 116, 7733-7743 (2002).
- [10] A. Oleinikova, P. Sasisanker, and H. Weingärtner, *J. Phys. Chem. B* 108, 8467-8474 (2004).
- [11] A. Bujacz, *Acta Cryst.* 68, 1278-1289 (2012).
- [12] T. Peters, *All about Albumin, Biochemistry, Genetics, and Medical Applications* Academic, New York (1996).
- [13] J.F. Foster and L.J. Kaplant, *Biochemistry* 10, 630-636 (1971).
- [14] D. Orthaber, A. Bergmann, and O. Glatter, *J. Appl. Crystallogr.* 33, 218-225 (2000).
- [15] O. Glatter, *J. Appl. Crystallogr.* 10, 415-421 (1977).
- [16] A. Shukla, E. Mylonas, E. Di Cola, S. Finet, P. Timmins, T. Narayanan, and D.I. Svergun, *Proc. Natl. Acad. Sci. U. S. A.* 105, 5057-5080 (2008).
- [17] T. Sato, H. Sakai, K. Sou, R. Buchner, and E. Tsuchida, *J. Phys. Chem. B.* 111, 1393-1401 (2007).
- [18] O. Glatter, *Acta Phys. Austriaca.* 47, 83 (1977).
- [19] G. Porod, *Acta Phys. Austriaca.* 2, 225-292 (1948).
- [20] F. Zernike and J.A. Prins, *Z. Phys.* 41, 184-194 (1927).
- [21] T. Fukasawa and T. Sato, *Phys. Chem. Chem. Phys.* 13, 3187-3196 (2011).
- [22] T. Sato and R. Buchner, *J. Phys. Chem. A* 108, 5007-5015 (2004).
- [23] G.R. Strobl, *The Physics of Polymers*, Springer (2007).
- [24] T. Fukasawa, T. Sato, J. Watanabe, Y. Hama, W. Kunz, and R. Buchner, *Phys. Rev. Lett.* 95, 197802 (2005).

- [25] U. Kaatze, *J. Chem. Eng. Data* 34, 371-374 (1989).
- [26] J. Barthel, K. Bachhuber, R. Buchner, and H. Hetzenauer, *Chem. Phys. Lett.* 165, 369-373 (1990).
- [27] R. Buchner, J. Barthel, and J. Stauber, *Chem. Phys. Lett.* 306, 57-63 (1999).
- [28] U. Kaatze, R. Behrends, and R. Pottel, *J. Non Cryst. Solids* 305, 19-28 (2002).
- [29] J. Barthel, H. Hetzenauer, and R. Buchner, *Ber. Bunsen-Ges. Phys. Chem.* 96, 1424-1432 (1992).
- [30] L.D. Kuntz and W. Kauzmann, *Adv. Protein. Chem.* 28, 239-345 (1974).
- [31] J.P. Powles, *J. Chem. Phys.* 21, 633-637 (1953).
- [32] J.L. Dote, D. Kivelson, and T.N. Schwartz, *J. Phys. Chem.* 85, 2169-2180 (1981).
- [33] J.L. Dote and D. Kivelson, *J. Phys. Chem.* 87, 3889-3893 (1983).
- [34] M. Wolf, R. Gulich, P. Lunkenheimer, and A. Loidl, *Biochim. Biophys. Acta.* 1824, 723-730 (2012).
- [35] M. Suzuki, J. Shigematsu, and T. Kodama, *J. Phys. Chem.* 100, 7279-7282 (1996).
- [36] R. Pethig, *Annu. Rev. Phys. Chem.* 43, 177-205 (1992).
- [37] C. Cametti, S. Marchetti, C.M.C. Gambi, and G. Onori, *J. Phys. Chem. B.* 115, 7144-7153 (2011).
- [38] K. Modig, E. Liepinsh, G. Otting, and B. Halle, *J. Am. Chem. Soc.* 126, 102-114 (2004).
- [39] F. Sterpone, G. Stirnemann, and D. Laage, *J. Am. Chem. Soc.* 134, 4116-4119 (2012).
- [40] M. Marchi, F. Sterpone, and M. Ceccarelli, *J. Am. Chem. Soc.* 124, 6787-6791 (2002).
- [41] P. Fernandez, S. Schrödle, R. Buchner, and W. Kunz, *ChemPhysChem* 4, 1065-1072 (2003).

[42] C. Grosse, J. Phys. Chem. 92, 3905-3910 (1988).

Chapter 6. Conclusions

6.1. Summary

In this section, I recapitulate the representative and specific results of the research presented in this thesis. In my doctoral study, I have extended the knowledge of how static structure and cooperative dynamics occurring in the mesoscopic length scales are related to macroscopic physical properties in a series of soft materials, such as thermo-responsive polymer, dialkyl chain cationic surfactant, and natural globular protein, in aqueous media. In order to clarify the mesoscopic structure involving cooperative dynamics of ions, solute, and solvent molecules, I have used simultaneous small- and wide-angle x-ray scattering (SWAXS) covering the length scale typically between 0.2 and 100 nm and dielectric relaxation spectroscopy (DRS) in the microwave-to-millimeter wave frequency region. This combination has been proven to be very efficient to deepen the mesoscopic paradigm.

In chapter 1, I summarize previous representative works on soft complex systems, such as thermo-responsive polymers and gels, bilayer membranes, and protein-protein interactions, and have given a brief description of the essential meanings and the major purpose of this research.

In chapter 2, I have explained the theoretical background of the scattering and spectroscopic techniques and the experimental methods and analyses used in this work.

In chapter 3, I have discussed microscopic aspects of the phase transition of poly(*N*-isopropylacrylamide) (pNIPAm) in aqueous media, providing the experimental evidence that critical fluctuations and dehydration of the pNIPAm chains are closely coupled. I

point out that the diverging behavior of the length scale and the magnitude of the density fluctuation arising from the swollen coil polymer network indicates the segregation of the system into nanometer-sized polymer-rich and water-rich domains. I have unambiguously demonstrated that the low- q peak, whose length scale is far greater than that of the intra-chain radial distributions, originates from the intrinsic density fluctuations reflecting the globule state of pNIPAm. Importantly, the microglobules already exist in the one-phase region far below spinodal temperature T_S . Besides the ordinary (density) order parameter, which generally monitor the phase states, the local number density of these microglobules acts as a counterpart of the ordinary order parameter. In other words, it should be identified as a microscopic order parameter governing the phase transition of aqueous pNIPAm solution. I have also settled a pending issue when using small-angle neutron scattering (SANS), namely the solvent deuterium isotope effects on the critical behavior of pNIPAm in aqueous media. I have been able to clearly show similarity and substantial difference of the critical fluctuation of pNIPAm in H_2O and D_2O , observing about 1 K higher T_S in D_2O and almost identical critical exponents independent the solvent conditions.

In chapter 4, I have focused on the interplay between the salt-induced drastic reduction of the dispersion viscosity of water/dialkylchain cationic surfactant (2HT) systems and the underlying intermembrane interactions and counterion fluctuations at the interface. Industrially, inorganic salts are known as viscosity modifiers for dialkylchain cationic surfactant dispersions, which play an important role in the formulation of base materials of fabric softeners. I have revealed that the α -gel-to-multi lamellar vesicle (MLV) transition upon addition of a tiny amount of salt is caused by the exclusion of a large amount of solvent water confined between the bilayer membranes in the lamellar gel

phase. As a result of the Grosse analysis of the relaxation amplitude reflecting the counterion fluctuations in the vicinity of the membrane surface, during the α -gel-to-MLV transition, not only the conductivity, κ , of the dispersion exhibits a sharp increase but a pronounced decrease of λ_s/κ , where λ_s is the surface conductivity at the interface, is closely coupled to the drastic reduction of the dispersion viscosity. These findings strongly indicate the α -gel-to-MLV transition is accompanied by the change of the percolation state of the system, i.e., the transition from impermeable to permeable states of the outer aqueous phase. Although the α -gel-MLV transition can be regarded as a pseudo unbound lamella-to-bound lamella transition, the slit-concentration dependent interlayer spacing cannot be explained by van der Waals attraction. The SAXS analysis based on the modified Caillé theory has quantified the intermembrane interactions involving the undulation fluctuation disorder (UFD) of the membranes. The data have revealed that a weak long-range attractive force is operative and the hydration forces do not suppress the undulation fluctuation of the membranes. I have pointed out that in view of the strikingly and unlikely small bulk water relaxation amplitudes, the reduction of the internal electric field acting on the interlamellar water should be taken into account in addition to the effects of genuine hydration of ions and surfactant molecules when hydration effects in the charged bilayer systems like α -gels and MLVs are discussed.

In chapter 5, I have investigated on the intermolecular interactions of bovine serum albumin (BSA) in solution. BSA is a stereotype of human serum albumin (HSA), preserving colloid osmotic pressure (COP) of blood and transporting water insoluble molecules in vivo. In detail, I have discussed effects of solvent ionic strength and protein concentration on the BSA-BSA interactions. I have found that the dielectric relaxation amplitude assigned to the BSA rotational diffusion decreases with increasing BSA

concentration, c_{BSA} . The fact indicates operation of rotationally anisotropic BSA-BSA interactions in which antiparallel dipolar correlations of the BSA molecules are favored. This implies that use of isotropic interaction potential models for the structure factor analysis in SAXS experiments is not necessarily appropriate. Spatial correlations of BSA in solution is scrutinized by using a structure-factor indirect Fourier transformation (SQ-IFT), an interaction potential model-free Fourier inversion analysis of the experimental static structure factor, $S(q)^{\text{eff}}$, defined as the normalized SAXS intensity divided by the experimental form factor. The resulting $g(r)^{\text{eff}}$ allows us to access two independent structural quantities, the mean nearest-neighbor distance between the BSA molecules, d^* , and the coordination number of BSA, N_C . The yielded quantities have revealed how the spatial correlations of BSA depend on c_{BSA} and solvent ionic strength. In the high ionic strength solvent (150mM PBS solution), d^* depends hardly on the c_{BSA} , whereas only N_C increases approximately in proportion to c_{BSA} . These observations are interpreted as an increase of the packing density of BSA molecules with increasing c_{BSA} because of efficiently screened long-range electrostatic repulsion. In contrast, in the low ionic strength solvent (water), d^* decreases with c_{BSA} roughly obeying $d^* \propto c_{\text{BSA}}^{-1/3}$ while N_C remains nearly constant. The hydration number evaluated from the bulk water amplitude based on the Cavell theory also decreases with c_{BSA} as the hydration shells of different BSA molecules overlap. The osmotic compressibility, $S(q \rightarrow 0)^{\text{eff}}$, is found to be significantly smaller than that in the high ionic strength solvent due to the operation of only weakly screened long-range electrostatic repulsion. These findings have demonstrated shrinkage of the coordination shell with c_{BSA} while preserving N_C .

In chapter 6, I have summarized the results of the research done in my doctoral work

and described future prospects of a possible expansion and developments of this research.

6.2. Future Prospects

6.2.1. Polymer system

Coexistence of alcohols [1, 2] and inorganic salts [3] affects the phase behavior of aqueous pNIPAm solution. For instance, pNIPAm is soluble in water and methanol at room temperature but a mixture of these two good solvents becomes a poor solvent depending on the solvent composition. This phenomenon is called cononsolvency. Analogously, the volume-phase transition (VPT) of pNIPAm-based gels from a swollen state to a collapsed state is induced by adding alcohols or other organic molecules like acetone and DMSO at constant temperature [4]. Understanding the behavior of macromolecules in a multi-component solvent give useful information about the in vivo environment. However, the microscopic origin of these intriguing phenomena still remains elusive and controversy. Tanaka et al. proposed a competitive hydrogen bonding picture, in which competitive hydrogen bond formation of water and methanol molecules with the polymer chain causes the cononsolvency of pNIPAm [5]. Trappe and co-workers argued that the mean energetic state of the aqueous medium determines hydrophobic hydration of pNIPAm that governs the phase transition of pNIPAm [6]. To settle the dispute about the underlying mechanisms of the cononsolvency, it is highly desirable to quantify the solvation number of water and alcohol molecules as a function of temperature and solvent composition, which may be able to done by extending very accurate DRS experiments performed in this study. I also expect from the results and findings of the pNIPAm/water systems presented in this thesis that monitoring how the local number

density of the microglobules, i.e., the microscopic order parameter identified in this study, changes during the transitions should give further microscopic structural insights into the cononsolvency phenomena. In addition, these strategies can be applied to all kinds of the thermo-responsive polymers, such as poly(*N*-isopropylmethacrylamide) and poly(*N*-alkylacrylamide), and thermo-responsive gels synthesized by crosslinking these polymers.

6.2.2. Bilayer system

Although I have obtained detailed information about the effects of CaCl₂ on the membrane-membrane interactions in the MLV dispersion of dialkyl chain cationic surfactant (2HT), we need to extend the present knowledge to the effects of other inorganic salt additives, in which the influence of the valency of co-ions should be investigated by using NaCl and KCl. If we use other quaternary ammonium salt surfactants like dialkyl ammonium bromide, instead of dialkyl ammonium chloride, we can also investigate the effects of different counterions. Incorporation of coil polymers or other surfactant molecules into the interlamellar aqueous phase also alter intermembrane interactions [7, 8], the latter being known to be efficient to improve dispersion stability of MLVs [9, 10]. Such effects should be also interesting and important both scientifically and industrially. By comprehensively examining all these factors, we will be able to clarify the origin of the weak long-range attraction that is necessary to be invoked for explaining the observed structural properties; its generality should be confirmed.

Phospholipids, such as 1,2-dipalmitoyl-sn-glycero-3-phosphocholine (DPPC) and 1,2-distearoyl-sn-glycero-3-phosphoethanolamine (DSPE), having two fatty acids and a phosphate ester moiety in their molecular structure form lipid bilayers because of their amphiphilic nature and the molecular architecture [11, 12]. Phospholipids serve as a major

component of cell membranes and also form uni-lamellar or multi-lamellar vesicles depending on the preparation conditions. If we extend the present methods established in this study, we will be able to reveal membrane-membrane interactions of lipid bilayers (in particular targeting undulation fluctuation disorder), ion fluctuation at the interface, and hydration effects depending on temperature, lipid concentration, ionic strength of solvent, and types of co-existing ion species for different phases, e.g., a lamellar crystalline phase (L_C), a lamellar gel phase (L_β) and a ripple gel phase (P_β'), and liquid crystal phase (L_a).

In this study, effects of the depolarizing electric fields and genuine hydration inferred from the strikingly small bulk water relaxation amplitude observed in aqueous 2HT dispersions are not able to be separated in a quantitative manner. To overcome this issue, quantification of the internal electric field created from the charged membranes should be considered based on the theory proposed by Steinhauser [13].

6.2.3. Protein system

The successful application of the SQ-IFT technique to aqueous BSA solutions highlight its eminent efficiency for visualizing spatial distributions of proteins in real space. If we use a Fourier inversion technique for dilute systems in a more conventional way, this can of course be an excellent tool to pursue a polymerization process of proteins and the structure of protein assemblies.

The cooperative nature of protein molecules may play an important role for their biological functions; it is presumed that in a broad sense, protein specific biological functions are to be maintained by a broad protein interaction including the hydration state of the protein molecules. Contingent modulation of the protein-protein interactions may

cause protein condensation diseases, such as sickle-cell anemia [14], cataract [15], and Alzheimer's disease [16]. Therefore, the present study should be expanded to diverse globular protein systems in solution for gaining deeper physical insights into the intermolecular interactions between globular protein molecules in solution and their modification responding to external conditions.

It has been recognized that lysozyme in solution exhibits a highly eccentric shape of static structure factors. There has long been controversy over the presence or absence of the equilibrium cluster formation, which may result from a co-existing short range attraction and long range repulsion between lysozyme molecules in solution at relatively low ionic strength [17–19]. Recently, the scattering theory on fractal structures built up by the cluster was developed [20]. An elaborate analysis of accurately measured experimental structure factors of lysozyme by combining SQ-IFT and this theory may settle these issues.

6.2.4. Hydrogen-bonding liquid dynamics

From biological, technological, and industrial viewpoints, there is no doubt that water is the most vital solvent on earth. It is not an exaggeration to declare that full-understanding the nature of water is the final goal of my present and future studies. At the end of my thesis, I briefly touch on my current works on hydrogen-bond (H-bond) liquid dynamics, in which dielectric spectroscopy [21] and Raman-induced Kerr effect spectroscopy (RIKES) [22, 23] are combined. I wish that the developments of this project should clarify how collective motions of molecules manifested as a mesoscopic/macroscopic relaxation process is related to an underlying dynamical elementary process, drastically improving our understanding of the H-bond liquid

dynamics.

References

- [1] F.M. Winnik, H. Ringsdorf, and J. Venzmer, *Macromolecules* 23, 2414-2416 (1990).
- [2] H.G. Schild, M. Muthukumar, and D.A. Tirrell, *Macromolecules* 24, 948-952 (1991).
- [3] Y. Zhang, S. Furyk, D.E. Bergbreiter, and P.S. Cremer, *J. Am. Chem. Soc.* 127, 14505-14510 (2005).
- [4] Y. Hirokawa and T. Tanaka, *J. Chem. Phys.* 81, 6379-6380 (1984).
- [5] F. Tanaka, T. Koga, and F.M. Winnik, *Phys. Rev. Lett.* 101, 028302 (2008).
- [6] I. Bischofberger, D. Calzolari, P. De Los Rios, I. Jelezarov, and V. Trappe, *Sci. Rep.* 4, 4377 (2014).
- [7] P.G. de Gennes, *Scaling Concepts in Polymer Physics*, Cornell University Press (1979).
- [8] K. Mortensen, W. Pfeiffer, S. Walter, E. Sackmann, and W. Knoll, *Biochim. Biophys. Acta, Biomembr.* 945, 221-245 (1988).
- [9] H. Sakai, K. Tomiyama, K. Sou, S. Takeoka, and E. Tsuchida, *Bioconjugate Chem.* 11, 425-432 (2000).
- [10] K. Sou, T. Endo, S. Takeoka, and E. Tsuchida, *Bioconjugate Chem.* 11, 372-379 (2000).
- [11] D. Voet, J.G. Voet, and C.W. Pratt, *Fundamentals of biochemistry*, John Wiley and Sons, Inc. (1999).
- [12] J.N. Israelachvili, *Intermolecular and surface forces*, Academic Press (2011).
- [13] M. Schmollngruber, D. Braun, D. Oser, and O. Steinhauser, *Phys. Chem. Chem. Phys.*

18, 3606-3617 (2016).

[14] C.T. Noguchi and A.N. Schechter, *Annu. Rev. Biophys. Biophys. Chem.* 14, 239-263 (1985).

[15] N. Dorsaz, G.M. Thurston, A. Stradner, P. Schurtenberger, and G. Foffi, *J. Phys. Chem. B* 113, 1693-1709 (2009).

[16] S.I.A. Cohen, S. Linse, L.M. Luheshi, E. Hellstrand, D.A. White, L. Rajah, D.E. Otzen, M. Vendruscolo, C.M. Dobson, and T.P.J. Knowles, *Proc. Natl. Acad. Sci. U. S. A.* 110, 9758-9763 (2013).

[17] A. Stradner, H. Sedgwick, F. Cardinaux, W.C.K. Poon, S.U. Egelhaaf, and P. Schurtenberger, *Nature* 432, 492-495 (2004).

[18] Y. Liu, E. Fratini, P. Baglioni, W.R. Chen, S.H. Chen, *Phys. Rev. Lett.* 95, 118102 (2005).

[19] A. Shukla, E. Mylonas, E.D. Cola, S. Finet, P. Timmins, T. Narayanan, and D.I. Svergun, *Proc. Natl. Acad. Sci. U. S. A.* 105, 5075-5080 (2008).

[20] D. Yamaguchi, T. Yuasa, T. Sone, T. Tominaga, Y. Noda, S. Koizumi, and T. Hashimoto, *Macromolecules* 50, 7739-7759 (2017).

[21] T. Fukasawa, T. Sato, J. Watanabe, Y. Hama, W. Kunz, and R. Buchner, *Phys. Rev. Lett.* 95, 197802 (2005).

[22] H. Shirota, K. Yoshihara, N.A. Smith, S. Lin, and S.R. Meech, *Chem. Phys. Lett.* 281, 27-34 (1997).

[23] H. Shirota, *J. Jpn. Soc. Infrared Science and Technology* 22, 40-49 (2012).

List of Publications

1. **Keiichi Yanase**, Miku Obikane, Taku Ogura, Richard Buchner, Akinori Igarashi, Takaaki Sato, “Ion fluctuations and intermembrane interactions in the aqueous dispersions of a dialkylchain cationic surfactant studied using dielectric relaxation spectroscopy and small- and wide-angle X-ray scattering” *Physical Chemistry Chemical Physics*, **20**, 26621-26633 (2018).
2. **Keiichi Yanase**, Richard Buchner, Takaaki Sato, “Microglobule formation and a microscopic order parameter monitoring the phase transition of aqueous poly(*N*-isopropylacrylamide) solution” *Physical Review Materials*, **2**, 085601 (2018).
3. **Keiichi Yanase**, Ryoichi Arai, Takaaki Sato, “Intermolecular interactions and molecular dynamics in bovine serum albumin solutions studied by small angle X-ray scattering and dielectric relaxation spectroscopy” *Journal of Molecular Liquids*, **200**, 59-66 (2014).

Publications not included in this thesis

1. Takaaki Sato, Takesi Akahane, Kenshi Amano, Ryo Hyodo, **Keiichi Yanase**, Taku Ogura, “Scattering and Spectroscopic Study on Hydration and Phase Behavior of Aqueous Alcohol Ethoxylate and Methyl Ester Ethoxylate: Effects of Terminal Groups in Hydrophilic Chains” *The Journal of Physical Chemistry B* **120**, 5444-5454 (2016).
2. Naoya Kobayashi, **Keiichi Yanase**, Takaaki Sato, Satoru Unzai, Michael H. Hecht, Ryoichi Arai, “Self-Assembling Nano-Architectures Created from a Protein Nano-Building Block Using an Intermolecularly Folded Dimeric de Novo Protein” *Journal of the American Chemical Society*, **137**, 11285-11293 (2015).

List of Presentations

Oral presentations at international conferences

1. ○Keiichi Yanase, Richard Buchner, Takaaki Sato “Critical fluctuations and dehydration behavior of a thermo-responsive polymer in aqueous media” *The 12th Mini-Symposium on Liquids* (2018/06/30-07/01 Fukuoka). [**selected as short invited talk**]
2. ○Keiichi Yanase, Richard Buchner, Takaaki Sato “Static Structure and dynamics of a Thermosensitive Polymer in Aqueous Media Exhibiting a Critical Phenomenon” *2nd The Asian Conference on Oleo Science 2017 & 第56回日本油化学会年会*, 3A12 (2017/09/11-13 Tokyo). [**invited**]
3. ○Takuya Sengoku, Koichi Inano, Keiichi Yanase, Ryoichi Arai, Takaaki Sato “A synchrotron small-angle scattering study on protein-protein interactions of lysozyme in solution at different solvent conditions” *2nd The Asian Conference on Oleo Science 2017 & 第56回日本油化学会年会*, **2B03** (2017/09/11-13 Tokyo).
4. ○Keiichi Yanase, Richard Buchner, Takaaki Sato “Scattering and Spectroscopic Study on a Critical Phenomenon of a Thermosensitive Polymer in Aqueous Media” *16th European Student Colloid Conference*, **23** (2017/06/19-22 Florence).
5. ○Takaaki Sato, Keiichi Yanase, Kazuyuki Hasoka, Mamoru Fujiki, Daisuke Suzuki, Kenshi Amano “Renovated Understanding of Critical Behaviour of poly(*N*-isopropylacrylamide): Hydration, Solvent Deuterium Isotope Effects, and Cononsolvency” *The 11th SPSJ International Polymer Conference (IPC2016)*, **14A02** (2016/12/13-16 Fukuoka).
6. ○Keiichi Yanase, Richard Buchner, Daisuke Suzuki and Takaaki Sato “Small- and Wide-angle X-ray Scattering and Dielectric Relaxation Spectroscopy Studies on

Poly(*N*-isopropylacryl amide) in Aqueous Media” Beyond Self-Assembly Workshop, (2016/01/23-27 Bad Gastein).

Poster presentations at international conferences

1. ○**Keiichi Yanase**, Richard Buchner, Takaaki Sato “Phase transition of aqueous poly(*N*-isopropylacrylamide) solution: experimental evidence for micro-globule formation” *Joint Conference of EMLG/JMLG Meeting 2018 and 41st Symposium on Solution Chemistry of Japan*, **P099** (2018/11/04-08 Nagoya).
2. ○Miku Obikane, **Keiichi Yanase**, Kenshi Amano, Norio Tabori, Taku Ogura, Takaaki Sato “Effects of Added Salt on Interactions between Membranes Formed by a Double-Chain Cationic Surfactant” *2nd The Asian Conference on Oleo Science 2017 & 第56回日本油化学会年会*, **P066** (2017/09/11-13 Tokyo).
3. ○Miku Obikane, **Keiichi Yanase**, Kenshi Amano, Norio Tabori, Taku Ogura, Takaaki Sato “Rigidity and flexibility of multilamellar vesicle membranes formed by double chain cationic surfactants by means of small and wide-angle x-ray scattering and dielectric spectroscopy” *16th European Student Colloid Conference*, **P12** (2017/06/19-22 Florence).
4. ○Takuya Sengoku, Kouichi Inano, **Keiichi Yanase**, Ryoichi Arai Takaaki Sato “Renovated interpretation of intermolecular interactions and spatial distributions of hen egg white lysozyme in solution based on the elaborated static structure factor analysis” *The 11th SPSJ International Polymer Conference (IPC2016)*, **15P-G6-146b** (2016/12/13-16 Fukuoka).
5. ○Mamoru Fujiki, **Keiichi Yanase**, Daisuke Suzuki, Takaaki Sato “Small- and Wide-angle X-ray Scattering Study of Cononsolvency: Microscopic Structure and Critical

Behavior of Poly(*N*-isopropylacrylamide) in Monohydric Alcohol/Water Mixtures”
The 11th SPSJ International Polymer Conference (IPC2016), **14P-G2-134b**
(2016/12/13-16 Fukuoka).

6. ○Keiichi Yanase, Richard Buchner, Daisuke Suzuki, Takaaki Sato “Renovated Microscopic Insights into the Critical Behavior of Poly(*N*-isopropylacrylamide) Studied by Small- and Wide-angle X-ray Scattering and Dielectric Relaxation Spectroscopy” *29th Conference of the European Colloid and Interface Society* (2015/09/07-11 Bordeaux).

Oral presentations at domestic conferences

1. ○柳瀬慶一, 藤木衛, Richard Buchner, 佐藤高彰 “温度応答性高分子の相転移に関するミクロ描像と共貧溶媒性に関する新知見” 平成 30 年度繊維学会年次大会, **3C06** (2018/06/13-15 東京).
2. ○佐藤高彰, 柳瀬慶一, 帯金未来, 天野賢史, 戸堀悦雄, 小倉卓 “カチオン界面活性剤膜の膜間相互作用：塩添加に伴う α -ゲル-多重層ベシクル転移” 平成 30 年度繊維学会年次大会, **3C05** (2018/06/13-15 東京).
3. ○帯金未来, 柳瀬慶一, 小倉卓, 天野賢史, 戸堀悦雄, 佐藤高彰 “産業応用可能なベシクル膜の膜間相互作用を散乱手法によってどう捉えるか?” 信州コロイド&界面化学研究会 第三回研究討論会, 一般公演 **3**, (2017/10/27-28 長野).
4. ○仙石琢也, 柳瀬慶一, 稲野紘一, 新井亮一, 佐藤高彰, “実験的構造因子に逆フーリエ変換法を適用した蛋白質間相互作用の可視化” 信州コロイド&界面化学研究会 第三回研究討論会, 一般公演 **4**, (2017/10/27-28 長野).
5. ○帯金未来, 柳瀬慶一, 宮原令二, 土屋好司, 佐藤高彰 “小角広角 X 線散乱法

による非イオン界面活性剤混合系が水中で形成する新規リップル相の静的構造” 第 68 回コロイドおよび界面化学討論会, **2A11** (2017/09/06-08 兵庫).

6. ○柳瀬慶一, Richard Buchner, 柿沼翔平, 城田秀明, 佐藤高彰 “感温性高分子水溶液が示す臨界現象に関わる微視的な構造学的秩序変数及び水の協同的な分子運動” 第 68 回コロイドおよび界面化学討論会, **1G33** (2017/09/06-08 兵庫). [依頼講演]
7. ○柳瀬慶一, Richard Buchner, 佐藤高彰 “散乱法と分光法による感温性高分子水溶液が示す臨界現象に関わる微視的な構造学的秩序変数と溶媒和の解明” 平成 29 年度繊維学会年次大会, **1G10** (2017/06/07-09 東京).
8. ○仙石琢也, 稲野紘一, 柳瀬慶一, 新井亮一, 佐藤高彰 “放射光小角 X 線散乱法を用いたニワトリ卵白由来リゾチーム溶液中におけるタンパク質間相互作用および空間分布の解明” 平成 29 年度繊維学会年次大会, **2C06** (2017/06/07-09 東京).
9. ○柳瀬慶一, Richard Buchner, 佐藤高彰 “感温性高分子水溶液の臨界現象を支配する構造学的な秩序変数と水和” 第 39 回溶液化学シンポジウム, **O32** (2016/11/9-11 茨城).
10. ○佐藤高彰, 赤羽健, 天野賢史, 柳瀬慶一, 兵藤亮 “小角散乱法・動的散乱法・誘電分光法による界面活性剤末端の水素結合サイトの有無が水和・ミセル構造・相挙動に与える影響” 第 39 回溶液化学シンポジウム, **O31** (2016/11/9-11 茨城).
11. ○帯金未来, 柳瀬慶一, 小倉卓, 戸掘悦雄, 佐藤高彰 “ジアルキルジメチルアンモニウム塩分散系の静的構造とイオン及び溶媒水のダイナミクス” 信州コロイド&界面科学研究会 第 2 回研究討論会, 一般講演 **15** (2016/10/28-29 長野).

12. ○藤木衛, 柳瀬慶一, 鈴木大介, 佐藤高彰 “水/メタノール混合溶媒中において共貧溶媒性を示す温度応答性高分子の微細構造及び臨界現象に与える溶媒組成の影響” 信州コロイド&界面科学研究会 第1回研究討論会, 一般講演 7 (2015/10/30-31 長野).
13. ○天野賢史, 柳瀬慶一, 呉羽拓真, 鈴木大介, 佐藤高彰 “異なる温度応答性高分子の共重合化によりもたらされるゲル微粒子の臨界挙動の特異性” 信州コロイド&界面科学研究会 第1回研究討論会, 一般講演 6 (2015/10/30-31 長野).
14. ○天野賢史, 柳瀬慶一, 呉羽拓真, 鈴木大介, 佐藤高彰 “Poly(*N*-isopropylacrylamide) 及び類型の温度応答性高分子をベースとするゲル微粒子が水中で示す臨界挙動の特異性” 平成 27 年度 繊維学会秋季研究発表会, 1C02 (2015/10/22-23 京都).
15. ○Mamoru Fujiki, Keiichi Yanase, Daisuke Suzuki, Takaaki Sato “Structural Study on Cononsolvency and Critical Behavior of poly(*N*-isopropylacrylamide), pNIPAm, in a water/methanol Mixed Solvent” 第64回高分子討論会, 3ESA04 (2015/9/15-17 宮城).

Poster presentations at domestic conferences

1. ○帯金未来, 柳瀬慶一, 小倉卓, 天野賢史, 戸掘悦雄, 佐藤高彰 “ジアルキルジメチルアンモニウム塩が形成するベシクル膜間に働く相互作用; 添加塩濃度及びイオン種依存性” 第68回コロイドおよび界面化学討論会, P008 (2017/09/06-08 兵庫).
2. ○帯金未来, 柳瀬慶一, 小倉卓, 戸掘悦雄, 佐藤高彰 “小角広角 X 線散乱法によるジアルキルジメチルアンモニウム塩分散系が水中で形成するベシク

ル構造と分子膜間に働く相互作用”平成 29 年度繊維学会年次大会, **1P258**
(2017/06/07-09 東京).

3. ○仙石琢也, 稲野紘一, 柳瀬慶一, 新井亮一, 佐藤高彰 “溶液中におけるニワトリ卵白由来リゾチームの静的構造と二体相関関数による分子間相互作用の解明” 第39回溶液化学シンポジウム, **P14**, (2016/11/9-11 茨城).

Acknowledgements

I would like to express my sincere gratitude to my supervisor Prof. Takaaki Sato for his valuable advice and continued encouragements. I wish to thank members of the committee: Prof. Yasushi Murakami, Prof. Yoshiyuki Hattori, Prof. Hideaki Shirota, and Prof. Ryoichi Arai for their insightful comments. I am also grateful to Prof. Hisanao Usami, Prof. Tokihiro Takizawa for their helpful comments.

I wish to thank Prof. Richard Buchner (Regensburg University), Dr. Taku Ogura (LION Corporation), Prof. Ryoichi Arai (Shinshu University), Prof. Hideaki Shirota (Chiba University), and Prof. Hiroaki Yoshida (Shinshu University) for giving me joint research opportunities.

Research fellowships from the Japan Society for the Promotion of Science (Grant No. 17J06213) and International Fiber Engineering Course are gratefully acknowledged.

I deeply thank my colleagues: Minoru Hattori, Takuya Miyashita, Yuki Komata, Takeshi Akahane, Kenshi Amano, Kouichi Inano, Mamoru Fujiki, Takuya Sengoku, and Miku Obikane, researchers at Regensburg University: Dr. Thomas Sonnleitner, Andreas Nazet, and Sergej Friesen, and Shohei Kakinuma at Chiba University for their experimental supports and discussions.

Finally, I wish to express my gratitude to my family for their encouragement.